



**Michigan
Technological
University**

Michigan Technological University
Digital Commons @ Michigan Tech

Dissertations, Master's Theses and Master's Reports

2018

PREDICTING THE ORGANIC COMPOUND DEGRADATION IN AQUEOUS-PHASE ULTRAVIOLET (UV) AND UV-BASED ADVANCED OXIDATION PROCESSES

Erica Coscarelli

Michigan Technological University, eacoscar@mtu.edu

Copyright 2018 Erica Coscarelli

Recommended Citation

Coscarelli, Erica, "PREDICTING THE ORGANIC COMPOUND DEGRADATION IN AQUEOUS-PHASE ULTRAVIOLET (UV) AND UV-BASED ADVANCED OXIDATION PROCESSES", Open Access Master's Thesis, Michigan Technological University, 2018.
<https://doi.org/10.37099/mtu.dc.etr/717>

Follow this and additional works at: <https://digitalcommons.mtu.edu/etdr>

 Part of the [Environmental Engineering Commons](#)

PREDICTING THE ORGANIC COMPOUND DEGRADATION IN AQUEOUS-PHASE
ULTRAVIOLET (UV) AND UV-BASED ADVANCED OXIDATION PROCESSES

By

Erica A. Coscarelli

A THESIS

Submitted in partial fulfillment of the requirements for the degree of

MASTER OF SCIENCE

In Environmental Engineering

MICHIGAN TECHNOLOGICAL UNIVERSITY

2018

© 2018 Erica A. Coscarelli

This thesis has been approved in partial fulfillment of the requirements for the Degree of MASTER OF SCIENCE in Environmental Engineering.

Department of Civil and Environmental Engineering

Thesis Advisor: *Dr. Daisuke Minakata*

Committee Member: *Dr. David Hand*

Committee Member: *Dr. Alex Mayer*

Department Chair: *Dr. Audra Morse*

Table of Contents

List of Figures.....	v
List of Tables.....	viii
Author contribution statement.....	ix
Acknowledgements	x
List of symbols and abbreviations.....	xi
Abstract.....	xiii
1 Introduction.....	1
2 Mechanistic Insight into the Degradation of Nitrosamines via Aqueous-Phase UV Photolysis or a UV-Based Advanced Oxidation Process: Quantum Mechanical Calculations.....	3
2.1 Introduction	3
2.2 Materials and Methods	5
2.3 Results	6
2.3.1 HO [•] -Induced Degradation	6
2.3.1.1 N-Nitrosodimethylamine (NDMA) Degradation Pathways Induced by HO [•]	6
2.3.1.2 N-Nitrosomethylethylamine (NMEA) Degradation Pathways Induced by HO [•]	9
2.3.1.3 N-Nitrosomethylbutylamine (NMBA) Degradation Pathways Induced by HO [•]	11
2.3.2 UV-Induced Degradation	15
2.3.2.1 NDMA Degradation Pathways Induced by UV Photolysis	15
2.3.3 Environmental Implication and Future Study.....	19
3 The Fate of N-Nitrosodimethylamine (NDMA) Degradation in Aqueous-phase UV Photolysis.....	20
3.1 Introduction.....	20
3.2 Materials and Methods	23
3.3 Results and Discussion	24
3.3.1 Elementary Reaction Pathways After Initial Photolysis of NDMA ...	24
3.3.2 Quantum Yields and Reaction Rate Constants	28
3.3.3 Time-dependent Concentration Profiles of NDMA and Byproducts	30
3.3.4 Sensitivity Analysis	33
3.4 Environmental Implications	42

4	Development of an Agent-based Model to Predict the Fate of Organic Compound Degradation in Aqueous Phase Advanced Oxidation Processes	43
4.1	Introduction.....	43
4.2	Materials and Methods	49
4.2.1	Model Overview	49
4.2.2	Entities, State Variables, and Scales	49
4.2.3	Data Requirements.....	50
4.2.4	Model Initialization	51
4.2.5	Process Overview and Scheduling	51
4.2.6	Sub-models	53
4.2.6.1	Movement of the Molecule Agent	53
4.2.6.2	Photolysis.....	53
4.2.6.3	Interaction Radius	54
4.2.6.4	Dissociation and Non-dissociation of Species.....	55
4.2.7	Design Concepts	55
4.2.8	Emergence	56
4.2.9	Interaction.....	56
4.2.10	Stochasticity	56
4.2.11	Observations	57
4.2.12	Model Simplifications	57
4.2.13	Input Parameters	57
4.3	Experimental Materials and Methods.....	58
4.3.1	Reactor Setup.....	58
4.3.2	Chemical Description.....	58
4.3.3	Experimental Setup	59
4.4	Results	60
4.5	Applicability and Future Work	69
5	Conclusions and Future Work.....	70
5.1	Chapter 2.....	70
5.2	Chapter 3.....	70
5.3	Chapter 4.....	70
6	Bibliography.....	71
A	Supporting Information for Chapter 4.....	81
A.1	Hydrogen Peroxide Decay Slope Calculations.....	81
A.2	Console Output.....	81
B	Copyright documentation	83
	Copyright and Licensing.....	83

List of Figures

Figure 2.1 Free energy profile for pathway 1–1 of the HO [•] -induced reaction pathways for <i>N</i> -nitrosodimethylamine (NDMA) via H abstraction	7
Figure 2.2 Free energy profile for pathway 1–2 of the HO [•] -induced reaction pathways for <i>N</i> -nitrosodimethylamine (NDMA) via HO [•] addition to amine nitrogen.....	8
Figure 2.3 Free energy profile for pathway 1–3 of the HO [•] -induced reaction pathways for <i>N</i> -nitrosodimethylamine (NDMA) via HO [•] addition to the nitrosyl nitrogen	8
Figure 2.4 Free energy profile for pathway 2–1 of the HO [•] -induced reaction pathways for NMEA via H abstraction from a C–H bond of the –CH ₂ – functional group adjacent to the N–NO functional group.....	10
Figure 2.5 Free energy profile for pathway 2–2 of the HO [•] -induced reaction pathways for NMEA via H abstraction from a C–H bond of the terminal CH ₃ functional group in the ethyl chain.....	11
Figure 2.6 Free energy profile for pathway 2–3 of the HO [•] -induced reaction pathways for NMEA via H abstraction from a C–H bond of the terminal CH ₃ functional group adjacent to the N–NO functional group	11
Figure 2.7 Free energy profile for pathway 3–1 of the HO [•] -induced reaction pathways for NMBA via H abstraction from a C–H bond of the –CH ₂ – functional group adjacent to the N–NO functional group.....	13
Figure 2.8 Free energy profile for pathway 3–2 of the HO [•] -induced reaction pathways for NMBA via H abstraction from a C–H bond of the -CH ₂ functional group adjacent to the –CH ₂ – functional groups on both sides.....	14
Figure 2.9 Free energy profile for pathway 3–3 of the HO [•] -induced reaction pathways for NMBA via H abstraction from a C–H bond of the terminal CH ₃ functional group in a butyl chain.....	14
Figure 2.10 Free energy profile for pathway 3–4 of the HO [•] -induced reaction pathways for NMBA via H abstraction from a C–H bond of the terminal CH ₃ functional group adjacent to the N–NO functional group	15
Figure 2.11 HOMO and lowest unoccupied molecular orbital (LUMO) of the $\pi \rightarrow \pi^*$ (a) and $n \rightarrow \pi$ (b) transitions at 212 nm and 341 nm, respectively.	16
Figure 2.12 Free energy profile for pathway 4–1 of the HO [•] -induced reaction pathways for NDMA photolysis.	17
Figure 2.13 Free energy profile for pathway 4–2 of the HO [•] -induced reaction pathways for NDMA photolysis.	17

Figure 2.14 Free energy profile for pathway 4–3 of the HO [•] -induced reaction pathways for NDMA photolysis.	18
Figure 2.15 Free energy profile for pathway 4–3 of the HO [•] -induced reaction pathways for NDMA photolysis.	18
Figure 3.1 NDMA photolysis pathways and subsequent reactions.....	25
Figure 3.2 Nitrate and nitrite photolysis pathways and the transformation products.....	27
Figure 3.3 Concentration profile of major byproducts of NDMA decay at pH 3 for model in comparison to experimental results from Lee et al. 2005 [23].....	31
Figure 3.4 Concentration profile of minor byproducts of NDMA decay at pH 3 for model in comparison to experimental results from Lee et al. 2005 [23].....	32
Figure 3.5 Concentration profile of major byproducts of NDMA decay at pH 7 for model in comparison to experimental results from Lee et al. 2005 [23].....	32
Figure 3.6 Concentration profile of minor byproducts of NDMA decay at pH 7 for model in comparison to experimental results from Lee et al. 2005 [23].....	33
Figure 3.7 NDMA concentration profile at pH 3 for variation of quantum yield two times the originally reported value	35
Figure 3.8 NDMA concentration profile at pH 3 for variation of quantum yield half of the originally reported value	35
Figure 3.9 NDMA concentration profile at pH 7 for variation of quantum yield two times the originally reported value	36
Figure 3.10 NDMA concentration profile at pH 7 for variation of quantum yield half of the originally reported value	36
Figure 3.11 DMA concentration profile at pH 3 for variation of quantum yield two times the originally reported value	37
Figure 3.12 DMA concentration profile at pH 3 for variation of quantum yield half the originally reported value	38
Figure 3.13 DMA concentration profile at pH 7 for variation of quantum yield two times the originally reported value	38
Figure 3.14 DMA concentration profile at pH 7 for variation of quantum yield half the originally reported value	39
Figure 3.15 MA concentration profile at pH 3 for variation of quantum yield two times the originally reported value and rate constant by ten times the originally reported value	40

Figure 3.16 MA concentration profile at pH 3 for variation of quantum yield half the originally reported value and rate constant by one tenth the originally reported value	40
Figure 3.17 MA concentration profile at pH 7 for variation of quantum yield two times the originally reported value and rate constant by ten times the originally reported value	41
Figure 3.18 MA concentration profile at pH 7 for variation of quantum yield half the originally reported value and rate constant by one tenth the originally reported value	41
Figure 4.4 Time-dependent concentration profiles of acetone, hydrogen peroxide, and other byproducts formed in UV/H ₂ O ₂ process	61
Figure 4.5 Snapshots of our agent based model that represent the agents of species at different time points.....	61
Figure 4.6 Time-dependent concentration profile of hydrogen peroxide.....	63
Figure 4.7 Time-dependent concentration profile of acetone	65
Figure 4.8 Time-dependent concentration profile of acetic acid	66
Figure 4.9 Time-dependent concentration profile of oxalic acid	67
Figure 4.10 Time-dependent concentration profile of formic acid.....	68

List of Tables

Table 3.1 Input parameters for simulation from Lee experiment [23]	24
Table 3.2 Photolysis reactions as input in code with quantum yield values for each pH tested.....	28
Table 3.3 Input irreversible reactions for compounds considered in the code	29
Table 3.4 Reactions and corresponding quantum yield values varied for sensitivity analysis.....	34
Table 4.3 Simplified reaction pathways and the reaction rate constants used in the test run	62
Table A.6.1 Experimentally obtained concentrations of hydrogen peroxide over time in benchtop photolysis experiment.....	81
Table A.6.2 Slope and y intercept for linear fit of hydrogen peroxide decay based on variation in included experimental points.....	81

Author contribution statement

This thesis is written in the intention for publication. Portions of the thesis have already been published or presented:

D. Minakata and E. Coscarelli, "Mechanistic Insight into the Degradation of Nitrosamines via Aqueous-Phase UV Photolysis or a UV-Based Advanced Oxidation Process: Quantum Mechanical Calculations," *Molecules*, vol. 23, no. 3, p. 539, 2018.

The remaining chapters are in the process of being prepared for submission.

For Chapter 2, Mechanistic Insight into the Degradation of Nitrosamines via Aqueous-Phase UV Photolysis or a UV-Based Advanced Oxidation Process: Quantum Mechanical Calculations; Dr. Daisuke Minakata and Erica Coscarelli contributed to the analysis of the results and to the writing of the manuscript. Dr. Minakata performed all quantum mechanical calculations and is the corresponding author of this publication.

For Chapter 3, Reaction Mechanisms for the Degradation of Trace Organic Contaminants through Advanced Oxidation Processes: Study of NDMA in UV Photolysis System; Dr. Daisuke Minakata, Divya Kamath and Erica Coscarelli contributed to the analysis of the results and to the writing of the manuscript. Dr. Minakata and Divya Kamath developed the original photolysis model and Dr. Minakata performed all quantum mechanical calculations. Dr. Minakata is the corresponding author of this chapter.

For Chapter 4, Development of An Agent-based Model to Predict the Fate of Organic Compound Degradation in Aqueous Phase Advanced Oxidation Processes; Robert Zupko, Divya Kamath, Erica Coscarelli, Dr. Mark Rouleau and Dr. Daisuke Minakata contributed to the implementation of the research, to the analysis of the results and to the writing of the manuscript. Robert Zupko developed the codes for an agent-based model. Divya Kamath and Dr. Minakata performed all the experiments. Dr. Rouleau and Dr. Minakata are the corresponding authors.

Acknowledgements

I would like to start by thanking my advisor, Dr. Daisuke Minakata of the Civil and Environmental Engineering Department at Michigan Technological University. He has been very supportive and helpful throughout my masters. Dr. Minakata also believed in me and helped me to obtain the funding I needed to complete my degree, which I am extremely thankful for.

I also would like to acknowledge the support of my committee members, Dr. David Hand and Dr. Alex Mayer. I appreciate you being so flexible with me. Thank you for your comments and suggestions as they helped to better me as an engineer. Throughout my graduate degree all of the faculty and staff in the Department of Civil and Environmental have been beyond helpful and because of them I am well prepared for my future as a professional Environmental Engineer.

None of this would have been possible without the financial support I received throughout my time in graduate school. This work was supported by the National Science Foundation CBET 1435926, the American Water Works Association Carollo Engineers Bryant L. Bench Scholarship, the Michigan Space Grant Consortium, the Department of Civil and Environmental Engineering, the Great Lakes Research Center Graduate Student Leadership Award, and the Society of Women Engineers Michigan Tech Chapter. Thank you. In particular, Dr. Morse at the Department of Civil and Environmental Engineering and Dr. Guy Meadows and Elizabeth Hoy at the Michigan Tech Great Lake Research Center are acknowledged here for their supports.

Finally I would like to thank my family and friends for supporting me as I worked tirelessly to achieve my goal of getting my masters. A special thanks to my parents, who believed in me even when they had only a vague idea of the work I was doing, and encouraged me to keep going when things got to be overwhelming. I would also like to thank my fiancé, Josh, for all his love and support. I am extremely thankful to have had such amazing support throughout my time in graduate school, and without it none of this would have been possible.

Erica Coscarelli

List of symbols and abbreviations

AOPs	advanced oxidation processes
ABM or ABM(s)	agent-based modeling or agent-based model(s)
ChemSim	agent based model created by our group specifically for AOPs
CH ₂ =N(+) <i>H</i> CH ₃	<i>N</i> -methylidenemethylamine
CH ₃ NHCH ₃	methyl diamine
CSV	comma-separated values
DFT	density functional theory
DMA	dimethylamine
DMP	2,9-dimethyl-1,10-phenanthroline
DOM	dissolved organic matter
EPA	Environmental Protection Agency
$\Delta G_{\text{aq,calc}}^{\text{act}}$	theoretically calculated aqueous phase free energy of activation
$\Delta G_{\text{aq,calc}}^{\text{react}}$	theoretically calculated aqueous phase free energy of reaction
G4	Gaussian-4 theory
HCHO	formaldehyde
HCOOH	formic acid
HNO ₂	nitrous acid
HO [•]	hydroxyl radicals
HOMO	highest occupied molecular orbital
LFER	linear free energy relationship
MA	methylamine
NF	nanofiltration
NDEA	<i>N</i> -nitrosodiethylamine
NDMA	<i>N</i> -nitrosodimethylamine
NMEA	<i>N</i> -nitrosomethylethylamine
NO [•]	nitric oxide
NO ₃ ⁻	nitrate ion
NO ₂ ⁻	nitrite ion
ODE(s)	ordinary differential equation(s)

ONOO ⁻	peroxynitrite
[•] O ₂ ⁻	superoxide anion radical
QM	quantum mechanical
RO	reverse osmosis
SMD	universal solvation model
TD-DFT	time-dependent density functional theory
TOC	total organic carbon
TS	transition state
UV	ultraviolet

Abstract

Clean safe drinking water is vital for society. With increasing water scarcity and the increased numbers of chemicals identified in waterways, it is important for us to fully understand how to destroy contaminants of concern and prevent potentially hazardous byproducts that may be produced from the degradation processes. Little is known about how nitrogen containing organics behave and degrade in current water treatment systems and therefore their role in water reuse. N-nitrosodimethylamine (NDMA), is carcinogenic and is being formed during conventional chlorination of drinking water. Ultraviolet (UV) photooxidation has been shown to degrade NDMA, but the degradation pathways and their kinetics are not well understood. The overall goal of this study is to determine the fate of nitrogen-containing organics in UV photolysis and UV-based advanced oxidation processes. In this study we use quantum mechanical calculations to determine the elementary pathways and their kinetics for the degradation of nitrosamines. From there, the ordinary differential equations of all species involved in the degradation process were generated and solved numerically. The predicted results were compared to the experimental observations reported in the literature.

1 Introduction

Clean water is essential, and therefore water treatments and ensuring the removal of contaminants is vital for both human and environmental health. The presences of new emerging contaminants or trace contaminants, such as pharmaceuticals and personal care products are becoming more prevalent in our waters and will continue rise with the increase in direct and indirect potable reuse [1-4]. These emerging contaminants are not well understood and often are not removed using conventional water and wastewater treatment approaches. In addition, these contaminants are likely to become even more problematic in the near future as de facto and planned water reuse is increased [5].

Use of ultraviolet (UV) photolysis and UV-based advanced oxidation processes (AOPs) are attractive treatment methods because these method destroy the target organic contaminants. The hydroxyl radicals react rapidly and non-selectively with most electron-rich sites on organic compounds and destroy a wide variety of organic compounds. AOPs can lead to the complete mineralization of organic compounds in the subsequent radical-involved chain reactions, if adequately designed. The initial fate of hydroxyl radicals-induced reactions with diverse organic compounds have been studied, the mechanisms that produce intermediate-radicals and transformation byproducts are not well understood [6, 7]. A better understanding of the complete reaction pathway and the elementary reactions that occur within the UV and AOP systems is vital to preventing the formation of harmful byproducts and ensuring removal of the trace organic contaminants.

Nitrosamines are a group of carcinogenic chemicals that are present in aquatic environments that result from byproducts of industrial processes and disinfection products. UV photolysis or UV-based AOPs are promising technologies to remove nitrosamines from water. However, complex reaction mechanisms involving radicals limit our understandings of the elementary reaction pathways embedded in the overall reactions identified experimentally. In Chapter 2, we perform quantum mechanical calculations to identify the photolysis-/hydroxyl radical-induced initial elementary reactions with various *N*-nitrosamine compounds including *N*-nitrosodimethylamine (NDMA), *N*-nitrosomethylethylamine, and *N*-nitrosomethylbutylamine.

The results presented in Chapter 2 provide mechanistic insight into the elementary reaction pathways, and were combined with the kinetic information to predict the time-dependent concentration profiles of nitrosamines and their transformation products in Chapter 3. These profiles were created through the development of ordinary differential equations and then solved numerically to obtain the time-dependent concentration profiles of all species involved in the reaction. With the coupling of the benchtop laboratory experiments reported in the literature, the proposed elementary reactions-based kinetic model is validated.

The ordinary differential equations generated in UV-photolysis and UV-based advanced oxidation processes are stiff and time-intensive to solve them numerically. The use of agent-based models (ABMs) is a novel bottom up that can be used to model complex systems, such as AOPs, as shown in Chapter 4. The goal of this study is to determine the feasibility of ABM in predicting concentrations of byproducts and to gain an understanding of the intermediate radicals and stable byproducts involved in peroxy radical bimolecular decay.

2 Mechanistic Insight into the Degradation of Nitrosamines via Aqueous-Phase UV Photolysis or a UV-Based Advanced Oxidation Process: Quantum Mechanical Calculations¹

2.1 Introduction

Nitrosamines, which contain N–NO functional groups, are a group of chemicals that pose mutagenicity, teratogenicity, and carcinogenicity [9]. Nitrosamines are the byproducts of various manufacturing, agricultural, and natural processes and have been found in natural aquatic environments and in the effluent of wastewater treatment processes [10]. As a type of nitrosamine, N-nitrosodimethyl amine [NDMA, (CH₃)₂N–NO] is a low-molecular-weight, neutral, organic contaminant that has also been found to be present in aquatic environments. The California Department of Health Services has set notification levels of 10 ng/L for NDMA and other nitrosamines in drinking water [11].

Ultraviolet (UV) photolysis and UV-based advanced oxidation processes (AOPs) that produce highly reactive hydroxyl radicals (HO[•]) are attractive and promising water treatment technologies, which can inactivate pathogens and destroy a wide variety of organic chemical contaminants [12, 13]. UV photolysis and UV-AOPs have been employed in wastewater reclamation processes for indirect or direct potable reuse of treated wastewater to increase water security and address water scarcity issues in many arid regions [14]. Wastewater reclamation processes use multiple barriers to physically remove pathogens and chemical contaminants via microfiltration/ultrafiltration, followed by nanofiltration (NF)/reverse osmosis (RO). After the NF/RO process, UV photolysis or UV-AOPs inactivate pathogens and destroy chemicals present in the NF/RO permeate stream. Over 50% of NDMA has been found to be present in the NF/RO permeate, and the use of UV photolysis or UV-AOPs are necessary to remove NDMA and other nitrosamines [15].

¹ The material contained in this chapter has previously been published, Minakata and Coscarelli (2018) [8]

UV photolysis using a low-pressure UV lamp that emits photons at a wavelength of 254 nm is very effective at destroying NDMA due to the high molar absorptivity ($1650 \text{ M}^{-1}\text{cm}^{-1}$ at 253.7 nm) and highly reactive HO^\bullet produced in AOPs rapidly react with many nitrosamines to effectively destroy the initial contaminants (the second order reaction rate constants of HO^\bullet ; $k = 10^8 - 10^9 \text{ M}^{-1}\text{s}^{-1}$) [16, 17]. However, complex chemical reactions involving radicals produce a number of transformation byproducts, and hence, detailed reactivity and reaction pathways for NDMA and other nitrosamines have not been elucidated yet. For example, Mezyk's group studied the kinetics of HO^\bullet with various structurally different nitrosamines, and found that NDMA, N-nitrosomethylethylamine (NMEA) and N-nitrosodiethylamine (NDEA) showed different reactivity and degradation efficiency from other nitrosamines that have longer alkyl chains adjacent to the N-NO functional group. They proposed that radical delocalization caused the differences in the degradation efficiency, but the detailed reaction pathway has not been identified yet [16]. Stefan and Bolton (2002) investigated reaction pathways for NDMA degradation based on laboratory-scale batch photolysis experiments and explained the initial photolysis mechanisms based on the reaction pathways previously identified by studies in the 1960s and 1970s [18-22]. UV-induced NDMA degradation pathways were studied at both pH 3 and pH 7 to identify the transformation products, such as methylamine, dimethylamine, formaldehyde, formic acid, nitrite ion and nitrate ion [23, 24]. Their careful experiments and measurement of transformation products proposed several key reaction pathways that were induced by UV photolysis at a wavelength of 253.7 nm at different pH values [23, 24]. However, some of the pathways involved in the formation of transformation products are still unknown. UV-induced NDMA degradation was also studied and identified previously unknown reactive species in the NDMA degradation pathways [25, 26]. The HO^\bullet -induced NDMA degradation mechanisms were studied in an ozone-based AOP, and general reaction mechanisms were proposed [27, 28]. The major transformation mechanisms were proposed based on experimental studies of the products, but the elementary reaction pathways are not known due to difficulties in identifying the embedded reactions that were involved in the overall reaction.

Quantum mechanical (QM) calculations using ab initio methods or density functional theory (DFT) are attractive approaches to identify elementary reaction pathways and the kinetics of complex fast radical reactions [29]. QM calculations have been used to

support experimentally identified reaction pathways by calculating the reaction energy using statistical thermodynamics. Aqueous-phase enthalpy and free energies of activation and reaction were calculated to determine the dominant degradation pathway of dimethyl phthalate [30]. Elementary reactions involved in the HO[•]-induced mineralization of flutriafol were identified [31]. DFT calculations were used to determine the NDMA formation mechanism from N,N-dimethylsulfamide via ozonation in water [32]. A high-level multi-point energy method was used to calculate the aqueous-phase free energies of activation for HO[•]-induced reactions of a wide variety of organic compounds, including aliphatic compounds, alkenes, and aromatic compounds [33-35]. These studies highlight the usefulness of QM-based calculations to provide insight into reaction mechanisms that cannot be obtained by experiments. In addition, the findings from QM-based calculations also provide potential transformation products that can be identified in future experiments.

In this study, we use QM-based calculations to identify the HO[•]-induced initial elementary reactions with NDMA and other nitrosamines as well as the UV-induced NDMA degradation pathways at 254 nm of wavelength. We investigate NDMA, NMEA, and N-nitrosomethylbutylamine (NMBA), which have different alkyl side chains that are adjacent to the nitroso functional group (–N–NO), to elucidate the effect of the alkyl side chain on the overall reactivity with HO[•]. We also investigate UV-induced NDMA degradation using time-dependent (TD)-DFT to understand the molecular orbitals responsible for electron excitation and the nitrogen-containing radical reactions during the photolysis of NDMA.

2.2 Materials and Methods

All of the QM calculations were performed with the Gaussian 09 revision D.02 program [36] using the Michigan Tech high-performance cluster “Superior” and homemade LINUX workstations. The M06-2X/cc-pVDZ [37] was used to optimize the electronic structures and calculate the frequencies in both the gas and aqueous phase for the HO[•]-induced reaction pathways with NDMA, NMEA, and NMBA. The UV-induced reaction pathways with NDMA was calculated with the Gaussian-4 theory (G4) [38]. The aqueous-phase structures and frequencies were obtained using an implicit polarizable continuum model [universal solvation model (SMD)] [39]. Previously, we verified the

combination of M06-2X/cc-pVDZ or G4 with the SMD model by successfully applying it to other aqueous-phase radical-involved reactions [33, 40]. Theoretically calculated absorption spectra were obtained from a TD-DFT analysis [41, 42] of the optimized aqueous-phase structure of NDMA at the level of M06-2X/cc-pVDZ with the SMD solvation model. To investigate the contributions from molecular orbitals to the peak of the spectra, molecular orbitals were determined using a natural population analysis at the level of M06-2X/cc-pVQZ with the SMD solvation model. The detailed calculation procedures for the transition state search, the aqueous-phase free energies of activation and reaction, and the associated computational methods are found in previous reports [40].

2.3 Results

2.3.1 HO[•]-Induced Degradation

2.3.1.1 *N*-Nitrosodimethylamine (NDMA) Degradation Pathways Induced by HO[•]

NDMA has three potential initial degradation mechanisms: (1) H atom abstraction from a C–H bond of the methyl group (pathway 1–1 in Figure 1), (2) HO[•] addition to amine nitrogen (pathway 1–2 in Figure 2), and (3) HO[•] addition to nitrosyl nitrogen (pathway 1–3 in Figure 3). Our QM calculations obtained $\Delta G_{\text{aq,calc}}^{\text{act}}$ values of 9.7 kcal/mol, 6.8 kcal/mol, and 9.6 kcal/mol for the respective pathways. H abstraction from a C–H bond forms a C-centered radical that reacts with the triplet state of molecular oxygen dissolved in water. Our previous studies indicate that the addition of molecular oxygen to a C-centered radical is a barrierless reaction with a $\Delta G_{\text{aq,calc}}^{\text{act}}$ of $-20 \sim -30$ kcal/mol, which enabled us to consistently predict the experimentally measured reaction rate constants [40]. The $\Delta G_{\text{aq,calc}}^{\text{act}}$ value obtained for the $\cdot\text{CH}_2\text{NNOCH}_3$ radical was 2.3 kcal/mol, which is significantly larger than those of typically observed reactions. This indicates that the N–NO functional group significantly affects molecular addition to the C-centered radical. The second-order reaction rate constant for the addition of molecular oxygen to a C-centered radical of NDMA was determined to be $(5.3 \pm 0.6) \times 10^6 \text{ M}^{-1}\text{s}^{-1}$ [17], which is three orders of magnitude smaller than the typically observed rate constants ($\sim 5 \times 10^9 \text{ M}^{-1}\text{s}^{-1}$) [43]. A more detailed discussion on the unique reactivity of molecular oxygen to

C-centered radicals will be given in a later section. According to our calculations, the C-centered radical also undergoes electron transfer to produce $\text{CH}_3\text{NNO}=\text{CH}_2$ ($\Delta G_{\text{aq,calc}}^{\text{rct}}$ of -2.0 kcal/mol), followed by the loss of NO^\bullet ($\Delta G_{\text{aq,calc}}^{\text{rct}}$ of -11.3 kcal/mol) to produce N-methylenemethylamine ($\text{CH}_2=\text{NHCH}_3$). This latter pathway involves several barrierless reactions, and is dominant over the pathway involving the addition of molecular oxygen. The formation of N-methylenemethylamine was also postulated in a previous report [26].

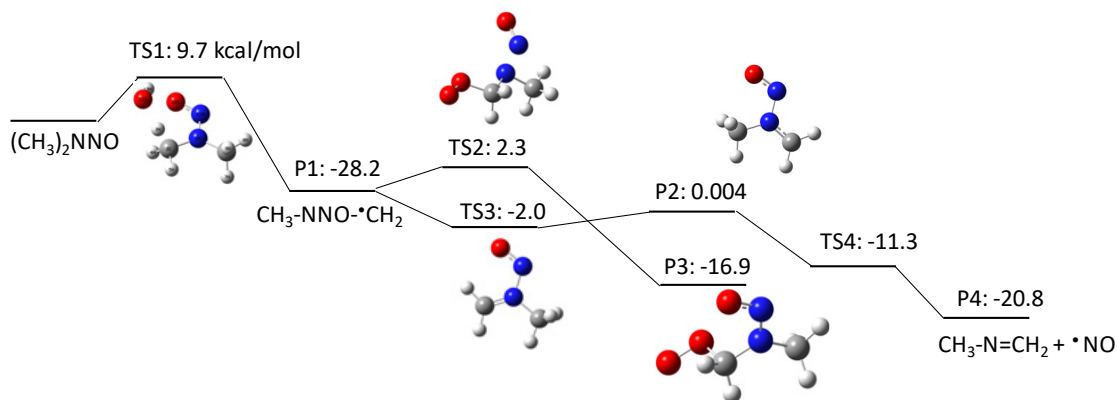


Figure 2.1 Free energy profile for pathway 1–1 of the HO^\bullet -induced reaction pathways for *N*-nitrosodimethylamine (NDMA) via H abstraction. TS denotes the transition state, and P denotes the product. The numbers (kcal/mol) are the free energy of activation for the TS and free energy of reaction for the P relative to the corresponding reactant. Blue represents a nitrogen atom, red represents an oxygen atom, white represents a hydrogen atom, and gray represents a carbon atom (The color notation is valid throughout the chapter).

The second pathway is HO^\bullet addition to the amine nitrogen, followed by the loss of an OH group. Although initial HO^\bullet addition has a lower free energy of activation ($\Delta G_{\text{aq,calc}}^{\text{rct}}$ of 6.8 kcal/mol) than the H abstraction identified in pathway 1–1, the subsequent reaction has a larger activation barrier ($\Delta G_{\text{aq,calc}}^{\text{rct}}$ of 3.1 kcal/mol) to produce a N-centered radical (i.e., $\text{CH}_3^\bullet\text{NCH}_3$). The N-centered radical undergoes either molecular oxygen addition or an H shift. The H shift has a significantly smaller $\Delta G_{\text{aq,calc}}^{\text{rct}}$ of -1.9 kcal/mol than molecular oxygen addition to the N-centered radical ($\Delta G_{\text{aq,calc}}^{\text{rct}}$ of 9.8 kcal/mol). Thus, C-centered radical formation resulting from an H shift is the dominant pathway via TS8. The significantly large $\Delta G_{\text{aq,calc}}^{\text{rct}}$ for the addition of molecular oxygen to a N-centered radical

via TS7 can be verified by the experimentally obtained reaction rate constant for hydrazyl ($k = 3.9 \times 10^8 \text{ M}^{-1}\text{s}^{-1}$) [43].

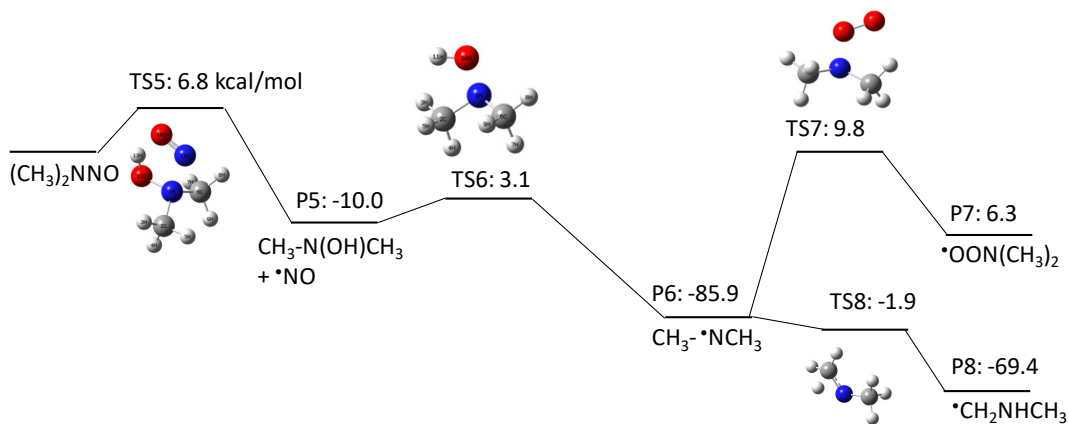


Figure 2.2 Free energy profile for pathway 1–2 of the HO \cdot -induced reaction pathways for *N*-nitrosodimethylamine (NDMA) via HO \cdot addition to amine nitrogen. The numbers (kcal/mol) are the free energy of activation for the TS and free energy of reaction for the P relative to the corresponding reactant.

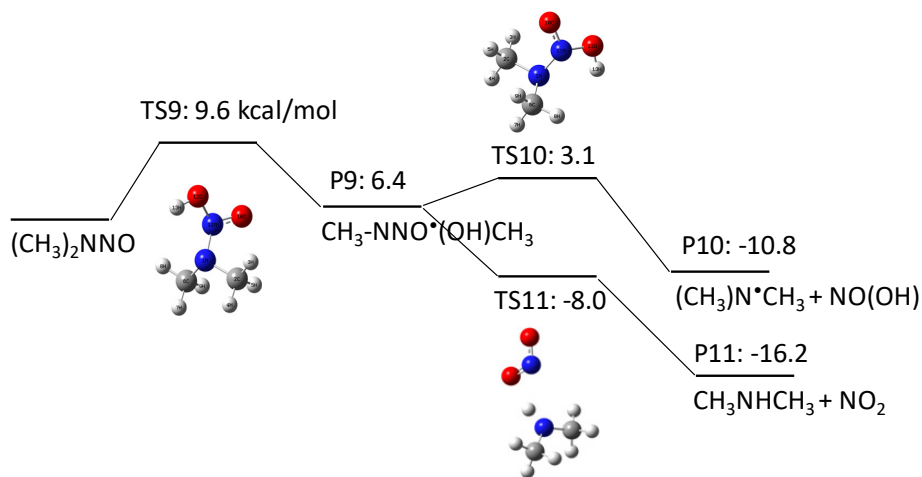


Figure 2.3 Free energy profile for pathway 1–3 of the HO \cdot -induced reaction pathways for *N*-nitrosodimethylamine (NDMA) via HO \cdot addition to the nitrosyl nitrogen. The numbers (kcal/mol) are the free energy of activation for the TS and free energy of reaction for the P relative to the corresponding reactant.

Pathway 1–3 involves initial HO \cdot addition to the nitrosyl nitrogen with a $\Delta G_{\text{aq,calc}}^{\text{act}}$ of 9.6 kcal/mol. Although this reaction has an almost identical $\Delta G_{\text{aq,calc}}^{\text{act}}$ to that of pathway 1–1, the initial HO \cdot addition reaction that produces an alkoxy radical [i.e., CH₃NNO \cdot (OH)CH₃]

is not thermodynamically favored ($\Delta G_{\text{aq,calc}}^{\text{react}}$ of 6.4 kcal/mol). This alkoxy radical undergoes two pathways to produce (1) a N-centered radical with a $\Delta G_{\text{aq,calc}}^{\text{act}}$ of 3.1 kcal/mol and (2) methyl diamine (CH_3NHCH_3) with a $\Delta G_{\text{aq,calc}}^{\text{act}}$ of -8.0 kcal/mol.

The above investigation confirms that H abstraction from a C-H bond of the methyl functional group of NDMA is the dominant initial reaction pathway as induced by HO^\bullet , which is consistent with the experimental investigation using the electron paramagnetic resonance (ESR) technique [17]. The experimentally determined second-order rate constant was $(4.3 \pm 0.12) \times 10^8 \text{ M}^{-1}\text{s}^{-1}$, and this relatively slow H abstraction from a C-H bond by HO^\bullet results from the electron-withdrawing effect of the neighboring N-NO functional group and the abnormally stable C-centered radical [17]. In the following subsections, the reactivity of NDMA will be compared to two other nitrosamines that have longer alkyl side chains (i.e., $-\text{CH}_2\text{CH}_3$ and $-(\text{CH}_2)_2\text{CH}_3$) to investigate the unique reactivity of NDMA.

2.3.1.2 *N-Nitrosomethylethylamine (NMEA) Degradation Pathways Induced by HO^\bullet*

NMEA has three potential H abstraction sites: (1) a C-H bond of the $-\text{CH}_2-$ functional group adjacent to the N-NO functional group by pathway 2-1, (2) a C-H bond of the terminal CH_3 functional group in the ethyl chain by pathway 2-2, and (3) a C-H bond of the terminal CH_3 functional group adjacent to the N-NO functional group by pathway 2-3. Figures 4-6 show the free energy profiles per reaction coordinate for each pathway. Our calculations revealed similar $\Delta G_{\text{aq,calc}}^{\text{act}}$ values for H atom abstraction: 11.1 kcal/mol in pathway 2-1 and 11.7 kcal/mol in pathway 2-3, except 62.7 kcal/mol in pathway 2-2. It is still not clear why the pathway 2-2 had such a high barrier. All three pathways are thermodynamically favorable ($\Delta G_{\text{aq,calc}}^{\text{react}} < 0$). Each pathway produces a C-centered radical, i.e., $\text{CH}_3^\bullet\text{CHNNOCH}_3$ in pathway 2-1, $^\bullet\text{CH}_2\text{CH}_2\text{NNOCH}_3$ in pathway 2-2, and $\text{CH}_3\text{CH}_2\text{NNO}^\bullet\text{CH}_2$ in pathway 2-3. The $\Delta G_{\text{aq,calc}}^{\text{act}}$ values for the addition of molecular oxygen to $\text{CH}_3^\bullet\text{CHNNOCH}_3$, $^\bullet\text{CH}_2\text{CH}_2\text{NNOCH}_3$, and $\text{CH}_3\text{CH}_2\text{NNO}^\bullet\text{CH}_2$ are 3.8 kcal/mol, -13.9 kcal/mol, and -2.2 kcal/mol, respectively. As observed in pathway 1, the $\Delta G_{\text{aq,calc}}^{\text{act}}$ values of these three C-centered radicals are still larger than the typical values (-20 to

-25 kcal/mol). This indicates that the functional group directly neighboring the N–NO functional group affects the slow reaction of molecular oxygen addition to $\cdot\text{CH}_2\text{CH}_2\text{NNOCH}_3$. Given that the other reaction pathways of the three C-centered radicals have either a larger $\Delta G_{\text{aq,calc}}^{\text{act}}$ than that for molecular oxygen addition or include thermodynamically unfavorable reactions ($\Delta G_{\text{aq,calc}}^{\text{react}} > 0$), the formation of peroxy radicals resulting from the addition of molecular oxygen is the dominant reaction pathway in the subsequent NMEA degradation mechanism.

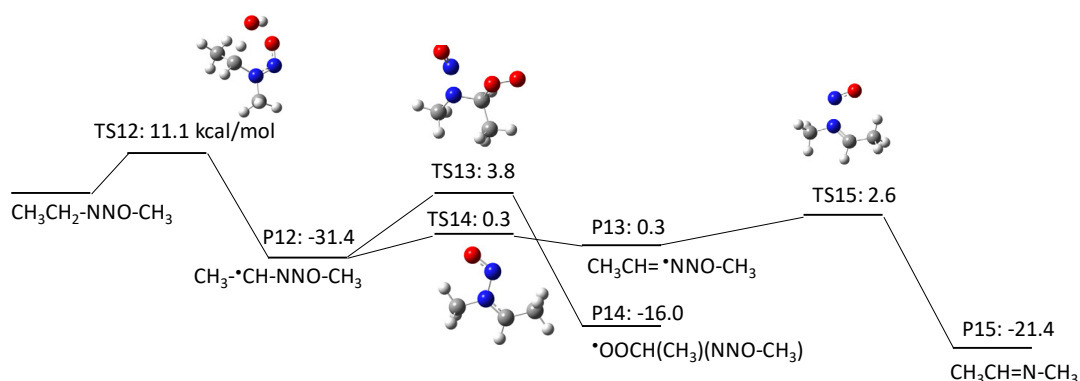


Figure 2.4 Free energy profile for pathway 2-1 of the HO \cdot -induced reaction pathways for NMEA via H abstraction from a C–H bond of the –CH $_2$ – functional group adjacent to the N–NO functional group. The numbers (kcal/mol) are the free energy of activation for the TS and free energy of reaction for the P relative to the corresponding reactant.

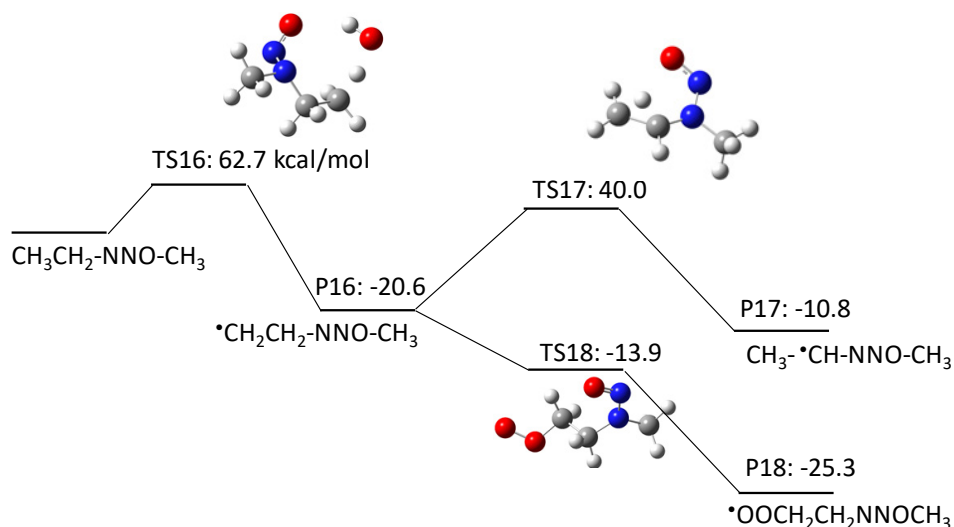


Figure 2.5 Free energy profile for pathway 2-2 of the HO[•]-induced reaction pathways for NMEA via H abstraction from a C-H bond of the terminal CH₃ functional group in the ethyl chain. The numbers (kcal/mol) are the free energy of activation for the TS and free energy of reaction for the P relative to the corresponding reactant.

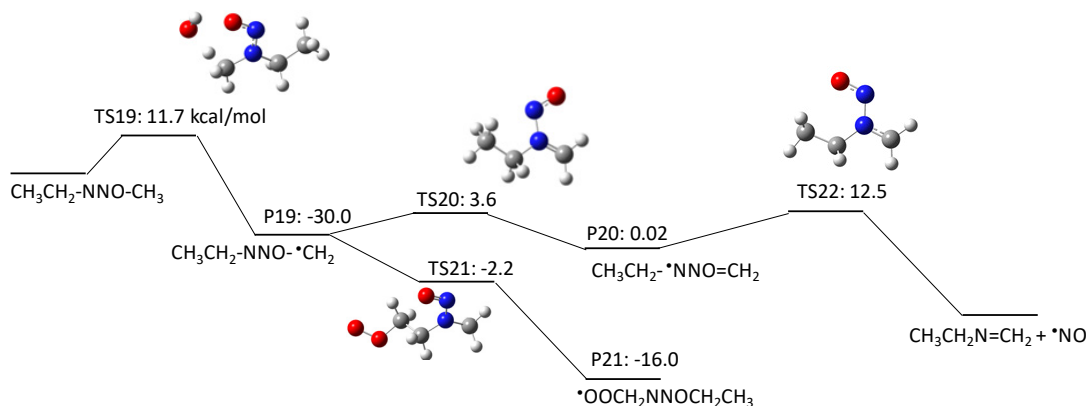


Figure 2.6 Free energy profile for pathway 2-3 of the HO[•]-induced reaction pathways for NMEA via H abstraction from a C-H bond of the terminal CH₃ functional group adjacent to the N-NO functional group. The numbers (kcal/mol) are the free energy of activation for the TS and free energy of reaction for the P relative to the corresponding reactant.

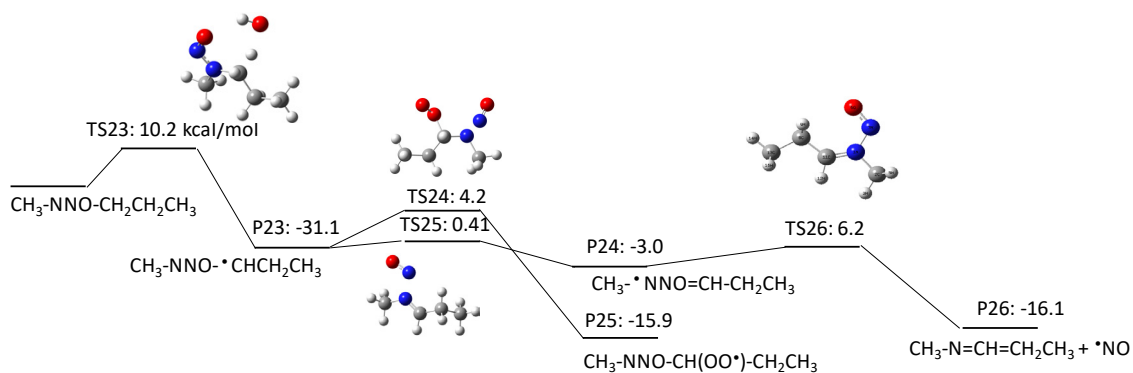
2.3.1.3 N-Nitrosomethylbutylamine (NMBA) Degradation Pathways Induced by HO[•]

NMBA has four potential H abstraction sites from C-H bonds by HO[•]: (1) a C-H bond of the -CH₂- functional group adjacent to the N-NO functional group by pathway 3-1, (2) a C-H bond of the -CH₂ functional group adjacent to the -CH₂- functional groups on both sides by pathway 3-2, (3) a C-H bond of the terminal CH₃ functional group in a butyl chain by pathway 3-3, and (4) a C-H bond of the terminal CH₃ functional group that is adjacent to the N-NO functional group by pathway 3-4. Figures 7-10 show the free

energy profiles per reaction coordinate for each pathway. The calculated $\Delta G_{\text{aq,calc}}^{\text{rct}}$ values are 10.2 kcal/mol for pathway 3–1, 8.3 kcal/mol for pathway 3–2, 10.9 kcal/mol for pathway 3–3, and 11.9 kcal/mol for pathway 3–4. The smaller $\Delta G_{\text{aq,calc}}^{\text{rct}}$ value for pathway 3–2 compared with those for NDMA and NDEA shows consistent reactivity with the experimentally obtained rate constants: $10^9 \text{ M}^{-1}\text{s}^{-1}$ for N-nitrosobutylamine, $4.3 \times 10^8 \text{ M}^{-1}\text{s}^{-1}$ for NDMA and $4.95 \times 10^8 \text{ M}^{-1}\text{s}^{-1}$ for NMEA [16]. The initial H abstraction reactions for all of the pathways are thermodynamically favorable.

Interestingly, we observed distinctive differences in the reactivity of molecular oxygen addition to different C-centered radicals for NMBA. The initial H abstraction from different C–H bonds in NMBA produced $\text{CH}_3\text{NNO}\cdot\text{CHCH}_2\text{CH}_3$ by pathway 3–1, $\text{CH}_3\text{NNOCH}_2\cdot\text{CHCH}_3$ by pathway 3–2, $\text{CH}_3\text{NNO}(\text{CH}_2)_2\cdot\text{CH}_2$ by pathway 3–3, and $\cdot\text{CH}_2\text{NNO}(\text{CH}_2)_2\text{CH}_3$ by pathway 3–4. While molecular oxygen addition to $\text{CH}_3\text{NNO}\cdot\text{CHCH}_2\text{CH}_3$ and $\cdot\text{CH}_2\text{NNO}(\text{CH}_2)_2\text{CH}_3$ have larger $\Delta G_{\text{aq,calc}}^{\text{rct}}$ values of 4.2 kcal/mol and -12.4 kcal/mol, the $\Delta G_{\text{aq,calc}}^{\text{rct}}$ values for $\text{CH}_3\text{NNOCH}_2\cdot\text{CHCH}_3$ (-25.6 kcal/mol) and $\text{CH}_3\text{NNO}(\text{CH}_2)_2\cdot\text{CH}_2$ (-23.9 kcal/mol) are very similar to those that were observed for typical molecular oxygen addition to C-centered radicals. Thus, the alkyl side chain affects the stability of the C-centered radicals and their subsequent reactivity. The significantly slower reaction of molecular oxygen addition to the C-centered radicals produced from NDMA and NMEA may be due to the delocalization of the radical spin density from the formed C-centered radicals onto the N–NO bond(s). This radical delocalization occurs only when a terminal $\cdot\text{CH}_2$ is adjacent to N–NO or $\cdot\text{CH}_2$ neighbors the N–NO functional group. When the alkyl chain contains three CH_2 functional groups, the $\cdot\text{CH}_2$ three positions away from the N–NO functional group does not seem to contribute to the radical delocalization. Thus, the molecular oxygen adds to the C-centered radical without being affected by the delocalization. The different extent of radical delocalization can also explain the lower degradation efficiencies that were observed for NDMA and NEMA (approximately 80~85% degradation efficiency) as compared with nitrosodibutylamine (100% degradation efficiency) [16].

To investigate the effect of the location of the C-centered radical on the occurrence of radical delocalization, we calculated the $\Delta G_{\text{aq,calc}}^{\text{act}}$ values for radical transfer from a C-centered radical to a neighboring C-/N-centered radical. For example, $\text{CH}_3\text{NNO}\cdot\text{CHCH}_2\text{CH}_3$ undergoes radical transfer from a carbon to the amine nitrogen to produce $\text{CH}_3\cdot\text{NNO}=\text{CHCH}_2\text{CH}_3$. This reaction has a $\Delta G_{\text{aq,calc}}^{\text{act}}$ of 0.41 kcal/mol, which indicates a low barrier for this radical delocalization (pathway 3–1). Similarly, $\cdot\text{CH}_2\text{NNO}(\text{CH}_2)_2\text{CH}_3$ requires 3.7 kcal/mol to produce $\text{CH}_2=\cdot\text{NNO}=\text{CHCH}_2\text{CH}_3$ (pathway 3–4). In contrast, $\text{CH}_3\text{NNOCH}_2\cdot\text{CHCH}_3$ requires a $\Delta G_{\text{aq,calc}}^{\text{act}}$ of 38.6 kcal/mol to produce $\text{CH}_3\text{NNO}\cdot\text{CHCH}_2\text{CH}_3$ (pathway 3–2). A similar significantly larger $\Delta G_{\text{aq,calc}}^{\text{act}}$ value of 40.0 kcal/mol was also observed for the radical transfer reaction from $\cdot\text{CH}_2\text{CH}_2\text{NNOCH}_3$ to $\text{CH}_3\cdot\text{CHNNOCH}_3$ via pathway 2–2. Thus, there is a significant barrier for radical transfer from the functional group neighboring the N–NO functional group to the nearest CH_2 group. Therefore, a C-centered radical in $\cdot\text{CH}_2\text{CH}_2\text{NNOCH}_3$ or $\text{CH}_3\text{NNOCH}_2\cdot\text{CHCH}_3$ would rather undergo molecular oxygen addition than radical transfer to produce $\text{CH}_3\cdot\text{CHNNOCH}_3$ or $\text{CH}_3\text{NNO}\cdot\text{CHCH}_2\text{CH}_3$, respectively.



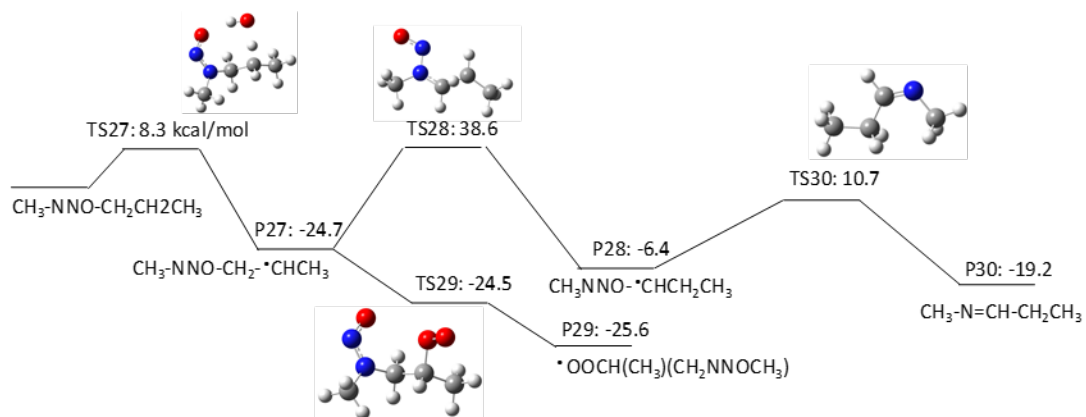


Figure 2.8 Free energy profile for pathway 3–2 of the HO \cdot -induced reaction pathways for NMBA via H abstraction from a C–H bond of the -CH $_2$ functional-group adjacent to the -CH $_2$ - functional groups on both sides. The numbers (kcal/mol) are the free energy of activation for the TS and free energy of reaction for the P relative to the corresponding reactant.

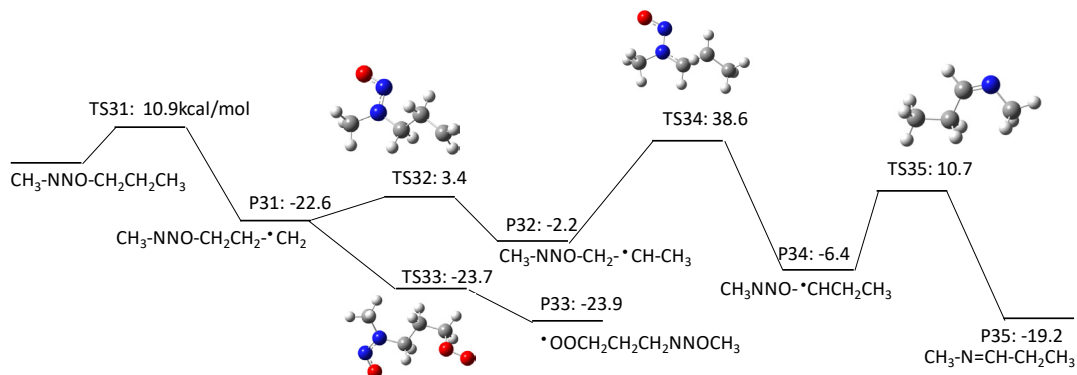


Figure 2.9 Free energy profile for pathway 3–3 of the HO \cdot -induced reaction pathways for NMBA via H abstraction from a C–H bond of the terminal CH $_3$ functional group in a butyl chain. The numbers (kcal/mol) are the free energy of activation for the TS and free energy of reaction for the P relative to the corresponding reactant.

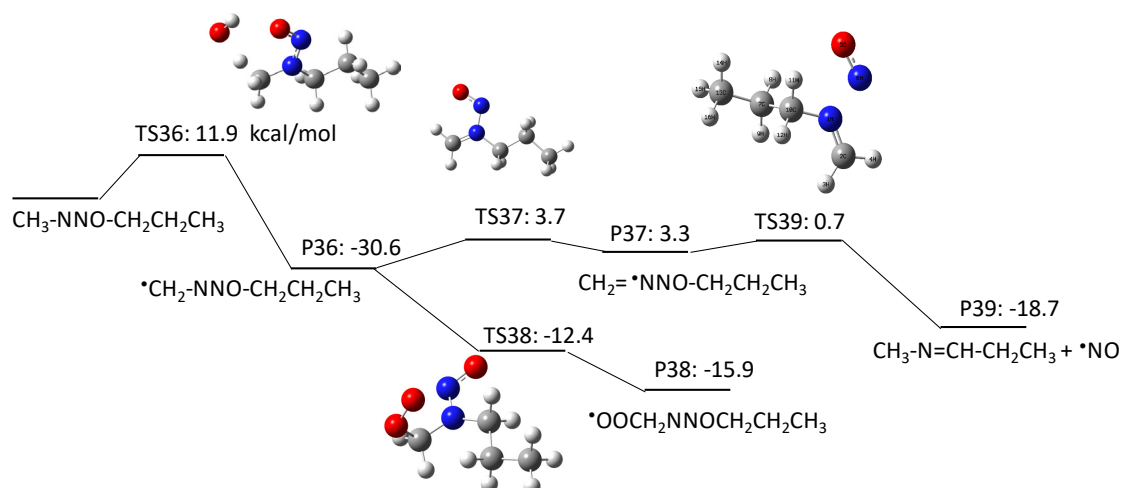


Figure 2.10 Free energy profile for pathway 3–4 of the HO[•]-induced reaction pathways for NMBA via H abstraction from a C–H bond of the terminal CH₃ functional group adjacent to the N–NO functional group. The numbers (kcal/mol) are the free energy of activation for the TS and free energy of reaction for the P relative to the corresponding reactant.

2.3.2 UV-Induced Degradation

2.3.2.1 NDMA Degradation Pathways Induced by UV Photolysis

NDMA absorbs photons at a wavelength of 228 nm with a molar absorptivity of 7380 M⁻¹cm⁻¹ and quantum yield of 0.13 at pH 7 [15]. At a wavelength of 253.7 nm, where a typical low-pressure UV lamp emits photons, the molar absorptivity was reported to be 1650 M⁻¹s⁻¹, and the quantum yield was 0.24 at pH 7 [15]. Another smaller peak is observed at approximately 350 nm. Our TD-DFT calculation obtained one major and one minor peak at 212 nm and 341 nm, respectively. The molecular orbitals that were responsible for the π→π* and n→π transitions at 212 nm and 341 nm are shown in Figure 11. At 212 nm, the N–N bond comprises the highest occupied molecular orbital (HOMO), whereas the C–N bond comprises the HOMO at 341 nm. This analysis indicates that the N–N bond is susceptible breakage under photolysis with a low-pressure UV lamp. This finding is consistent with the experimental findings that were reported in the previous literature.

The UV photolysis-induced NDMA degradation pathways were extensively studied [23, 24]. According to their studies, NDMA undergoes three major degradation pathways induced by UV photolysis: (1) formation of an aminium radical [(CH₃)₂N(+)H] and nitric oxide (*NO) resulting from homolytic cleavage of the N–N bond (pathway 4–1 in Figure

12), (2) formation of dimethylamine $[(\text{CH}_3)_2\text{NH}_2^+]$ and nitrous acid (HNO_2) resulting from heterolytic photocleavage of the N–N bond facilitated by a water molecule (pathway 4–2 in Figure 13), and (3) formation of N-methylidenemethylamine $[(\text{CH}_2=\text{N}(+)\text{HCH}_3]$, $\cdot\text{NO}$, and a superoxide anion radical ($\cdot\text{O}_2^-$) in the presence of dissolved oxygen (i.e., triplet state of $^3\text{O}_2$) (pathway 4–3 in Figure 14).

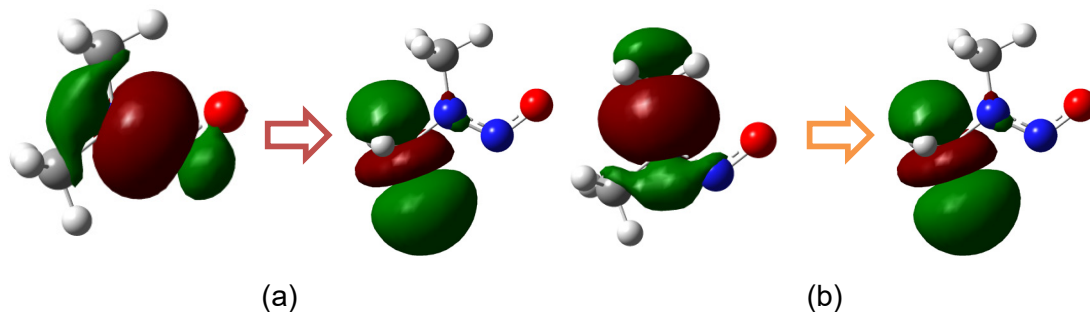


Figure 2.11 HOMO and lowest unoccupied molecular orbital (LUMO) of the $\pi \rightarrow \pi^*$ (a) and $n \rightarrow \pi^*$ (b) transitions at 212 nm and 341 nm, respectively.

The products of $(\text{CH}_3)_2\text{N}(+)\text{H}$ and $\cdot\text{NO}$ in pathway 4–1 react in a solvent cage to produce N-methylidenemethylamine $[(\text{CH}_2=\text{N}(+)\text{HCH}_3]$ and nitroxyl (HNO). Our calculation obtained a $\Delta G_{\text{aq,calc}}^{\text{act}}$ of 1.6 kcal/mol for this reaction. Then, N-methylidenemethylamine undergoes rapid hydrolysis to produce methylamine (CH_3NH_2^+) and formaldehyde (HCHO). A total of 99% of the HCHO is hydrolyzed to form a geminal diol in the aqueous phase [44]; therefore, the hydrated form of HCHO [i.e., $\text{CH}_2(\text{OH})_2$] exists in the aqueous phase. $\text{CH}_2(\text{OH})_2$ reacts with $\text{HO}\cdot$ via H abstraction to produce $\cdot\text{CH}(\text{OH})_2$ with a $\Delta G_{\text{aq,calc}}^{\text{act}}$ of 10.0 kcal/mol. As was examined in the $\text{HO}\cdot$ -induced pathways, this C-centered radical reacts with molecular oxygen to produce a peroxy radical [i.e., $\cdot\text{OOCH}(\text{OH})_2$] ($\Delta G_{\text{aq,calc}}^{\text{act}}$ of -34.9 kcal/mol). The peroxy radical undergoes uni/bimolecular decay to produce stable lower-molecular-weight products [45]. When $\cdot\text{OOCH}(\text{OH})_2$ undergoes unimolecular decay (i.e., $\text{HO}_2\cdot$ elimination), formic acid (HCOOH) is produced ($\Delta G_{\text{aq,calc}}^{\text{act}}$ of 31.6 kcal/mol), which has been experimentally observed [46].

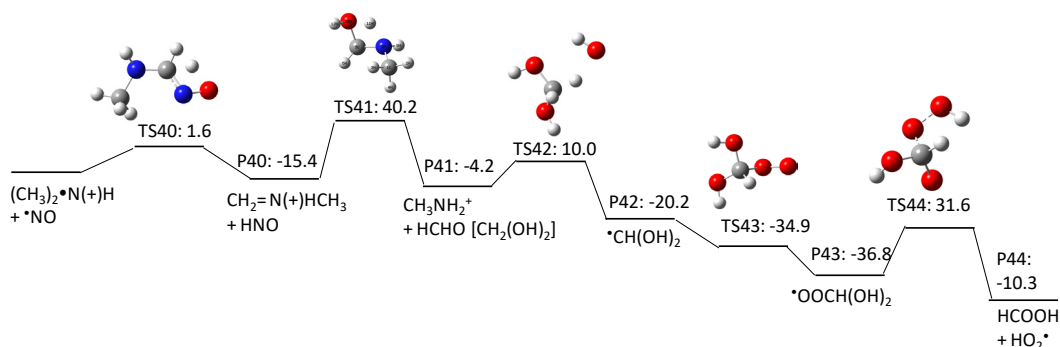


Figure 2.12 Free energy profile for pathway 4–1 of the HO[•]-induced reaction pathways for NDMA photolysis.

One of the C–H bonds in the methyl group of the dimethylamine produced in pathway 4–2 undergoes H abstraction by HO[•] to produce a C-centered radical with a $\Delta G_{\text{aq,calc}}^{\text{act}}$ of 13.9 kcal/mol. Molecular oxygen adds to the C-centered radical to produce a peroxy radical with a $\Delta G_{\text{aq,calc}}^{\text{act}}$ of -15.0 kcal/mol, and the peroxy radical undergoes subsequent uni/bimolecular decay.

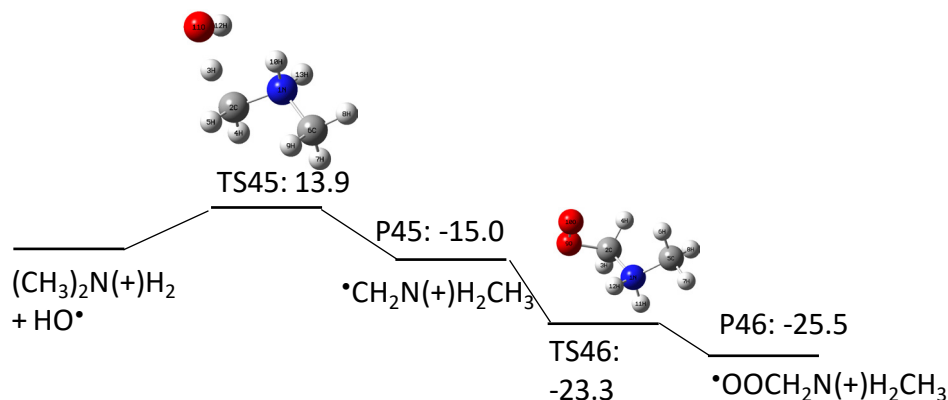


Figure 2.13 Free energy profile for pathway 4–2 of the HO[•]-induced reaction pathways for NDMA photolysis.

The products of •NO and •O₂⁻ from pathway 4–3 react in a solvent cage to produce peroxyxynitrite (ONOO⁻) with a $\Delta G_{\text{aq,calc}}^{\text{act}}$ of 1.72 kcal/mol. The rate constant for this reaction was determined to be $(4.3 - 7.6) \times 10^9 \text{ M}^{-1}\text{s}^{-1}$ [47, 48]. Then, ONOO⁻ undergoes rearrangement with a $\Delta G_{\text{aq,calc}}^{\text{act}}$ of 57.8 kcal/mol to produce a nitrate ion (NO₃⁻). This rearrangement was proposed as isomerization by Anbar and Taube (1954) [49]. ONOO⁻ also reacts with HO₂[•]/O₂^{•-} via single electron transfer to produce an •OONO radical. Our

calculation indicates that this reaction is barrierless, with a $\Delta G_{\text{aq,calc}}^{\text{act}}$ of -16.2 kcal/mol, but the reaction is not thermodynamically favorable ($\Delta G_{\text{aq,calc}}^{\text{react}}$ of 3.4 kcal/mol). Finally, the $\cdot\text{OONO}$ radical undergoes cleavage with a $\Delta G_{\text{aq,calc}}^{\text{react}}$ of -0.56 kcal/mol to produce $\cdot\text{NO}$.

When nitrate undergoes UV photolysis, a nitrite ion (NO_2^-) and $\text{NO}_2\cdot$ are produced. Then, $\text{NO}_2\cdot$ reacts with $\text{HO}\cdot$, $\text{O}_2\cdot^-$, or $\text{NO}_2\cdot$ with a $\Delta G_{\text{aq,calc}}^{\text{react}}$ of 48.3 kcal/mol, 40.2 kcal/mol, or 100.6 kcal/mol to produce ONOOH , $\text{NO}_2^-/\text{NO}_3^-$, or N_2O_4 , respectively. Although the disproportionation of $\text{NO}_2\cdot$ has the largest free energy barrier, the reaction product, N_2O_4 , undergoes hydrolysis to produce NO_3^- and NO_2^- .

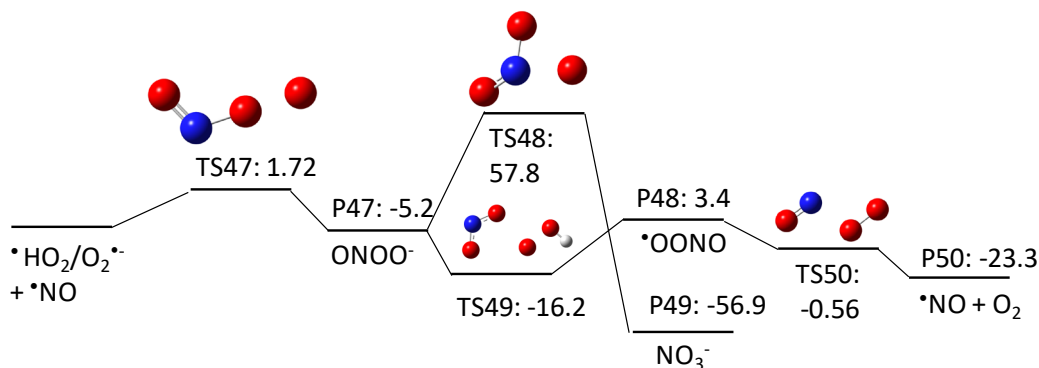


Figure 2.14 Free energy profile for pathway 4–3 of the $\text{HO}\cdot$ -induced reaction pathways for NDMA photolysis.

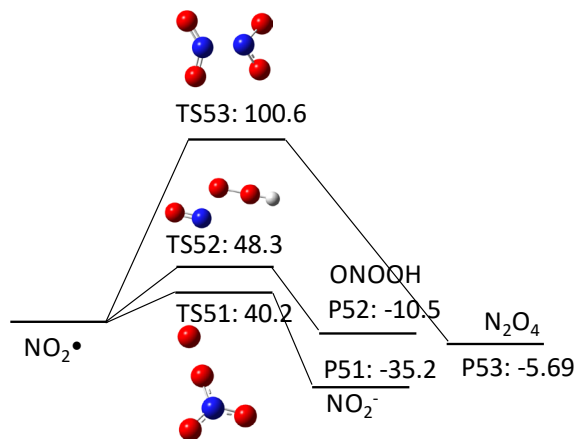


Figure 2.15 Free energy profile for pathway 4–3 of the $\text{HO}\cdot$ -induced reaction pathways for NDMA photolysis.

2.3.3 Environmental Implication and Future Study

Nitrosamines, and NDMA in particular, are extremely potent carcinogenic contaminants in water. The concentration at which NDMA shows potent carcinogenicity is extremely low (0.7 ng/L) [9]. Experimentally investigating the ng/L fate of many chemical contaminants during water treatment processes is time consuming and expensive. Our computational study highlights the usefulness of QM calculations to reveal the elementary reaction pathways that are embedded in the overall reaction pathways that are typically identified by analytical techniques. This technique becomes more useful when the contaminant concentrations are below the analytical detection limit.

Once the elementary reaction pathways are identified, the reaction rate constants should be determined or predicted to calculate the reaction rate of each molecule or species involved in each elementary reaction step. By combining the elementary reaction pathways and the reaction rate constants, one can predict the time-dependent concentration profiles of a target chemical contaminant and its transformation products. This elementary-reaction-based kinetic model could be used as an initial screening tool for many potentially toxic chemical contaminants to estimate the fate of degradation pathways. Our efforts towards the development of such elementary-reaction-based kinetic model are underway.

3 The Fate of N-Nitrosodimethylamine (NDMA) Degradation in Aqueous-phase UV Photolysis²

3.1 Introduction

The trace organic pollutant category nitrosamines poses high potential carcinogenicity and is of serious concern about adverse human health and ecotoxicological effects. Among N-nitrosamines, N-nitrosodimethylamine (NDMA) is on the EPA priority pollutant list and is formed as a byproduct of chloramination and chlorine disinfection as well as a byproduct of industrial processes. In drinking water, the EPA has determined a screening level of 0.11 ng/L for a 10^{-6} lifetime excess cancer risk [9]. NDMA is a small neutral compound that can pass through membrane filtration and reverse osmosis processes.

Ultraviolet (UV)-based water treatment technology is the promising technology to degrade NDMA. UV photolysis for the attenuation of NDMA in groundwater and drinking water was performed at full scales. The absorbance of photons by the compound of interest, creates an excited species that begins the photochemical degradation pathways. These chain reactions lead to a variety of radical-intermediates and transformation byproducts and the mechanisms by which they form are not well understood. UV photolysis can be used to remove NDMA because of its high molar absorptivity (1650 L/mol cm at 253.7 nm) [16, 17]. UV treatment technologies are also known to effectively degrade other N-nitrosamine compounds because of their strong photolability. NDMA's highest absorbance peak is between 225 and 250 nm with a smaller second peak occurring between 300 and 350 nm. These peaks are within the range emitted by medium pressure lamps and close to that emitted by low pressure lamps, both of which are commonly used in water treatment applications [15, 22]. The quantum yield depends on pH and wavelength with various primary quantum yields having been reported in the literature under air saturated conditions for NDMA [24, 50]. Lee reported a primary quantum yield of 0.3 at 254 nm of wavelength at both pH 3 and 7 under O₂ saturation and 0.206 in deaerated solution [23].

² The material contained in this chapter is in preparation for submission to a journal

Although the photochemical reactions of NDMA under UV irradiation have been studied at various conditions and the major degradation pathways and transformation products were reported, the complete reaction mechanisms and the kinetics have not been elucidated yet. Early studies on the degradation of nitrosamine species in the 1960s determined that symmetry of nitrosamine impacts the products formed and that under acidic conditions photolysis pathways were altered [51, 52]. Grover et al in 1987, proposed that through the degradation of nitrosamines using UV light, carbon centered radicals were formed [53]. In 2002, Stefan and Bolton published results of NDMA decay by a 1kWh medium pressure Hg lamp, with intensity of $(3.03 \pm 0.08) \times 10^{-4}$ einsteins s^{-1} , with a focus on byproduct formation and kinetics of the photolysis reactions at both pH 3 and 7. Major byproducts were identified as dimethylamine (DMA) and nitrite with nitrate, formaldehyde, and formic acid [22]. Analysis of the pathways by which NDMA undergoes photolysis were expanded upon by Lee et al in 2005 [23] in which the pH and dissolved oxygen concentration was varied to determine the impact on byproduct formation. According to their studies, NDMA undergoes three major degradation pathways induced by UV photolysis: (1) formation of an aminium radical $[(CH_3)_2N(+)H]$ and nitric acid ($\cdot NO$) resulting from homolytic cleavage of the N-N bond; (2) formation of dimethylamine $[(CH_3)_2NH_2^+]$ and nitrous acid (HNO_2) resulting from heterolytic photocleavage of the N-N bond facilitated by a water molecule; and (3) formation of N-methylidenemethylamine $[(CH_2=N(+)H)CH_3]$, $\cdot NO$, and a superoxide anion radical ($\cdot O_2^-$) in the presence of dissolved oxygen (i.e., triplet state of 3O_2). Kwon et al, similar to Lee et al, looked at the initial pathways and byproducts of NDMA photolysis, however, focused on the formation on nitrate and nitrite ions. Previous studies suggested that the formation of nitrate was a result of the presence of peroxyxynitrite ($ONOO^-$) but Kwon et al showed this is not possible due to the pKa value of peroxyxynitrite relative to the acidic conditions in the study. Rather a new mechanism for the creation of nitrate is proposed [25, 26]. The initial pathways through which NDMA degrades by UV photolysis are well understood and some of the subsequent reactions involving the products of the initial pathways have been identified. Work still needs to be done to understand all reactions that produce stable byproducts and determine the rate at which they are occurring.

As nitrate and nitrite are the major byproducts of NDMA photolysis, it is important to consider the reactions they go through, specifically their photolysis pathways. The

prediction of reaction mechanisms involved in nitrate/ nitrite photolysis is still being investigated today. Flash photolysis experiments in 1980 resulted in a simplistic explanation for potential reaction mechanisms with experiments of nitrate and nitrite photolysis as they relate to AOPs being done in 1994 [54, 55]. In 1999, Mack and Bolton, broke down the plausible reaction pathways for both nitrate and nitrite photolysis and discussed how all the reactions could be interconnected, with many of the reactions considered unknown [56]. These reactions were then further supplemented with those in a review by Tugaoen et al in 2017 which focused on nitrate reactions [57]. Major obstacles result from the fact that numerous multi-step elementary reactions via various reaction pathways produce identical stable-byproducts in both the photolysis of NDMA and nitrate/ nitrite. This makes it difficult to identify the important elementary reactions and to determine their associated reaction rate constants experimentally. The coupling of experiments with theoretical investigations can provide mechanistic insights into elementary reaction mechanisms for nitrogenous species. The creation of a kinetic based model for NDMA photolysis based on reaction pathways and rate constants has not yet been done.

Quantum mechanical (QM) calculations using *ab initio* methods or density functional theory (DFT) are attractive approaches to identify elementary reaction pathways and the kinetics of complex fast radical reactions. QM calculations have been used to support experimentally identified reaction pathways by calculating the reaction energy using statistical thermodynamics [8]. A high-level multi-point energy method was used to calculate the aqueous-phase free energies of activation for HO[•]-induced reactions of a wide variety of organic compounds, including aliphatic compounds, alkenes, and aromatic compounds.

This study aims to elucidate photolysis reaction mechanisms of NDMA by developing an elementary reaction-based kinetic model. The elementary reaction pathways and the reaction rate constants were determined with theoretical calculations using *ab initio* and density functional theory (DFT) quantum mechanical calculations. By combining the identified reaction pathways and kinetics, an ordinary differential equation for all species will be developed and solved numerically to obtain the time-dependent concentration profiles of NDMA and the products. This is the first study to develop an elementary

reaction-based kinetic model for the photochemical reaction of NDMA and nitrogen-containing species.

3.2 Materials and Methods

All experimental values for NDMA and subsequent byproducts were taken from Lee et al, *UV Photolytic Mechanism of N-Nitrosodimethylamine in Water: Roles of Dissolved Oxygen and Solution pH* [23]. The model used is a modified AdOx model that allows for non-steady state solutions and can solve charge balance equations. Due to the stiffness of the ordinary differential equations (ODEs) used for determining the time dependent concentration profile, Gear's backward differential formula was used [58, 59]. This multi-step method was used over others due to the ability to estimate error and correct the predicted points as it iterates. The Dgear method has been successfully applied for various kinetic models in AOPs [35, 60, 61].

By calculating the charge balance at each time step, the change in pH can be found and the model can determine dissociation of all species at the new pH. This modified AdOx model is run using Microsoft Visual Studios 2013 Professional and Intel Parallel Studio XE 2015 with IMSL FORTRAN Numerical Library [62]. The input files allows the user to change the number of species present in the reactor and at what concentrations they are present at initialization. Users also control the number of available reactions and the rate they occur at. For species that dissociate, the pKa is able to be specified. Other input parameters, listed in Table 3.1, were input in the model to replicate the laboratory conditions from the Lee et al study [23].

Table 3.1 Input parameters for simulation from Lee experiment [23]

	Model Inputs	
Reactor Type	CMBR	
Tank Volume	0.15 L	
Time Step	1 sec	
Lamp	13W low pressure mercury vapor lamp at 253.7 nm	
Optical Pathlength	2 cm	
Alkalinity	0 mg/L as CaCO ₃	
UV Intensity	1.87 x 10 ⁻⁶ einsteins/L/s	
Initial pH	3.0	7.0
Model Run Time	30 min	300 min
Initial NDMA Concentration	0.0001 M	0.01 M

All QM calculations were performed with the Gaussian 09 revision D.02 program using the Michigan Tech high-performance cluster “Superior” and homemade LINUX workstations. The UV-induced reaction pathways with NDMA were calculated with the Gaussian-4 theory (G4). The aqueous-phase structures and frequencies were obtained using an implicit polarizable continuum model [universal solvation model (SMD)]. Previously, we verified the combination of M06-2X/cc-pVDZ or G4 with the SMD model by successfully applying it to other aqueous-phase radical-involved reactions.

3.3 Results and Discussion

3.3.1 Elementary Reaction Pathways After Initial Photolysis of NDMA

The initial photolysis of NDMA undergoes three major degradation mechanisms: (1) formation of an aminium radical [(CH₃)₂N(+•)H] and nitric acid (•NO) resulting from homolytic cleavage of the N-N bond (pathway 1), (2) formation of dimethylamine [(CH₃)₂NH₂⁺] and nitrous acid (HNO₂) resulting from heterolytic photocleavage of the N-N bond facilitated by a water molecule (pathway 2), and (3) formation of N-methylenemethylamine [(CH₂=N(+•)HCH₃], •NO, and a superoxide anion radical (•O₂⁻) in the qwtew78 (i.e., triplet state of ³O₂) (pathway 3) [23]. These pathways are illustrated by the pink (pathway 1), teal (pathway 2), and yellow arrow (pathway 3), in Figure 3.1.

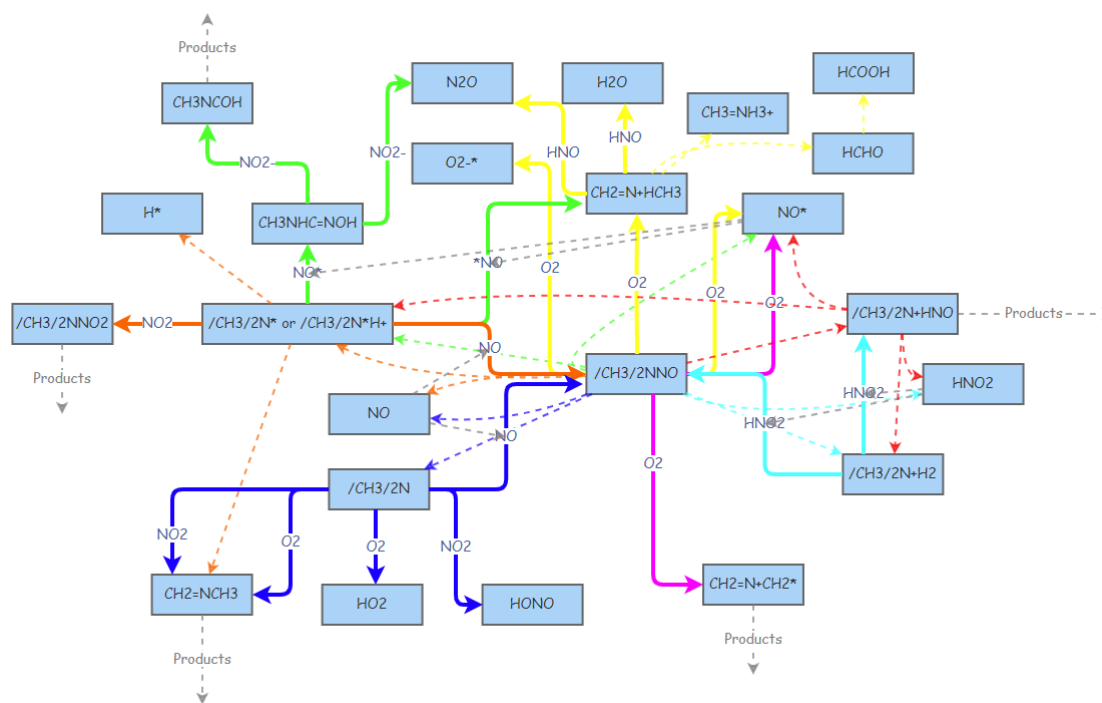


Figure 3.1 NDMA photolysis pathways and subsequent reactions. Radicals are indicated with an asterisk and double bonds with an equal sign. Solid colored arrows with compounds listed on them indicate the product (end of arrow) requires both compound at start of arrow and one indicated on arrow in order to be produced. Dashed colored arrows indicate decay reactions in which no additional reactants are needed to form the product(s). Dashed grey lines are used to show how reaction products are used in future reactions as reactants.

The products of $(\text{CH}_3)_2\text{N}^+(\text{H})$ and $\cdot\text{NO}$ in pathway 1 react in a solvent cage to produce N-methylidenemethylamine $[(\text{CH}_2=\text{N}^+)\text{HCH}_3]$ and nitroxyl (HNO). Our calculation obtained the aqueous-phase free energy of activation of 1.6 kcal/mol for this reaction. Then, N-methylidenemethylamine undergoes rapid hydrolysis to produce methylamine (CH_3NH_2^+) and formaldehyde (HCHO). A total of 99% of the HCHO is hydrolyzed to form a geminal diol in the aqueous phase; therefore, the hydrated form of HCHO [i.e., $\text{CH}_2(\text{OH})_2$] exists in the aqueous phase [44]. $\text{CH}_2(\text{OH})_2$ reacts with HO^\cdot via H abstraction to produce $\cdot\text{CH}(\text{OH})_2$ with a $\Delta G_{\text{aq,calc}}^{\text{act}}$ of 10.0 kcal/mol. As was examined in the HO^\cdot -induced pathways, this C-centered radical reacts with molecular oxygen to produce a peroxy radical [i.e., $\cdot\text{OOC}(\text{OH})_2$] (-34.9 kcal/mol of the aqueous-phase free energy of activation). The peroxy radical undergoes uni/bimolecular decay to produce stable lower-molecular-weight products. When $\cdot\text{OOC}(\text{OH})_2$ undergoes unimolecular decay (i.e., HO_2^\cdot elimination), formic acid (HCOOH) is produced (aqueous phase free energy of

activation), which has been observed experimentally. The methylamine (CH_3NH_2^+) undergoes H-atom abstraction by either HO^\bullet or NO^\bullet to produce a carbon-centered radical ($^\bullet\text{CH}_2\text{NH}_2^+$) that further react with molecular oxygen to produce peroxy radicals.

One of the C-H bonds in the methyl group of the dimethylamine produced in pathway 2 undergoes H-atom abstraction by HO^\bullet to produce a C-centered radical with 13.9 kcal/mol of free energy of activation. Molecular oxygen adds to the C-centered radical to produce a peroxy radical with -15.0 kcal/mol of aqueous-phase free energy of activation, and the peroxy radical undergoes subsequent uni-/bi-molecular decay. Dimethylamine also undergoes H-atom abstraction by NO^\bullet to produce a C-centered with 4.63 kcal/mol of free energy of activation.

The products of $^\bullet\text{NO}$ and $^\bullet\text{O}_2^-$ from pathway 3 react in a solvent cage to produce peroxyxynitrite (ONOO^-) with 2.0 kcal/mol of aqueous-phase free energy of activation. The rate constant for this reaction was determined to be $(4.3\text{-}7.6) \times 10^9 \text{ M}^{-1}\text{s}^{-1}$. Depending on the solution pH, $^\bullet\text{NO}$ also reacts with HO_2^\bullet to produce peroxyxynitric acid (ONOOH) and the calculated free energy of activation was 1.72 kcal/mol. The experimentally determined k value was $3.2 \times 10^9 \text{ M}^{-1}\text{s}^{-1}$. The pKa of ONOOH is 6.6. The $\text{ONOOH}/\text{ONOO}^-$ undergoes rearrangement with 57.8 kcal/mol of aqueous-phase free energy of activation to produce a nitrate ion (NO_3^-) and the experimental k was determined as 1.11 s^{-1} . This rearrangement was proposed as isomerization by Anbar and Taube [49]. ONOO^- also reacts with $\text{HO}_2^\bullet/\text{O}_2^-$ via single electron transfer to produce an $^\bullet\text{OONO}$ radical. Our calculation indicates that this reaction is barrierless with -16.2 kcal/mol of aqueous-phase free energy of activation, but the reaction is not thermodynamically favorable (3.4 kcal/mol of aqueous-phase free energy of activation). The $\text{ONOO}^-/\text{ONOOH}$ is known to behave like HO^\bullet and abstract H-atom from a C-H bond of hydrolyzed form of formaldehyde (i.e., diol). Our calculated free energies of activation for these reactions were 42 kcal/mol for ONOO^- and 44.2 kcal/mol for ONOOH . The nitric acid ($^\bullet\text{NO}$) is a reactive radical species and reacts with other active radicals such as HO^\bullet , NO_2^\bullet , and NO^\bullet . Finally, the $^\bullet\text{OONO}$ radical undergoes cleavage with -0.56 kcal/mol of aqueous-phase free energy of activation to produce $^\bullet\text{NO}$.

When nitrate undergoes UV photolysis, an excited state nitrate is created that can then form a nitrite ion (NO_2^-) or NO_2^\bullet [57, 63, 64]. Then, NO_2^\bullet reacts with HO^\bullet , O_2^- , or NO_2^\bullet

with 48.3 kcal/mol, 40.2 kcal/mol, or 100.6 kcal/mol of aqueous-phase free energies of activation to produce ONOOH, $\text{NO}_2^-/\text{NO}_3^-$, or N_2O_4 , respectively. Although the disproportionation of NO_2^\cdot has the largest free energy barrier, the reaction product, N_2O_4 , undergoes hydrolysis to produce NO_3^- and NO_2^- . Nitrite photolysis results in the formation of NO_2^\cdot that can then form NO^\cdot and O_2^\cdot , with O_2^\cdot often being protonated to form HO_2^\cdot [57, 65]. Formation of NO^\cdot can also occur due to the degradation of ONOO^\cdot or as a major photolysis product of ONOO^- [56]. Depending upon the pH of the solution, if HNO_2 is present, it can undergo photolysis and has a higher quantum yield than nitrite [56, 57, 66]. NO^\cdot is able to react with other radical species including NO_2^\cdot and O_2^\cdot to form dinitrogen trioxide (N_2O_3) and peroxyxynitrite/peroxyxynitrous acid ($\text{ONOO}^-/\text{ONOOH}$) respectively [56]. However, the formation of peroxyxynitrite/peroxyxynitrous acid is considered a secondary reaction and is minor compared to other pathways [57, 67]. Formation of O_2^\cdot occurs during photolysis of NDMA. Dinitrogen trioxide in the presence of water can produce two nitrite ions through hydrolysis [56, 57]. Species formed from the photolysis of NDMA, such as HNO_2 and NO^\cdot , feed into reactions involved in nitrate/nitrite photolysis. Figure 3.2 shows nitrate and nitrite reactions that can occur during the photolysis of NDMA.

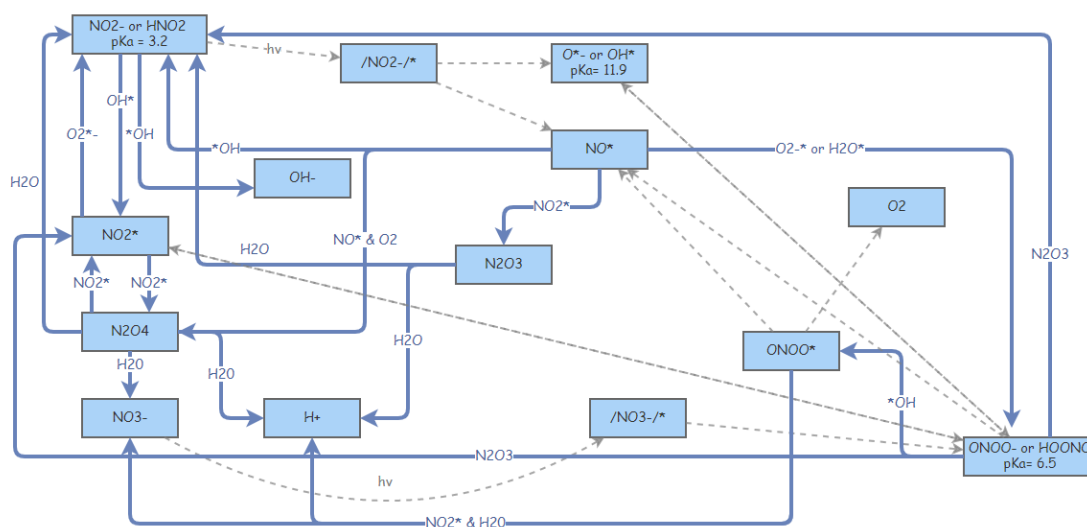


Figure 3.2 Nitrate and nitrite photolysis pathways and the transformation products. Radicals are indicated with an asterisk and double bonds with an equal sign. Solid colored arrows with compounds listed on them indicate the product (end of arrow) requires both original compound at start of arrow and one indicated on arrow in order to be produced. Dashed arrows indicate decay reactions in which no additional reactants are needed to form the product(s).

3.3.2 Quantum Yields and Reaction Rate Constants

Table 3.2 summarizes the identified photolysis reactions with each quantum yield determined in this study and used as input into the simulation. The quantum yield for each photolysis reaction was determined by fitting with the experimentally determined overall values at both pH values. The sum of all pathway quantum yields results in the overall measured quantum yield value as detailed in Li et al [68]. For example, at both pH 3 and pH 7, the overall quantum yield was reported as 0.31, regardless of the solution pH in the region of pH 2-8, in the saturated O₂ solution. It is noted that the quantum yield drops from 0.3 to almost 0 as the pH value increased from 4 to 10, indicating that the dissolved oxygen is responsible for the formation of subsequent excited species resulting from the NDMA photolysis.

Table 3.2 Photolysis reactions as input in code with quantum yield values for each pH tested. Note that the code is only able to produce one to one ratios for photolysis reactions so some reactions with multiple products were split into several reactions.

Reaction	Φ at pH 3	Φ at pH 7
H ₂ O ₂ → HO [•]	1	1
(CH ₃) ₂ N-NO → (CH ₃) ₂ N [•] H	0.051	0.15
(CH ₃) ₂ N-NO → [•] NO	0	0.046
(CH ₃) ₂ N-NO → [•] NO	0.001	0.001
(CH ₃) ₂ N-NO → O ₂ ^{•-}	0.14	0.15
(CH ₃) ₂ N-NO → CH ₃ N ⁺ H=CH ₂	0.27	0.6
(CH ₃) ₂ N-NO → (CH ₃) ₂ NH ₂ ⁺	0.18	0.4
(CH ₃) ₂ N-NO → HNO ₂	0.102	0.27
NO ₂ ⁻ → [•] NO	0	0.046
NO ₂ ⁻ → O ^{•-}	0	0.046
HNO ₃ → NO ₂ ⁻	0.31	0.19

The reaction rate constants used in this study are shown in Table 3.3. The elementary reaction pathways were listed based on Figures 3.1 and 3.2. For those reactions without literature sources listed, reactions and rate constants were estimated through QM calculations.

Table 3.3 Input irreversible reactions for compounds considered in the code

Reaction	Rate Constant	Units	Source
$\text{H}_2\text{O}_2 + \text{HO}^\bullet \rightarrow \text{HO}_2^\bullet + \text{H}_2\text{O}$	2.7×10^7	$\text{M}^{-1} \text{s}^{-1}$	[26, 69]
$\text{HO}^\bullet + \text{HO}_2^\bullet \rightarrow \text{HO}_2^\bullet + \text{OH}^\bullet$	7.5×10^9	$\text{M}^{-1} \text{s}^{-1}$	[70]
$\text{H}_2\text{O}_2 + \text{HO}_2^\bullet \rightarrow \text{HO}^\bullet + \text{H}_2\text{O} + \text{O}_2$	3	$\text{M}^{-1} \text{s}^{-1}$	[71]
$\text{H}_2\text{O}_2 + \text{O}_2^{\bullet -} \rightarrow \text{HO}^\bullet + \text{OH}^- + \text{O}_2$	0.13	$\text{M}^{-1} \text{s}^{-1}$	[72]
$\text{HO}^\bullet + \text{CO}_3^{2-} \rightarrow \text{CO}_3^{\bullet -} + \text{OH}^-$	3.9×10^8	$\text{M}^{-1} \text{s}^{-1}$	[57, 69]
$\text{HO}^\bullet + \text{HCO}_3^- \rightarrow \text{CO}_3^{\bullet -} + \text{H}_2\text{O}$	8.5×10^6	$\text{M}^{-1} \text{s}^{-1}$	[57, 69]
$\text{HO}^\bullet + \text{HPO}_4^{2-} \rightarrow \text{HPO}_4^{\bullet -} + \text{OH}^-$	1.5×10^5	$\text{M}^{-1} \text{s}^{-1}$	[69]
$\text{HO}^\bullet + \text{H}_2\text{PO}_4^- \rightarrow \text{HPO}_4^{\bullet -} + \text{H}_2\text{O}$	2.0×10^4	$\text{M}^{-1} \text{s}^{-1}$	[69]
$\text{H}_2\text{O}_2 + \text{CO}_3^{\bullet -} \rightarrow \text{HCO}_3^- + \text{HO}_2^\bullet$	4.3×10^5	$\text{M}^{-1} \text{s}^{-1}$	[73]
$\text{HO}_2^\bullet + \text{CO}_3^{\bullet -} \rightarrow \text{CO}_3^{2-} + \text{HO}_2^\bullet$	3.0×10^7	$\text{M}^{-1} \text{s}^{-1}$	[73]
$\text{H}_2\text{O}_2 + \text{HPO}_4^{\bullet -} \rightarrow \text{H}_2\text{PO}_4^- + \text{HO}_2^\bullet$	2.7×10^7	$\text{M}^{-1} \text{s}^{-1}$	[74]
$\text{HO}^\bullet + \text{HO}^\bullet \rightarrow \text{H}_2\text{O}_2$	4.2×10^9	$\text{M}^{-1} \text{s}^{-1}$	[57, 69]
$\text{HO}^\bullet + \text{HO}_2^\bullet \rightarrow \text{H}_2\text{O} + \text{O}_2$	6.6×10^9	$\text{M}^{-1} \text{s}^{-1}$	[69]
$\text{HO}_2^\bullet + \text{HO}_2^\bullet \rightarrow \text{H}_2\text{O}_2 + \text{O}_2$	8.3×10^5	$\text{M}^{-1} \text{s}^{-1}$	[75]
$\text{HO}_2^\bullet + \text{O}_2^{\bullet -} \rightarrow \text{HO}_2^\bullet + \text{O}_2$	9.76×10^7	$\text{M}^{-1} \text{s}^{-1}$	[69]
$\text{HO}^\bullet + \text{O}_2^{\bullet -} \rightarrow \text{O}_2 + \text{OH}^-$	7.0×10^9	$\text{M}^{-1} \text{s}^{-1}$	[69]
$\text{HO}^\bullet + \text{CO}_3^{\bullet -} \rightarrow \text{Products not considered}$	3.0×10^9	$\text{M}^{-1} \text{s}^{-1}$	[76]
$\text{CO}_3^{\bullet -} + \text{O}_2^{\bullet -} \rightarrow \text{CO}_3^{2-} + \text{O}_2$	6.0×10^8	$\text{M}^{-1} \text{s}^{-1}$	[77]
$\text{CO}_3^{\bullet -} + \text{CO}_3^{\bullet -} \rightarrow \text{Products not considered}$	3.0×10^7	$\text{M}^{-1} \text{s}^{-1}$	[76]
$(\text{CH}_3)_2\text{N}^\bullet \rightarrow \text{CH}_2\text{-NH-CH}_3$	1.0×10^6	s^{-1}	estimated
$(\text{CH}_3)_2\text{N}^\bullet + \text{H}^\bullet \rightarrow \text{CH}_3\text{N}^\bullet + \text{H}=\text{CH}_2 + \text{HNO}$	7.17×10^8	$\text{M}^{-1} \text{s}^{-1}$	[23]
$\text{CH}_2\text{-NH-CH}_3 + \text{H}^\bullet \rightarrow \text{CH}_3\text{-NH-CH}=\text{NOH}$	1.0×10^8	$\text{M}^{-1} \text{s}^{-1}$	
$\text{CH}_3\text{-NH-CH}=\text{NOH} + \text{NO}_2^\bullet \rightarrow \text{CH}_3\text{-NH-CH}=\text{O} + \text{N}_2\text{O}$	1.0×10^1	$\text{M}^{-1} \text{s}^{-1}$	[23]
$\text{CH}_3\text{N}^\bullet + \text{H}=\text{CH}_2 \rightarrow \text{CH}_3\text{NH}_2 + \text{CH}_2\text{OH}^\bullet$	1.0×10^1	s^{-1}	estimated
$\text{H}^\bullet + \text{O}_2^{\bullet -} \rightarrow \text{ONOO}^\bullet$	1.9×10^9	$\text{M}^{-1} \text{s}^{-1}$	[25, 26, 78]
$\text{CH}_2\text{OH}^\bullet + \text{O}_2 \rightarrow \text{OOCH}_2\text{OH}^\bullet$	1.2×10^9	$\text{M}^{-1} \text{s}^{-1}$	[79]
$2 \text{OOCH}_2\text{OH}^\bullet \rightarrow 2 \text{OCH}_2\text{OH}^\bullet$	8.9×10^8	$\text{M}^{-1} \text{s}^{-1}$	[79]
$\text{OOCH}_2\text{OH}^\bullet \rightarrow \text{HO}_2^\bullet + \text{HCHO}$	48	s^{-1}	[79]
$\text{ONOO}^\bullet \rightarrow \text{NO}_3^-$	1.11	s^{-1}	[65]
$(\text{CH}_3)_2\text{N}^\bullet + \text{H}^\bullet \rightarrow \text{CH}_3\text{N}^\bullet + \text{H}=\text{CH}_2 + \text{NO}^\bullet$	1.0×10^{10}		[23]
$\text{HO}_2^\bullet + \text{H}^\bullet \rightarrow \text{ONOOH}$	3.2×10^9	$\text{M}^{-1} \text{s}^{-1}$	[25]
$2 \text{NO}_2^\bullet \rightarrow \text{N}_2\text{O}_4$	4.5×10^8	$\text{M}^{-1} \text{s}^{-1}$	[56, 57, 80]
$\text{N}_2\text{O}_4 \rightarrow \text{NO}_2^\bullet + \text{NO}_3^-$	1.0×10^3	s^{-1}	[26, 56, 57, 80]
$\text{ONOOH} \rightarrow \text{NO}_3^- + \text{H}^\bullet$	1.4	s^{-1}	[57, 65]
$\text{H}^\bullet + \text{NO}_2^\bullet \rightarrow \text{N}_2\text{O}_3$	1.1×10^9	$\text{M}^{-1} \text{s}^{-1}$	[56, 57, 80]

$N_2O_3 \rightarrow 2 NO_2^-$	5.3×10^2	s^{-1}	[56, 57, 80]
$O_2^- + NO_2^- \rightarrow NO_2^- + O_2$	1.0×10^8	$M^{-1} s^{-1}$	[56, 80, 81]
$\cdot NO + HO^- \rightarrow HNO_2$	1.0×10^{10}	$M^{-1} s^{-1}$	[56, 57, 69, 80]
$NO_2^- + HO^- \rightarrow ONOOH + NO_3^-$	1.3×10^9	$M^{-1} s^{-1}$	[56, 80, 82]
$NO_2^- + HO^- \rightarrow OH^- + NO_2^-$	2.5×10^9	$M^{-1} s^{-1}$	[57, 69]
$2 \cdot NO \rightarrow N_2O_2$	1.0×10^9	$M^{-1} s^{-1}$	[56, 57, 83]
$N_2O_2 + O_2 \rightarrow N_2O_4$	1.0×10^9	$M^{-1} s^{-1}$	[56, 57, 83]
$ONOOH + H_2O \rightarrow NO_3^-$	1.2	s^{-1}	[47]
$ONOO^- + HCHO \rightarrow NO_3^- + HCOOH$	10	$M^{-1} s^{-1}$	[23]
$ONOOH + HCHO \rightarrow NO_3^- + HCOOH$	5	$M^{-1} s^{-1}$	Estimated
$ONOO^- + HO^- \rightarrow ONOO^- + OH^-$	5.0×10^9	$M^{-1} s^{-1}$	[56]
$ONOOH + HO^- \rightarrow ONOO^- + H_2O$	1.0×10^9	$M^{-1} s^{-1}$	Estimated
$ONOO^- + NO_2^- \rightarrow 2 NO_3^-$	1.0×10^9	$M^{-1} s^{-1}$	Estimated
$HO_2^- + NO_2^- \rightarrow NO_3^- + O_2$	5.0×10^4	$M^{-1} s^{-1}$	Estimated
$HCOOH + HO^- \rightarrow \cdot COOH + H_2O$	4.5×10^7	$M^{-1} s^{-1}$	[79]
$HCOO^- + HO^- \rightarrow \cdot COOH + H_2O$	2.4×10^9	$M^{-1} s^{-1}$	[79]
$\cdot COOH + O_2 \rightarrow \cdot OOCOO^-$	1.0×10^{10}	$M^{-1} s^{-1}$	[79]
$2 \cdot OOCOO^- \rightarrow \cdot OCOO^- + O_2$	8.7×10^9	$M^{-1} s^{-1}$	[79]
$2 \cdot OCOO^- \rightarrow CO_2 + O_2$	7.8×10^9	$M^{-1} s^{-1}$	[79]
$N_2O_4 \rightarrow NO_3^-$	1.11	s^{-1}	[84]
$2 HNO \rightarrow N_2O + H_2O$	8.0×10^6	$M^{-1} s^{-1}$	[57]
$HNO + \cdot NO \rightarrow N_2O + HNO_2$	5.0×10^9	$M^{-1} s^{-1}$	[57]
$NO_3^- \rightarrow NO_2^- + HO^-$	2.3×10^5	s^{-1}	[85]
$NO_3^- \rightarrow H^+ + NO_3^{2-}$	16	s^{-1}	[85]
$NO_3^{2-} \rightarrow NO_2^- + HO^-$	5.5×10^4	s^{-1}	[85]
$CH_2(OH)_2 + HO^- \rightarrow \cdot CH(OH)_2 + H_2O$	1.0×10^9	$M^{-1} s^{-1}$	[79]
$2 \cdot OCH(OH)_2 \rightarrow 2 \cdot OCH(OH)_2$	7.9×10^7	$M^{-1} s^{-1}$	[79]
$2 \cdot OCH(OH)_2 \rightarrow 2 HOC(OH)_2$	7.9×10^7	$M^{-1} s^{-1}$	[79]
$2 \cdot OCH(OH)_2 \rightarrow CH(OH)_3 + HOC(OH)_2$	1	$M^{-1} s^{-1}$	[79]
$\cdot OCH(OH)_2 \rightarrow \cdot HO_2 + HCOOH$	8.7×10^3	s^{-1}	[79]
$\cdot OCH(OH)_2 + HO_2^- \rightarrow CH(OH)_3 + O_2$	2.0×10^6	$M^{-1} s^{-1}$	[79]
$\cdot OCH_2OH \rightarrow HCOOH + HO^-$	6.3×10^6	s^{-1}	[79]
$\cdot CH(OH)_2 + O_2 \rightarrow \cdot OCH(OH)_2$	4.9×10^9	$M^{-1} s^{-1}$	[79]

3.3.3 Time-dependent Concentration Profiles of NDMA and Byproducts

Once the reaction pathways and reaction rate constants were determined, ordinary differential equations were generated for all species and solved to obtain the concentration profiles of all species. Figures 3.3 through 3.6 compare the time-

dependent concentration profiles of NDMA and the transformation products at pH 3 and pH 7, respectively. For the pH 3 runs, shown in Figures 3.3 and 3.4, the model was able to predict trends and magnitude of the experimentally measured byproducts, with the exception of formic acid. The pH was also observed to remain constant throughout the run. In contrast, at pH 7, the model predicted linear formation of dimethylamine (DMA) and methylamine (MA) and overall under predicted to the concentrations of all byproduct. Concentration profiles are shown in Figures 3.5 and 3.6. It is important to note that the pH dropped significantly in the model (from a starting pH of 7 to around 4) whereas the experimental results from Lee et al 2005 did not observe a notable change in pH as they had added a phosphate buffer [23]. We are now currently examining the cause of this discrepancy by investigating the influence of pH change during the simulation and determining the best way to incorporate a buffer while allowing for the pH to vary throughout the simulation.

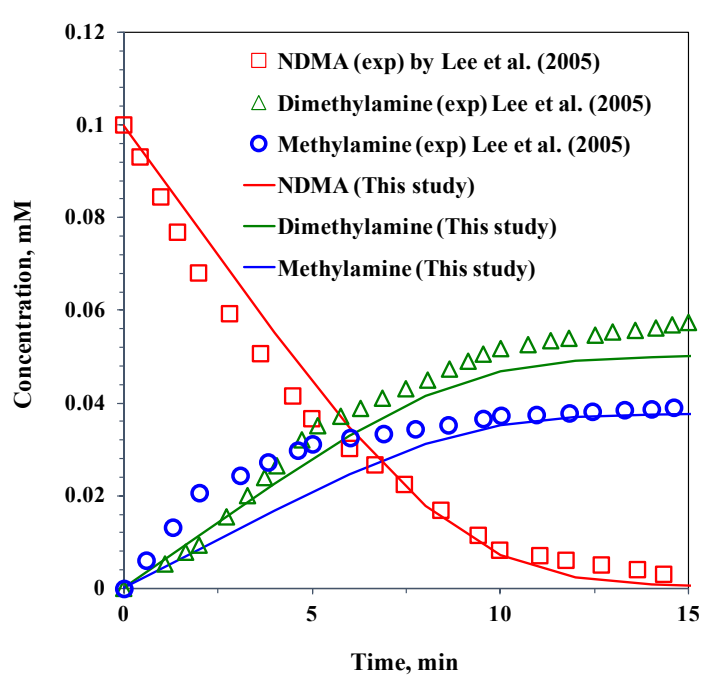


Figure 3.3 Concentration profile of major byproducts of NDMA decay at pH 3 for model in comparison to experimental results from Lee et al. 2005 [23]

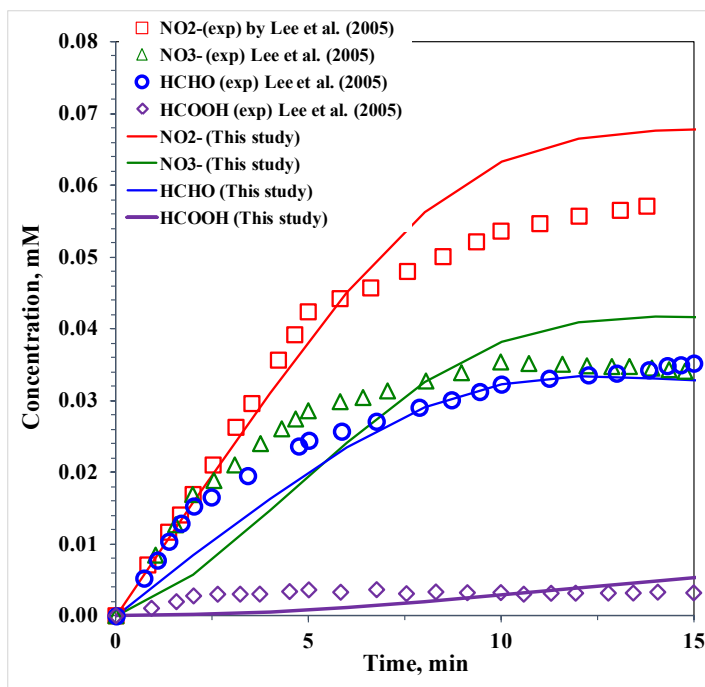


Figure 3.4 Concentration profile of minor byproducts of NDMA decay at pH 3 for model in comparison to experimental results from Lee et al. 2005 [23]

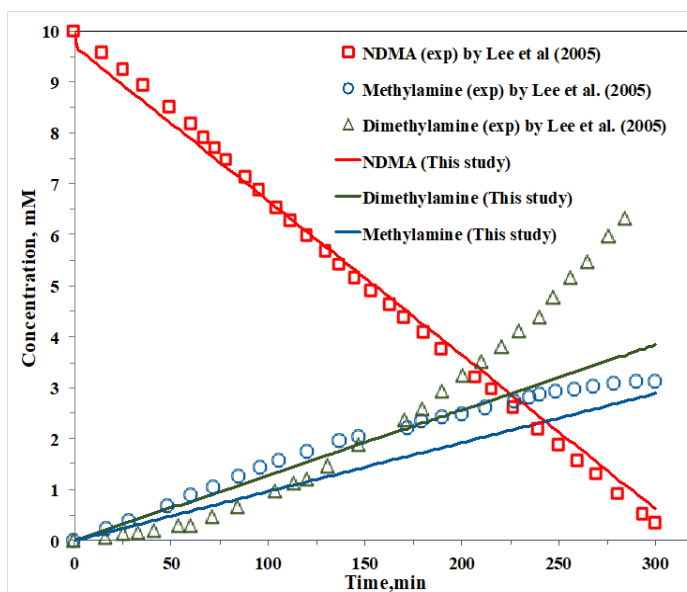


Figure 3.5 Concentration profile of major byproducts of NDMA decay at pH 7 for model in comparison to experimental results from Lee et al. 2005 [23]

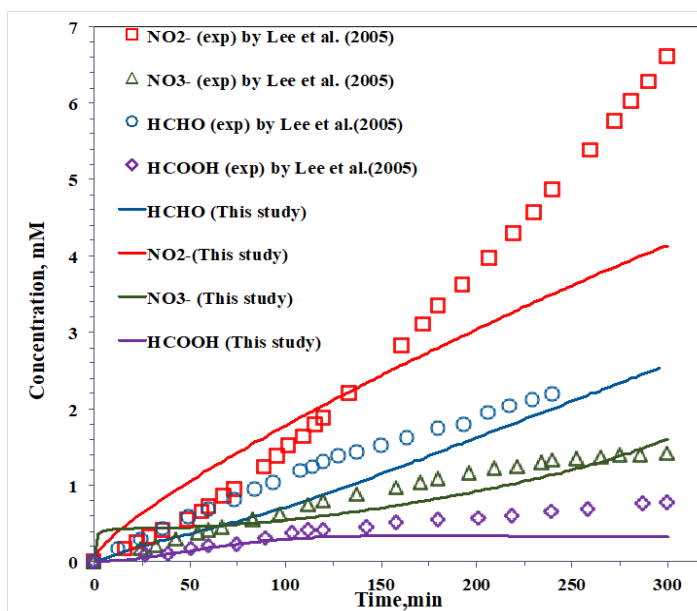


Figure 3.6 Concentration profile of minor byproducts of NDMA decay at pH 7 for model in comparison to experimental results from Lee et al. 2005 [23]

3.3.4 Sensitivity Analysis

A sensitivity analysis was performed to investigate the impact of quantum yields and rate constants on the predicted concentration profiles of species. By doing so, one can get to know the dominant important reactions and species that are responsible for the important byproducts. These impacts were examined by observing the decay of NDMA and the production of the primary byproducts, DMA and MA. NDMA decay and DMA formation only occur through photolysis reactions and therefore only changes in quantum yield values were investigated. The production of MA occurs through the reaction with a product of NDMA photolysis. For the sensitivity analysis for MA, both quantum yield values and the involved rate constant were altered. The quantum yield values were altered by the difference of a factor of two and reaction rate constants were altered by the difference of a factor of ten for MA analysis. The specific photolysis reactions are shown in Table 3.4 and the reaction rate constant ($k = 10 \text{ s}^{-1}$) for $\text{CH}_3\text{N}^+\text{H}=\text{CH}_2 \rightarrow \text{CH}_3\text{NH}_2 + \cdot\text{CH}_2\text{OH}$ were the values varied to obtain the figures below. It is important to note that reaction 7 has a quantum yield of zero at pH 3 and therefore was not varied and is not shown in the figures.

Table 3.4 Reactions and corresponding quantum yield values varied for sensitivity analysis. Note that their reaction numbers correspond to the quantum yields changed as seen in the key for Figures 3.7 through 3.18

Number	Reaction	Φ at pH 3	Φ at pH 7
1	$(\text{CH}_3)_2\text{N-NO} \rightarrow (\text{CH}_3)_2\text{N}^+\text{H}$	0.051	0.15
2	$(\text{CH}_3)_2\text{N-NO} \rightarrow \cdot\text{NO}$	0.001	0.001
3	$(\text{CH}_3)_2\text{N-NO} \rightarrow \text{O}_2\cdot^-$	0.14	0.15
4	$(\text{CH}_3)_2\text{N-NO} \rightarrow \text{CH}_3\text{N}^+\text{H=CH}_2$	0.27	0.6
5	$(\text{CH}_3)_2\text{N-NO} \rightarrow (\text{CH}_3)_2\text{NH}_2^+$	0.18	0.4
6	$(\text{CH}_3)_2\text{N-NO} \rightarrow \text{HNO}_2$	0.102	0.27
7	$(\text{CH}_3)_2\text{N-NO} \rightarrow \cdot\text{NO}$	0	0.046

Figures 3.7 and 3.8 indicate the decay of NDMA as predicated by the model at pH 3. The variation of individual quantum yields suggests that reaction 6 [i.e., $(\text{CH}_3)_2\text{N-NO} \rightarrow \text{HNO}_2$] is primarily controlling the concentration of NDMA in the system as changes in all other rate constants produce results identical to the original model output. Similarly at pH 7, shown in Figures 3.9 and 3.10, reaction 6 is the only one that significantly alters the concentration profile. All other reactions resulted in identical results to the original quantum yield input.

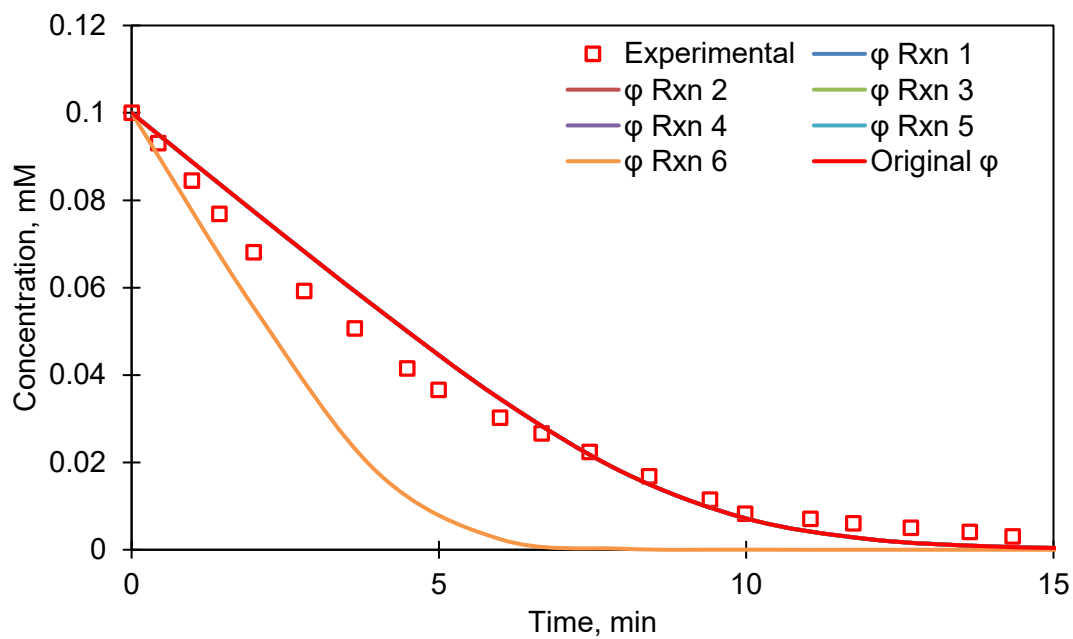


Figure 3.7 NDMA concentration profile at pH 3 for variation of quantum yield two times the originally reported value

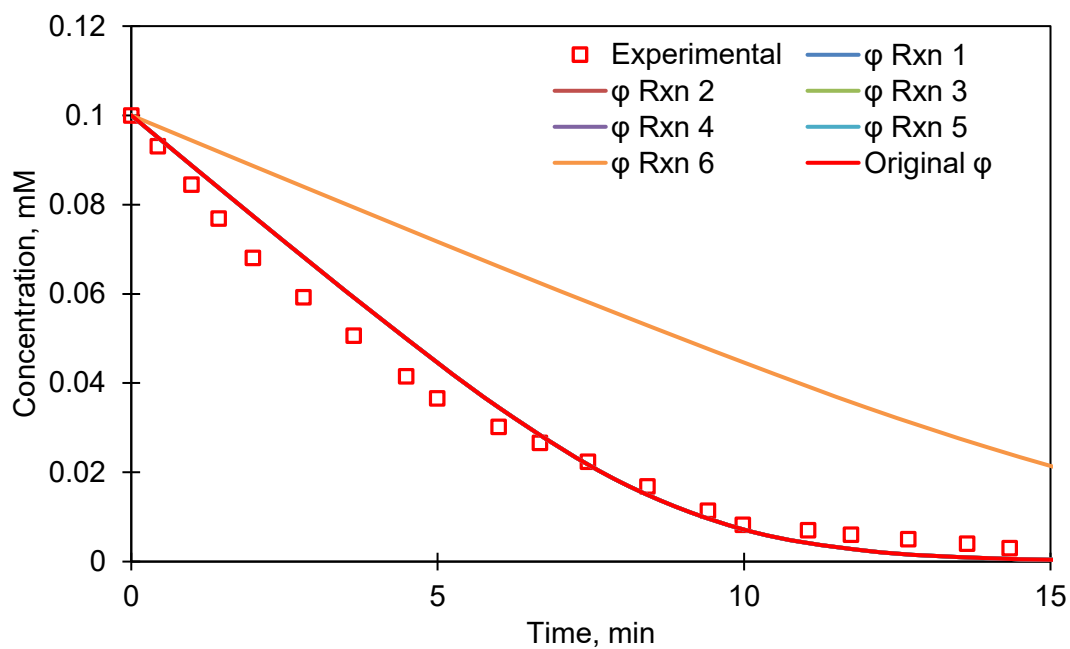


Figure 3.8 NDMA concentration profile at pH 3 for variation of quantum yield half of the originally reported value

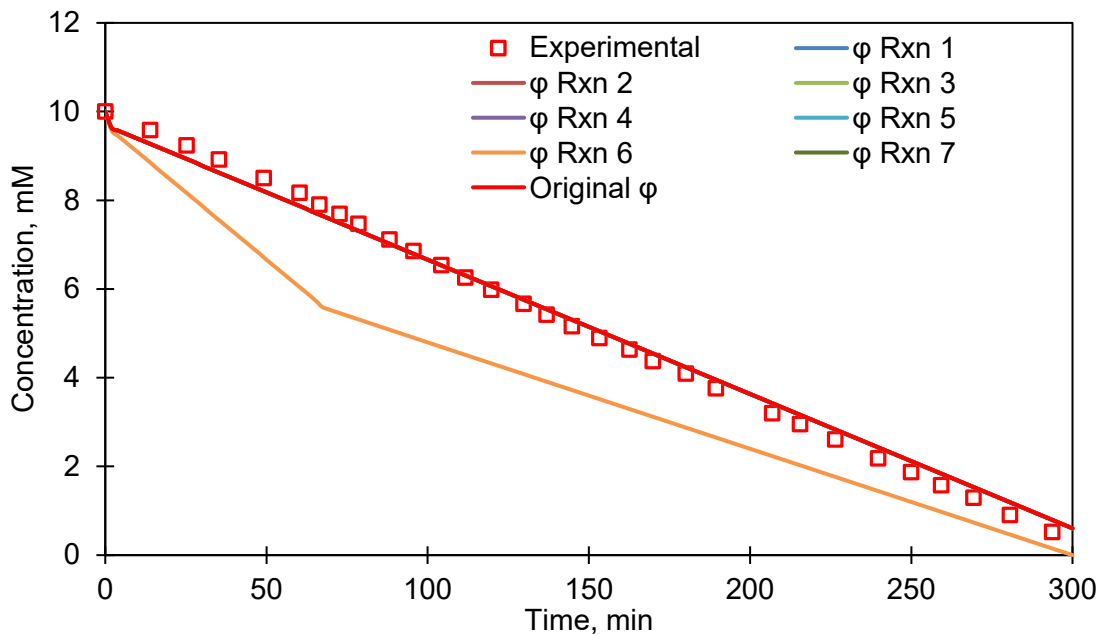


Figure 3.9 NDMA concentration profile at pH 7 for variation of quantum yield two times the originally reported value

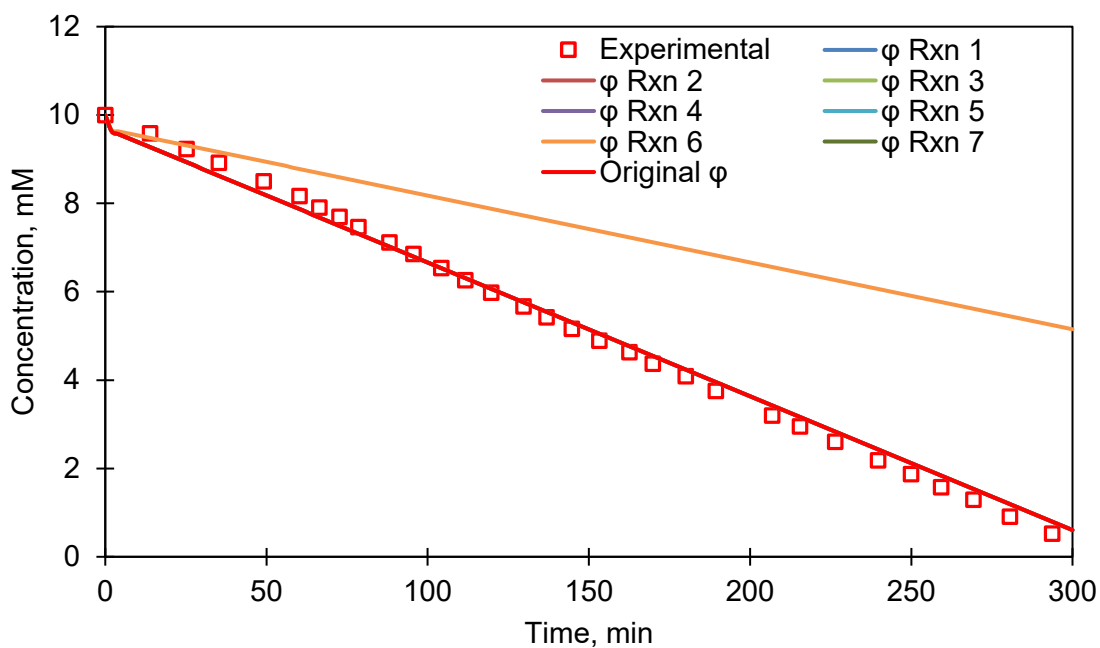


Figure 3.10 NDMA concentration profile at pH 7 for variation of quantum yield half of the originally reported value

The formation of DMA is impacted by reaction 6 as well since the concentration of NDMA in the system impact DMA formation, the quicker NDMA is exhausted, less is

available for DMA formation, shown in Figure 3.11 for pH 3. At pH 7, reaction 6 did not produce more DMA than originally modeled results since a linear increase in DMA was already predicted and no more DMA could be formed from the available NDMA. DMA formation is also impacted by reaction 5 ($(\text{CH}_3)_2\text{N-NO} \rightarrow (\text{CH}_3)_2\text{NH}_2^+$) as expected since this is the reaction responsible for its formation. This was shown for pH in Figures 3.11 and 3.12 and in Figures 3.13 and 3.14 for pH 7. All other reactions resulted in identical results to the original quantum yield input.

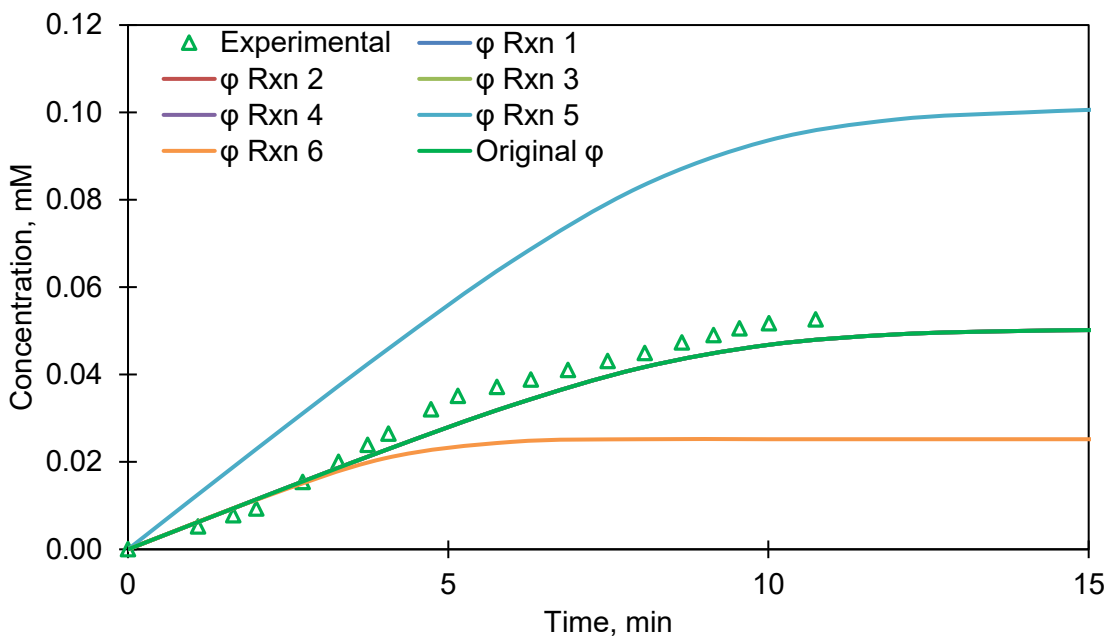


Figure 3.11 DMA concentration profile at pH 3 for variation of quantum yield two times the originally reported value

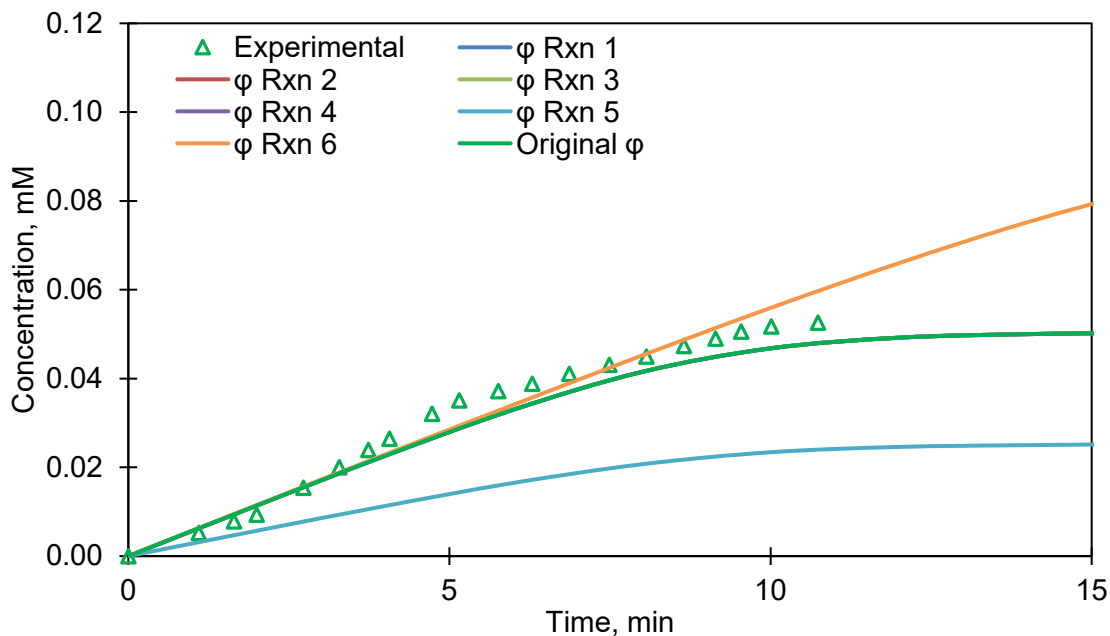


Figure 3.12 DMA concentration profile at pH 3 for variation of quantum yield half the originally reported value

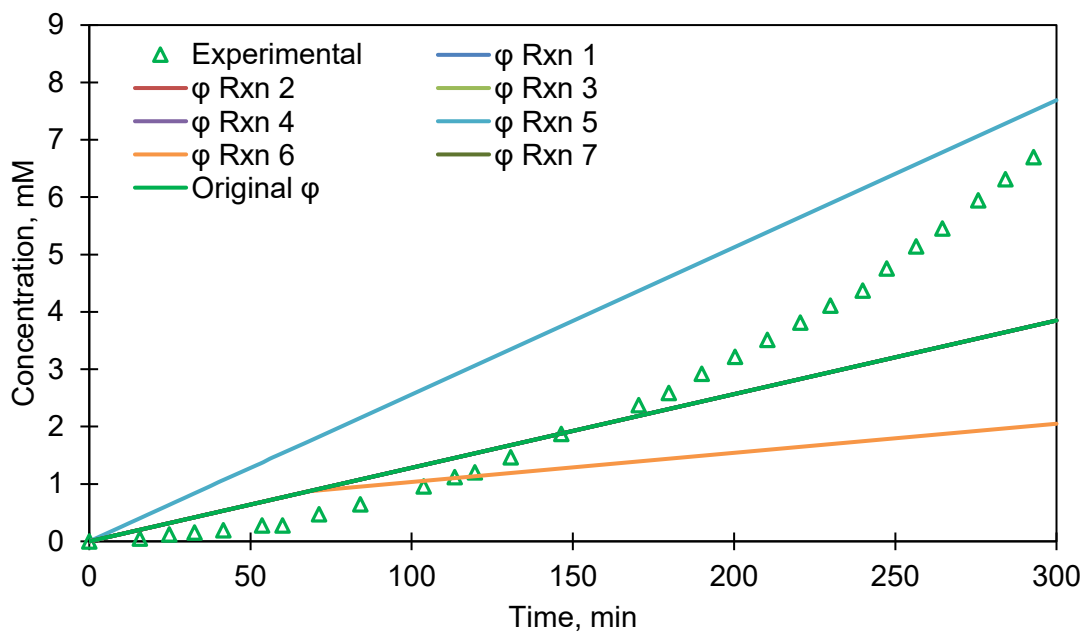


Figure 3.13 DMA concentration profile at pH 7 for variation of quantum yield two times the originally reported value

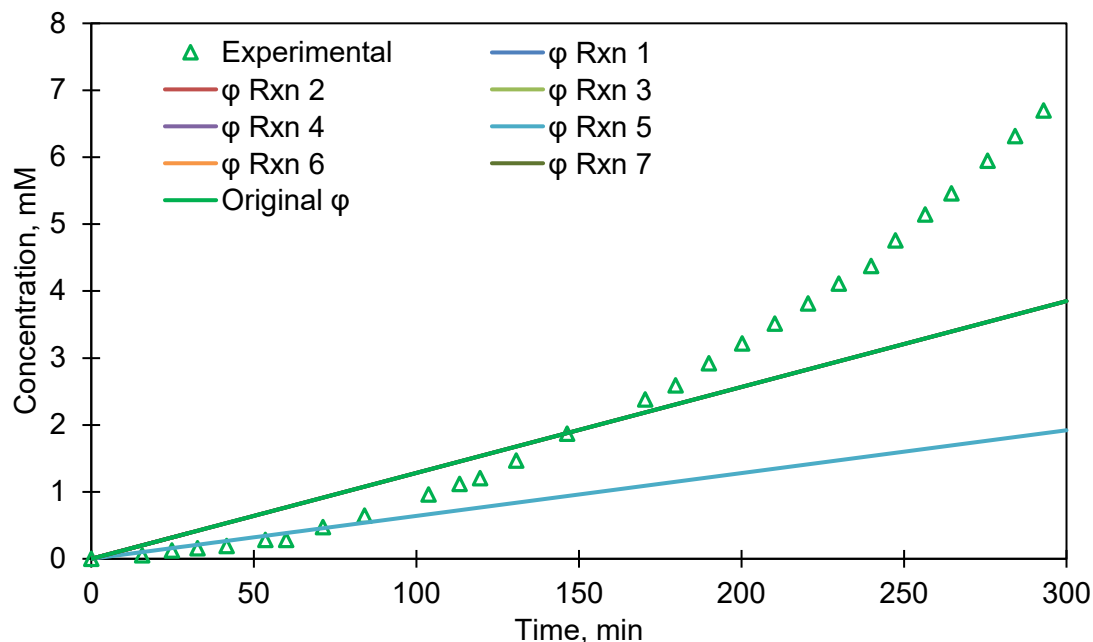


Figure 3.14 DMA concentration profile at pH 7 for variation of quantum yield half the originally reported value

Quantum yield was not the only factor impacting MA formation, an irreversible reaction is responsible for the direct formation and therefore the reaction rate constant was also varied. Similar to DMA, MA formation is dependent on reaction 6 which impacts the concentration of NDMA in the system and behaves in a similar manner to DMA at both pH 3 and pH 7, Figure 3.15 through 3.18. Reaction 4 ($(\text{CH}_3)_2\text{N-NO} \rightarrow \text{CH}_3\text{N}^+\text{H}=\text{CH}_2$) impacted MA formation the most as it produces the reactant needed for the irreversible reaction for MA production. However, changes in the rate constant for $\text{CH}_3\text{N}^+\text{H}=\text{CH}_2 \rightarrow \text{CH}_3\text{NH}_2 + \cdot\text{CH}_2\text{OH}$ did not significantly impact MA concentration profiles. At pH 7, when the quantum yield for reaction 7 ($(\text{CH}_3)_2\text{N-NO} \rightarrow \cdot\text{NO}$) was decreased, no MA was formed. All other reactions resulted in identical results to the original quantum yield input.

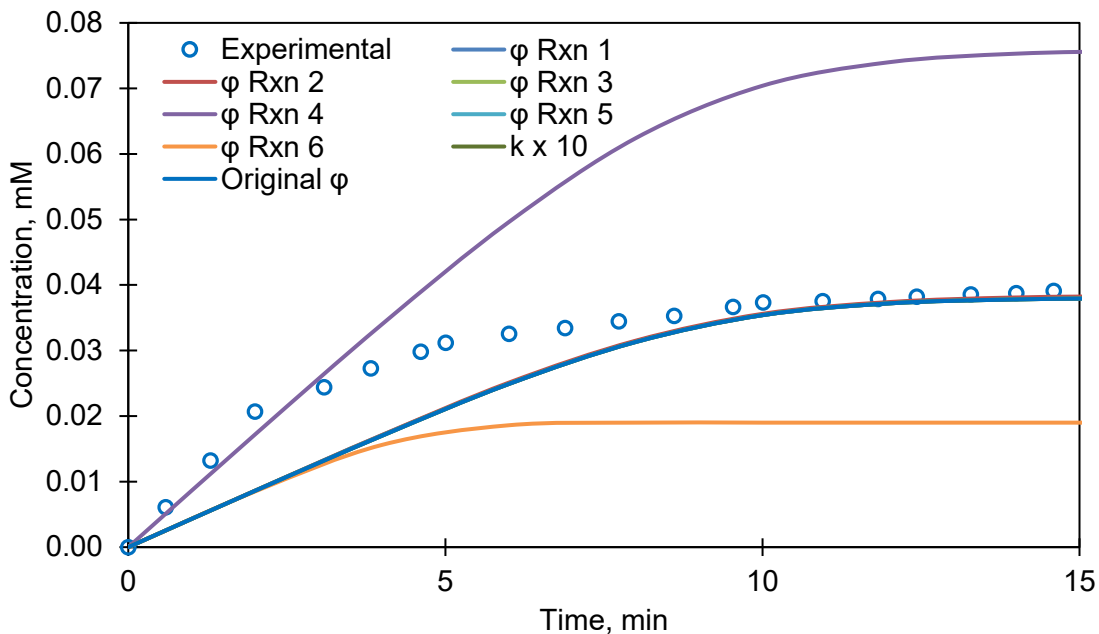


Figure 3.15 MA concentration profile at pH 3 for variation of quantum yield two times the originally reported value and rate constant by ten times the originally reported value

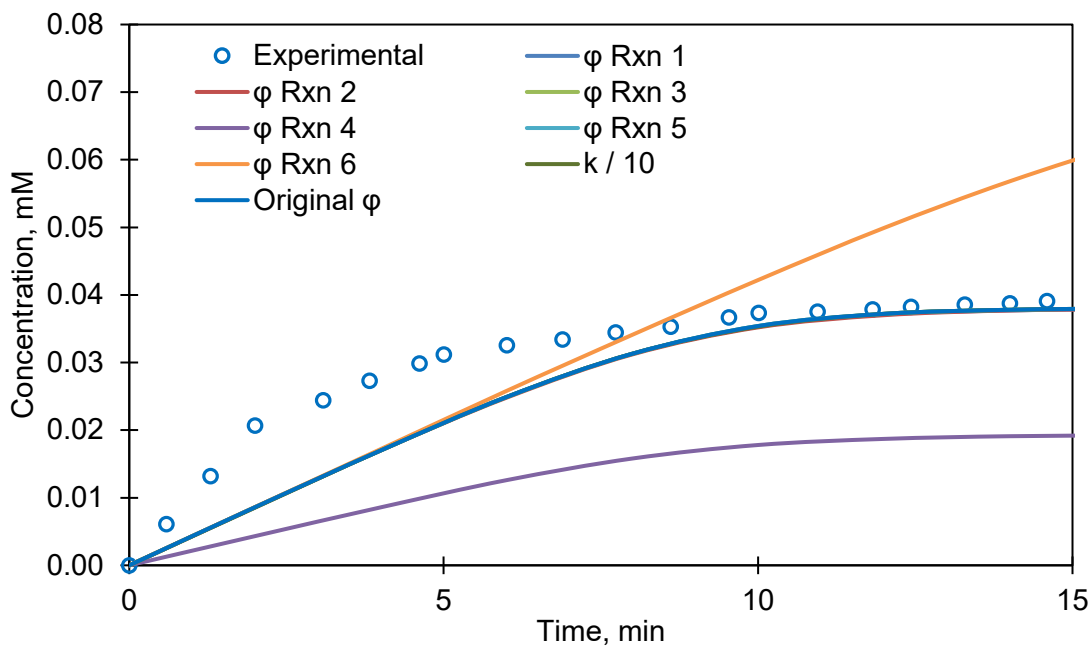


Figure 3.16 MA concentration profile at pH 3 for variation of quantum yield half the originally reported value and rate constant by one tenth the originally reported value

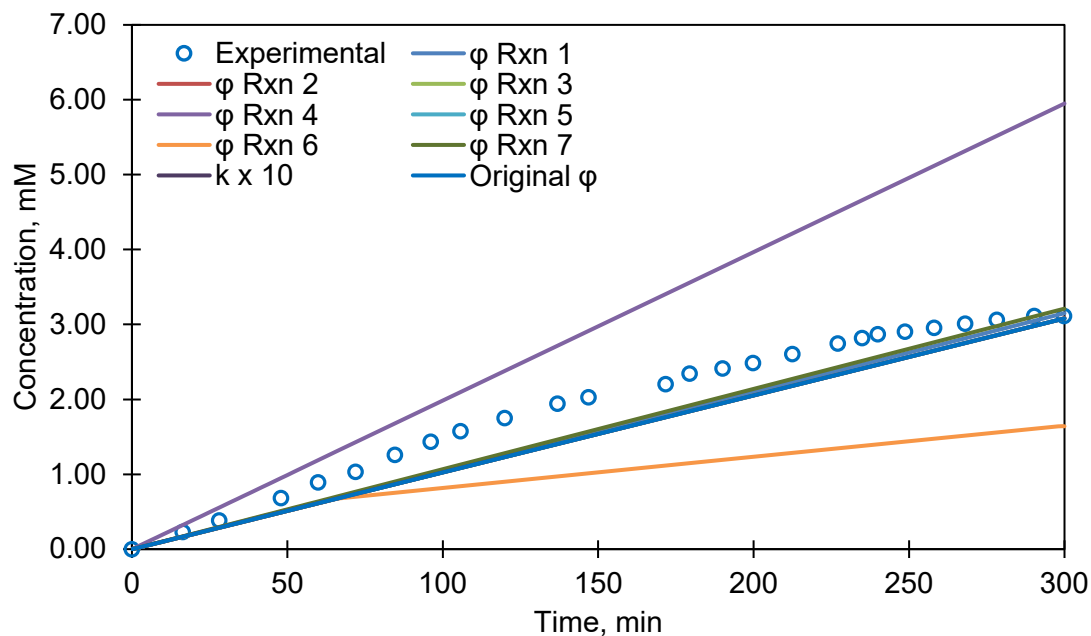


Figure 3.17 MA concentration profile at pH 7 for variation of quantum yield two times the originally reported value and rate constant by ten times the originally reported value

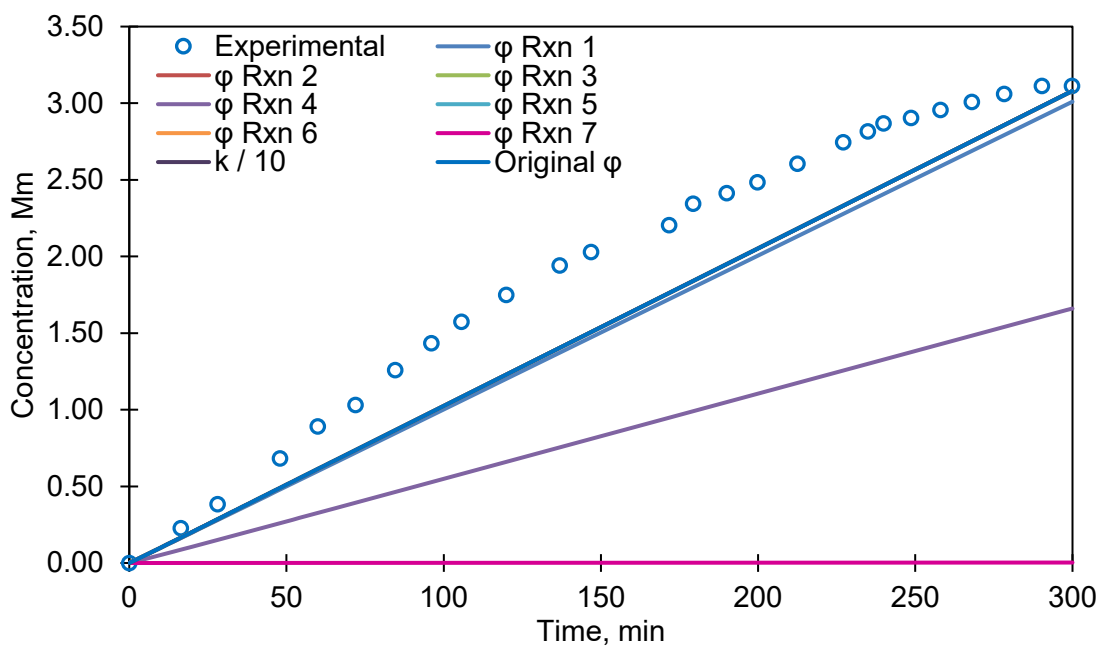


Figure 3.18 MA concentration profile at pH 7 for variation of quantum yield half the originally reported value and rate constant by one tenth the originally reported value

3.4 Environmental Implications

Nitrogen-containing organic contaminants pose more toxicity than carbon-containing compounds. This raises serious concern about the fate of degradation products in engineered water treatment and natural aquatic systems. The findings in this study highlight the importance of elementary reaction-based kinetic models that provided mechanistic insight into the reaction mechanisms and kinetics of nitrogen-containing organic contaminants. This is key if this model is to be applied in other scenarios. With knowing the reactions that occur, steps can be taken to predict the stable byproducts based on input compounds and concentrations. When applied in a water treatments setting, the impact of dissolved organic matter (DOM) and other common water constituents needs to be considered as well. Further work needs to be done on this topic as it will likely alter the pathways and products observed when treating for nitrosamine compounds.

4 Development of an Agent-based Model to Predict the Fate of Organic Compound Degradation in Aqueous Phase Advanced Oxidation Processes³

4.1 Introduction

A number of concerns have been raised about the potential adverse health and ecological effects of new and emerging contaminants recently identified in natural waterways that are likely present due to inability of conventional water and wastewater treatment processes [1, 86, 87]. This has led to a call to eliminate such contaminants at treatment facilities, to the greatest extent possible, to prevent their entrance into natural water systems where they can ultimately harm human or ecological health in often highly complex ways.

Advanced Oxidation Processes (AOPs) offer a promising and attractive technological solution to this problem because they can destroy a wide variety of known and emerging organic contaminants present in the aqueous phase as hydroxyl radicals (HO^{\bullet}) produced at ambient temperature and atmospheric pressure react rapidly with the electron rich sites of organic contaminants causing degradation via a series of chain-reactions [12, 13]. If adequately designed, AOPs can transform target organic contaminant(s) into various intermediate radicals and byproducts that can eventually be mineralized into inert substances, such as water, carbon dioxide and mineral acids.

AOPs offer an innovative way to degrade hazardous trace organic contaminants but their complex radical-involved reaction mechanisms make it difficult to understand and predict the formation of intermediate radicals and byproducts, which is problematic for determining when certain byproducts are expected to be more toxic than their parent contaminants. This process is complicated by the fact that complex peroxy radical-involved reactions form identical products via multi-channel/-step reactions, making it difficult or challenging to experimentally identify each elementary reaction pathway and measure accompanying reaction rate constants. Given the hundreds of thousands of chemicals in commercial use and production today, a model that can predict the

³ The material contained in this chapter is in preparation for submission to a journal

formation of intermediate radicals and byproducts without the need for nearly endless experimentation is critical to the success of the AOP treatment approach. Such a model could greatly aid the preliminary design of AOPs prior to full-scale development and guide industry's assessment of environmentally recalcitrant toxic chemicals in their manufacturing processes.

A number of conventional steady-state and non-steady-state models have already been developed in the literature that explore various aspects of AOP treatment. For example, Glaze *et al.* (1995) derived a kinetic model for the UV/H₂O₂ process with steady-state approximation to predict final concentrations of 1,2-dibromo-3-chloropropane (DBCP) [88]. This work set the formation rate of HO• equal to zero to determine the pseudo-steady-state concentration of HO•, invoking the pseudo-state-assumption that the formation and consumption rates of HO• are equal based on the idea that reaction rates involving HO• are very fast while HO• concentration are very small relative to other compounds. Pseudo-steady-state concentrations were solved at each time step (t=1) up to 1440 seconds of reaction time and then compared with experimental observations for the target compound DBCP. It was found that the degradation of DBCP follows pseudo-first-order kinetics irrespective of the experimental conditions used (i.e., pH and the concentrations of H₂O₂, DOM, and alkalinity). Sharpless and Linden (2003) also used the steady-state approximation to estimate both the time-based and fluence-based rate constants for NDMA degradation resulting from both the photolysis and HO•-induced reactions, respectively, with low and medium pressure UV lamps [50]. Their calculated rate constants were also found to be consistent with experimental observations. Wols and Hofman-Caris (2012) derived a similar model by including the photolysis of target compounds and then they calculated the estimated removal efficiencies from both photolysis and the HO•-induced reactions for more than 100 emerging contaminants with low pressure UV lamps (400 mJ cm⁻²) for a typical Nieuwegein water: 250 mg/L HCO₃⁻, 1.7 mgC/L DOC, and pH 8) [89]. They also performed a cluster analysis and classified those compounds based on $k_{HO\bullet}$, quantum yields and molar absorptivity. Finally, Guo *et al.* (2013) developed UV/H₂O₂ process models with steady-state approximation for various flow types of reactors such as completely mixed batch reactors (CMBR), completely mixed flow reactors (CMFR), plug flow reactors (PFR), tank-in-series reactors (TIS, i.e., sequential CMFRs), and real reactors with a disperse flow model

(DFM) [61, 90]. These MathCAD models were able to calculate the steady-state concentration of HO[•], the removal efficiency of a target compound, and the energy efficiency per removal of order, given any specified target compound and other water quality parameters.

The most detailed level of modeling to date in the existing literature are models that use complete kinetic descriptions of a system without steady state approximations [91]. In other words, all reactions in the system are considered and rate equations are written for all species. In such models, reactions occur at the sub-microsecond timescale while typical UV/H₂O₂ processes take place on the order of minutes. The integration of the resulting set of stiff differential equations from these models may require up to 10⁸ - 10¹² steps depending on the number of ordinary differential equations (ODEs) assigned (Payton, 1990). One example of such a model is that of Yao *et al.* (1992) who used the ACUCHEM software to develop a UV/H₂O₂ kinetic model [92, 93]. The drawback of using ACHUCHEM is that the software does not consider the acid-base equilibrium and variable photolysis rates nor does it consider complex flow reactor kinetics. This is problematic because it has been shown that the pH of a solution can drop as organic compounds are oxidized into mineral acids, carbon dioxide or acidic intermediates during the UV/H₂O₂ process and, therefore, it is critical to simulate such pH changes [62]. In response, Crittenden *et al.* (1999) developed a dynamic kinetic model of the UV/H₂O₂ process in a CMBR with non-steady-state approximation that includes known elementary chemical and photochemical reactions and literature-reported photochemical parameters with chemical reaction rate constants. By default, the target organic compound(s) of this model reacts with HO[•], carbonate radicals (i.e., •CO₃⁻), phosphorus radicals (i.e., •HPO₄⁻), •O₂⁻ and •HO₂ radicals while including scavenging reactions of HO[•] with alkalinity, phosphorus buffers, and carbonate radicals. The scavenging reaction by NOM was not included in Crittenden *et al.* (1999) but the final product software (see below) does include this reaction. The model also tracks the net charge balance of anions and cations to account for changes in solution pH over time. Finally, the model solves a set of very stiff ODEs for all identified species using a backward differentiation formula method by adapting a package designed by Hindmarsh (1974), making it possible to solve the model in several minutes using a microcomputer [58, 94]. The resulting kinetic model was then validated with experimental studies by Lay (1989) and

the results of Glaze *et al.*'s (1995) pseudo-steady-state model [88, 95]. This comprehensive kinetic model is now available as AdOx™ software (Li *et al.*, 1998) that enables users to select reactor types (e.g., CMBR, CMFR, TIS) based on flow conditions as well as the types of UV lamps used (low pressure or medium pressure lamp) [88, 96]. The software also implements the analysis function of tracer study that makes it possible to estimate the removal efficiency of target compounds using the DFM model in a real reactor. For example, Li *et al.* (2008) used AdOx™ to evaluate the efficiency of a full-scale UV/H₂O₂ process for the removal of methyl *tert*-butyl ether (MtBE) and tertiary butyl alcohol (*t*BA) from a drinking water source [60]. Evaluations included two commercial UV light sources such as low pressure high intensity lamps (LPUV) and medium pressure high intensity lamps (MPUV), pretreatment options including ion exchange softening with seawater regeneration, pellet softening, weak acid ion exchange, and high pH lime softening followed by reverse osmosis. A dealkalization option was also evaluated prior to the UV/H₂O₂ process. Based on the requirement of the treatment objective, the electrical energy per order values, and H₂O₂ residual concentration after the process, Li *et al.* (2008) optimized the dose of H₂O₂ at the required number of reactors per treatment train for both LPUV and MPUV lamps [60]. Finally, Crittenden *et al.* (2012) compared the *pseudo*-first-order rate constants of DBCP predicted from the Sim-pSS model, pseudo-steady-state model, and AdOx kinetic model with those determined by Glaze *et al.* (1995) under various experimental conditions and found that the AdOx kinetic model better simulated all experimental conditions than the other two models [88, 97]. The authors concluded that AdOx was better able to predict micropollutant kinetics than *pseudo*-steady state models because of its ability to model containment destruction under conditions in which initial experimental parameters such as pH and H₂O₂ concentration (thus, HO• concentration) change as treatment progresses.

Wols *et al.* (2014) also developed a kinetic model for UV and UV/H₂O₂ process in a collimated beam system employing a monochromatic low pressure UV lamp and later developed a similar kinetic model for polychromatic medium-pressure UV lamps [98]. These kinetic models included photolysis of nitrate and subsequent reactions of nitrogen-radicals (e.g., •NO and •NO₂) to predict the water quality impacts of the UV and UV/H₂O₂ process on treated wastewater. Wols *et al.* (2014, 2015) assigned rate

constants for both forward and backward reactions to account for equilibrium reactions and avoided the use of steady-state approximation to account for the impact of changes in solution pH [98, 99]. Their model was validated with their own experiments for the degradation of 36 pharmaceuticals in the presence of bicarbonate, nitrate, and NOM while it was found that the model inconsistently predicted the degradation for 5 compounds when compared to experimental observations due to pH effects during photolysis and the radical scavenging of NOM. These two kinetic models were later combined with a computational fluid dynamics (CFD) model to predict the degradation of a group of 35 pharmaceuticals in a pilot-scale UV/H₂O₂ reactor [98].

In general, the main limitation of the AOP models in the existing literature reviewed so far is that they rely on ODEs that are very stiff to solve numerically because of dramatic differences in reaction rates (i.e., the product of the reaction rate constant and the concentration) that often vary by more than 10 orders of magnitude in an AOP (i.e., 10 M⁻¹s⁻¹ v.s. 10¹⁰ M⁻¹s⁻¹). Such models also frequently produce unstable numerical solutions as a consequence of the lumped elementary reactions that often occur in an AOP. It is for these reasons that our research explored the possibility of using Agent-based modeling (ABM) to simulate the complex reactions and resulting byproducts and byproduct chains produced in an AOP to predict the fate of organic compounds in this promising approach to water and wastewater treatment. ABM is a computer simulation technique that models the actions of software “agents,” representing any conceivable entity such as a person or a chemical species, interacting with other agents and the environment in which they are embedded at the level of the individual agent to produce or reproduce complex emergent patterns at the system level. The use of individual-level modeling to produce system-level dynamics means that no generalized systems of equations are required to generate observed model results, making it possible to simulate a wide range of mathematically intractable systems [100]. The modular and extensible framework of an ABM, which relies heavily on the broadly applicable software design principles of Object-Oriented Programming, also allows for the abstraction of as much detail as necessary in order to reproduce complex emergent patterns in a manner that is similar to the experimental approach in that *ceteris paribus* conditions can be explored incrementally through the controlled manipulation of simulated modeling parameters assumed to be responsible for system-level patterns [101]. These features

make it possible for an ABM to overcome the restrictions of the ODE-based models outlined above, which are unable to adequately model competing radical induced multiple-elementary reactions that simultaneously produce different byproducts and, therefore, offer a promising solution to the advancement of AOP modeling over existing techniques. ABMs have already been employed in a wide range of fields, from the Social Sciences and Economics to Ecology and Biology, to explore numerous complex emergent phenomena that stem from the interactions of individual actors [102]. Agent-based modeling has also recently been applied to a variety of biological systems to gain mechanistic insights at the cellular level (e.g., insect communities and epithelial tissue) but our research is the first to use this modeling technique in the field of chemistry to explore the fate of organic compounds in AOP [103-105].

In our study, we develop an ABM to aid our understanding of the intermediate radicals and stable byproducts involved in peroxy radical bimolecular decay. Our model made it possible to visualize changes in chemical concentrations over time resulting from the complex reactions of chemical species interacting over time and space in a simulated AOP reactor, as parent chemical species react to produce byproducts and successive chains of byproduct reactions throughout a simulation run. This work enables researchers and AOP engineers to identify tipping points that could drive changes in concentration profiles over time as well as to predict the fate of organic species upon exhaustion of potential reactants. Finally, our model provides researchers a level of experimental control that is comparable to laboratory conditions in that researchers can manipulate individual or multiple experimental conditions to determine how such changes alter system dynamics (changes in concentration profiles over time) or the resulting fate of organic compounds. In this sense, researchers can run any number of relatively “cost-free” simulated experiments to pilot the plausibility of alternative hypotheses or to identify opportunities for future laboratory experiments that may prove useful for improving AOP wastewater treatments.

4.2 Materials and Methods

4.2.1 Model Overview

ChemSim is an ABM software application designed to predict the fate of organic compounds in Advanced Oxidation Processes (AOPs) for wastewater treatment, which is also capable of exploring other more generalized chemical reaction pathways. The agents of ChemSim represent thousands of individual molecules that each move through a simulated AOP reactor space containing an aqueous solution and react with other molecule agents representing different chemical species to produce terminal byproducts or byproduct chains over time based upon user-provided chemical reaction pathways. At the end of each simulated experiment, ChemSim produces a concentration profile time-series plot of all active and remaining chemical species for every simulated round as a way visualize changes in byproduct concentrations over time so as to predict the chemical fate of persistent organic compounds in AOP wastewater treatment. ChemSim was developed using the Java programming language and the MASON simulation library [106]. The remainder of this section uses the ABM standard ODD (Overview, Design concepts, Details) protocol to provide a formal model description of ChemSim [107, 108].

4.2.2 Entities, State Variables, and Scales

Molecule agents are the primary simulated entities of ChemSim. Molecule agents can represent any possible individual chemical species or compound. Each molecule agent has four main attributes that determine how it behaves within the simulated AOP reactor during a model run: 1) its species type (i.e., the chemical formula assigned to this species), 2) its current reactor location, 3) its reaction radius, and 4) a list of the species types of all possible reactants (i.e., the other simulated molecule agents of a species type to which this species can chemically react). The only additional entity modeled in ChemSim is a disproportionation reaction agent whose role is to temporarily represent the existence of chemicals undergoing a disproportionation reaction over time, which requires multiple simulation rounds to complete as opposed to the single-round reaction time of all other simulated byproducts.

The environment in which our molecule agents interact in ChemSim is a simulated AOP reactor consisting of a well-mixed aqueous solution with dissolved compounds (e.g., Oxygen, Nitrogen, etc.). We use a sparse lattice to model this environment computationally, which tracks the location of all molecule agents in discrete three-dimensional space over time. The sparse lattice design is organized around three hashmap data structures: 1) a space-integer lattice, 2) an agent map, and 3) a tag map. These three hashmaps use the fastutil implementation to take advantage of the fact that it is possible to determine hashmap sizes at runtime in order to optimize computational performance. The location a molecule agent occupies in our sparse-integer map is hashed according to the scheme by Teschner et al. (2003) [109]:

$$\text{hash}(x, y, z) = ((x * p1) \text{ xor } (y * p2) \text{ xor } (z * p3)) \text{ mod } n$$

where $x, y, z \in \mathbb{Z}$, $p1, p2, p3 \in PRIME$, and n is the size of the allocated array for the values. This hashing allows us to collapse three-dimensional space into a single map (i.e., list) of values and enables agent retrieval and probing for agent existence at a given location in constant time. The tag hashmap is used when the size of the search space exceeds the number of agents in the system at which point it is more computationally efficient to linearly bound the search space (i.e., $O(n)$) by the number of agents with the same tag type (a simple hash of the molecule's chemical species formula) and to use the Euclidian distance from the target agent to determine a match when said distance is less than the requested radius. Finally, our sparse grid is designed and indexed to allow for efficient insertion, search, and retrieval of agents from the data structure, which is critical for computational performance given that ChemSim must constantly update agent locations in space to model dispersion, add new byproduct agents, and remove parent reactant agents.

4.2.3 Data Requirements

ChemSim requires a number of user-provided data inputs to initialize the model for each simulated experiment. For example, users must provide a comma-separated values (CSV) file that lists the names of the chemical species to be included and their chemical formulas. Users must also provide a second CSV file that identifies the known set of chemical reaction pathways so that the model can determine which species should

interact with which other species in the simulated reactor and how (based on reaction types and reaction rates). Users must then specify the initial concentration of species so that the model can calculate the number of agents to create per mol of a given compound upon model initialization. Users must also specify the probability (on a scale of 0 to 1) of a photolysis reaction with Hydrogen Peroxide, which is used to catalyze all further chemical reactions in our simulated AOP reactor (more on this below). Finally, users are asked to set the stopping condition for the given simulated run (e.g., exhaustion of a target chemical species or a user-specified time step) or the model will run until the user manually stops the simulation.

4.2.4 Model Initialization

To begin model initialization, ChemSim first reads in the user-provided CSV files outlined above. One molecule agent is then created for each chemical compound based upon the initial concentration of compounds and species types defined in these user-provided CSV files. Each molecule agent is also added to the sparse reactor grid and accompanying hashmaps at a random location based upon a draw from a uniform distribution as a way to replicate the laboratory conditions of a well-mixed chemical solution at t_0 . A bulk loader is used to determine the quantity of agents to create for each chemical compound scaled to the molar parameters provided for that compound and using the following statistical normalization technique:

$$normalizer = 1/(v_1 + v_2 + \dots + v_n)$$

$$molecules_i = v_i * normalizer * target$$

$$scalar = normalizer * target$$

where v is the number of moles for a given compound, *target* is the maximum number of total molecules, and *molecules* is the quantity of the given molecule.

4.2.5 Process Overview and Scheduling

A typical simulated experiment involves the following basic order of operations:

1. ChemSim first reads in the required user-provided CSV files and initializes the model to include molecule agents randomly located throughout the sparse grid of the simulated reactor for each chemical compound present at the start of the simulated experiment in the quantities required based upon the initial concentrations of each species.
2. During each simulated round, the scheduler randomly activates every individual molecule agent one-at-a-time to react with any available reactant in its reaction radius (see sub-model below) or moves about the sparse reactor grid using a random walk algorithm when a reactant is unavailable.
3. At the end of each simulated round, all existing pKa reactions are executed (see sub-model below), molecule counts are balanced, and the photolysis reaction rate is updated to ensure the linear decay of any existing Hydrogen Peroxide agents in the next round of the simulation.
4. The simulation will then repeat these steps until the user manually stops the simulation or the simulation reaches the user-specified stopping conditions. At this point, ChemSim tallies the final molecule count, which is converted to a molar value to determine the final concentration profile of all chemical species remaining at the end of the simulation.

A simulation round in ChemSim can represent an arbitrary length of time depending upon reaction requirements. During each round, all agents present in the model are scheduled for activation. They are then sequentially activated and operate in accordance with their step method. For basic chemical species, the agent first checks to see if it should move before checking to see if a reaction should occur. Movement takes place using a simple random walk where a normally distributed random number is drawn for each direction (i.e., x, y, and z) and the agent moves plus or minus one unit for a value within plus or minus one standard deviation respectively. Movement outside of the container is prevented. When reactions are checked, the model checks for bimolecular reactions, unimolecular reactions, and photolysis reactions. Reactions occur based upon the first chemical species within the correct interaction radius and either immediately generate new chemical species or a disproportionating species agent, based upon the appropriate equation. When disproportionating species are activated, they generate new chemical species that are appropriate for the time step. Once all species have been

generated, the agent removes itself from the model. Newly created agents are capable of interacting with other species the same time step they are created, but they will not be activated until the next simulation round. In the event a reaction contains a product that is not used in a subsequent reaction (i.e., “end product”) it is added to the total molecule count, but a corresponding agent is not created. At the end of the timestep, an updated photolysis decay rate and pKa reactions may be performed (see Sub-models).

4.2.6 Sub-models

4.2.6.1 Movement of the Molecule Agent

In the event that a molecule agent is activated and there are no reactant agents present in its interaction radius, the molecule agent will perform a simple random walk from its current location on the sparse reactor grid. To perform this random walk, a normally distributed random number is drawn for each possible movement direction (i.e., x, y, and z) and the agent will then move plus or minus one unit that is plus or minus one standard deviation of its current location for each possible movement direction respectively. The distance traveled each simulated round is scaled to 590 nm/s as per Pogson (2006), which ensures that the reactor remains a well-mixed solution for the duration of the simulated experiment [105]. Finally, movement beyond the sparse reactor grid is not allowed so the random walk of the agent is bounded by the extreme limits of the sparse grid dimensions, forcing the agent to remain within the reactor space itself.

4.2.6.2 Photolysis

Photolysis is required to catalyze all chemical reactions in our simulated reactor. Photolysis triggers the decay of existing hydrogen peroxide molecule agents into hydroxyl radical agents which then further catalyze reactions beginning with Acetone decay and then progressing through all possible byproducts chains in the user-provided known chemical pathways CSV file. To model photolysis reactions, we simply trigger the decay of a random Hydrogen Peroxide molecule agent each round of the simulation using a linear decay slope m described by the following equation:

$$c = m * t + b$$

where t is the current time-step or simulation round, b is the starting quantity of Hydrogen Peroxide molecules, and c is the new expected count based on a best fit linear decay as determined experimentally. The difference between c and the current quantity is the *decayCount* and can be used to calculate the individual odds that a Hydrogen Peroxide molecule agent will decay in a given round:

$$pr = \text{decayCount} / \text{quantity}$$

where pr is the individual probability, assuming all molecules have an equal likelihood of decaying.

4.2.6.3 Interaction Radius

Once photolysis triggers the decay of Hydrogen Peroxide agents into hydroxyl radical agents, all further chemical reactions use a reaction radius-based decay tied to the presence of possible chemical reactants. To determine if a reaction should occur when a given molecule agent is activated, ChemSim uses the interaction radius calculation described by Pogson et al (2006) to determine if a reactant is within the possible reaction range of a given activated molecule agent as follows [105]:

$$r = (3k\Delta t / 4 \times 10^3 N_a)^{1/3}$$

where k is the reaction rate, Δt is the duration of a model time step, and N_a is Avogadro's constant. However, within the context of the model the k_{chem} value is used as the basis,

$$k_{chem} = (k \times k_{diff}) / (k + k_{diff})$$

$$r = (3k_{chem}\Delta t / 4 \times 10^3 N_a)^{1/3}$$

Thus, if a reactant is found within r , new byproducts molecule agents are created (based on the user-provided chemical pathways list) and added to the sparse reactor grid at the location in which the reaction took place and the parent molecule agents are also removed.

4.2.6.4 Dissociation and Non-dissociation of Species

Another important aspect of the model is acid dissociation which takes place in the model through a process referred to in the code as “pKa balancing.” This takes place at the end of each time step for reactions that have a dissociation reaction defined.

Assuming reactions are defined as follows:



The quantity of agents in the model is calculated as follows:

$$ratio = 10^{-pKa} / 10^{-pH}$$

$$quantity_{A^-} = count_{A^-} * ratio$$

$$quantity_{A^-} = quantity_{A^-} > count_{A^-} \text{ then } count_{A^-} \text{ else } quantity_{A^-}$$

$$quantity_{H^+} = quantity_{A^-}$$

$$quantity_{HA} = count_{HA} - quantity_{A^-}$$

Assuming that pKa is the acid dissociation quantity that is relevant to the reaction and pH is the appropriate value for the solution. The quantities then represent the number of molecules that need to be removed, or added, to the model. In the event that molecules need to be removed, the first known instance is removed until the total quantity has been removed. In the event that molecules need to be added, they are introduced at a random location within the model. In either case, the inherent stochasticity allows us to assume a well-mixed solution.

4.2.7 Design Concepts

Agent decision-making in ChemSim, unlike most ABM simulations, is highly constrained and deterministic. This is because agents represent inanimate chemical compounds or molecules that simply respond to their environment without decision-making. The

advantage of this design pattern is that ChemSim agents are computationally lightweight, allowing large numbers of agents to be simulated relative to typical ABMs.

4.2.8 Emergence

The goal of most ABMs is the generation of emergent phenomenon. The dynamic concentration profiles of our chemical species that vary over time throughout the course of our simulations are one example of an emergent product in ChemSim. The final concentration profiles or the remaining chemical species is another important emergent outcome. It is this outcome that we can use to predict the fate of organic compounds in AOP wastewater treatment.

4.2.9 Interaction

The main drive of emergence and system complexity in ChemSim comes from agent interactions as opposed to agent decision-making. Thousands of individual-level interactions take place between heterogeneous agents representing various chemical species both across time and across space in every round of our simulated experiments. These interactions can be either bimolecular, taking place with the first appropriate species within the appropriate interaction radius of the agent, or disproportionate, taking place over multiple rounds producing multiple stages of byproducts.

4.2.10 Stochasticity

The initial location of all molecule agents on our sparse reactor grid are randomly assigned at model initialization to replicate a well-mixed solution. Molecule movement during each simulation round is also modeled using a random walk to replicate natural dispersion in an aqueous solution. Finally, photolysis reactions with Hydrogen Peroxide agents occur at a random rate to replicate linear decay at each round of the simulation. Such reactions are necessary to produce hydroxyl radical agents which further catalyze all other chemical reactions in the simulation. This means that the location of each photolysis reaction is determined based on a random draw to match the linear decay probability for that round and the location of that reaction is based on the location of the randomly selected available Hydrogen Peroxide agent chosen in that round for that

particular reaction. In sum, stochasticity drives many of the complex dynamics underpinning the results of ChemSim at the level of the individual agent.

4.2.11 Observations

During model execution, ChemSim tracks the current number of existing molecule agents, including the time of their creation and their eventual destruction upon reaction with a reactant. This data is then plotted using a time-series chart to visualize changes in the concentration profiles of target chemical species over time from the beginning to the end of every simulated experiment. The concentration profile values at the end of the simulation can be used to estimate or predict the final fate of the organic compounds in a given AOP treatment.

4.2.12 Model Simplifications

During model runs, pH, pressure, and temperature were assumed to be constant throughout the duration of the model and uniform within the reactor. Temperature was measured during the benchtop experiments and changed minimally, therefore supporting this assumption. The reactor was open to the atmosphere, so pressure was assumed to remain constant throughout the experiment/ model run. Another simplifying assumption was the consideration of only non-dissociated species. This was done in an effort to reduce computational complexity for the simplistic pathways used for early runs. However, the model can be altered to accept input pKa values of species and alter the ratios of non-dissociated and dissociated species after each time step, based on the pH of the reactor. This would also allow for the differentiation of reactions and the corresponding differences in reaction rate constants dependent on if species is dissociated.

4.2.13 Input Parameters

In order for the model to run, input parameters for the system of interest need to be included. During the creation process of ChemSim, care was taken to ensure its applicability in all AOP settings. Within the model, a maximum molecule count is set to prevent overloading the capacity of the computer being used; in our runs the starting molecule count was set to be one million. Within the code for the model, the user can

alter the time step for calculations and the initial pH, which are one second and 7 respectively for the model described here.

4.3 Experimental Materials and Methods

4.3.1 Reactor Setup

A benchtop photoreactor was used to obtain the experimental results. The photoreactor was composed of four reactor vessels each a Wheaton Roller Bottle with a volume of 1.8 L to allow for multiple experiments to be conducted at once. Reactor vessels were placed within the photo reactor such that they surrounded the low pressure UV lamp (Atlantic UV) with wavelength of 254 nm. UV intensity that the reactor was exposed to per wavelength was determined based on the spectral distribution provided for the lamp by Ace Glass Inc. To prevent overheating of the lamp, it was placed in a quartz immersion well (cooling jacket) to allow for water circulation around the lamp. Similarly, the reactor vessels were surrounded by water that continuously circulated in order to maintain a constant temperature. The photoreactor itself is contained within a glass box covered in aluminum foil in order to prevent the escape of UV light. Each reactor vessel was placed on a magnetic stir plate and a stir bar was used in order to maintain completely mixed conditions within each reactor. A dye study was conducted to verify completely mixed conditions within each reactor vessel. For the experimental runs, the desired organic compound and hydrogen peroxide were added to the reactor vessels and sampled as designated time steps. After removal from the photoreactor, samples were placed in amber vials and stored at a temperature of 4°C until they were ready to be analyzed. Byproduct analysis for a variety of compounds was conducted using gas chromatography, high performance liquid chromatography and ion chromatography with a detailed description of these methods included in the following section.

4.3.2 Chemical Description

All chemicals used in the experiments are of the highest grade. Acetone, hydrogen peroxide, oxalic acid, formic acid, acetic acid, glyoxylic acid, pyruvaldehyde (40% wt in soln) and pyruvic acid were obtained from sigma Aldrich of ACS grade. Formaldehyde was obtained from Fisher scientific. All experimental solutions were prepared using

MilliQ water (resistance > 18.2 MΩ.cm) obtained from a Millipore purification system. From these chemicals, stock solutions were made for the desired concentrations and then diluted to obtain standard solutions within the anticipated concentration range to be used for calibration curves. For the photochemical experiments, we added 10 mM hydrogen peroxide to 1mM of acetone prepared with DI water. Para-chloro benzoic acid (pCBA) solution, 0.25 μM, was also added as a probe compound for hydroxyl radicals.

4.3.3 Experimental Setup

UV photolysis experiment were conducted in the photoreactor described above with only one of the four reactor vessels in use. Using ferrioxalate actinometry, the light intensity in this reactor was obtained to be 5.16×10^{-7} Einstein/L-s. Temperature control measures within the photoreactor kept the temperature within 1°C of the initial temperature over the course of the experiment. Therefore the kinetics observed are that at room temperature.

Acetone, formaldehyde and pyruvic aldehyde were determined by derivatization with 2,4-dinitrophenyl hydrazine followed by analyses using a UHPLC 2000 series Dionex equipped with a reverse phase C-18 column (4.5 mm × 250 mm). The mobile phase used was acetonitrile and water in a gradient flow condition at 0.8 mL/min. Retention times for formaldehyde, acetone and pyruvate were 10.1 min, 21.1 min and 14 min, respectively using this method. Concentrations of pCBA were also determined using this system and reverse phase HPLC with a C-18 column. A different eluent with 45% of acetonitrile and 55% of 10 mM H₃PO₄ was used to find a retention time of 7.8 min at a 254 nm wavelength for pCBA. To determine the concentration of hydrogen peroxide, 2,9-dimethyl-1,10-phenanthroline (DMP) method was used for a diluted sample so concentrations were within the valid μM range for this test. Ion chromatography with Dionex ICS 2100 series equipped with an ion-exchange column was used to determine concentration of organic anions, acetate, formate, pyruvate and oxalate. The total organic carbon (TOC) was determined using a TOC analyzer, GE sievers.

4.4 Results

As a proof-of-concept demonstration of our ABM approach, we ran a series of computational experiments using ChemSim to simulate the UV/H₂O₂ process and then we compared our resulting simulated concentration profiles of a parent contaminant, acetone, hydrogen peroxide, and other byproducts to those that were experimentally measured using the experimental design conditions outlined in the previous section. Figure 4.4 shows the concentration profiles of the wide range of simulated byproducts, particularly radical species, that we were able to generate computationally in ChemSim as UV interacted with H₂O₂ in our model to produce hydroxyl radical byproducts that then reacted with acetone and catalyzed further byproduct chain reactions (Table 4.3) in our simulated reactor. This result shows how it is possible to visualize the fate of chemical species over time in a simulated AOP reactor to identify potential reaction dynamics that might be of interest to AOP designers, Figure 4.5. For example, certain intermediate species in our simulated experiment, such as acetyl peroxy radical ($\cdot\text{OOCH}_2\text{COCH}_3$), were found to have concentrations of zero throughout the entire simulation run, indicating that this species was either not being formed or was so highly reactive with other species that its reactions were essentially instantaneous with respect to the time-step increment used for the current simulation. Further analysis holding other produced compounds constant can help us to determine which of these situations is the case and, therefore, allow for a better understanding of the role that particular molecule plays in the advanced oxidation process.

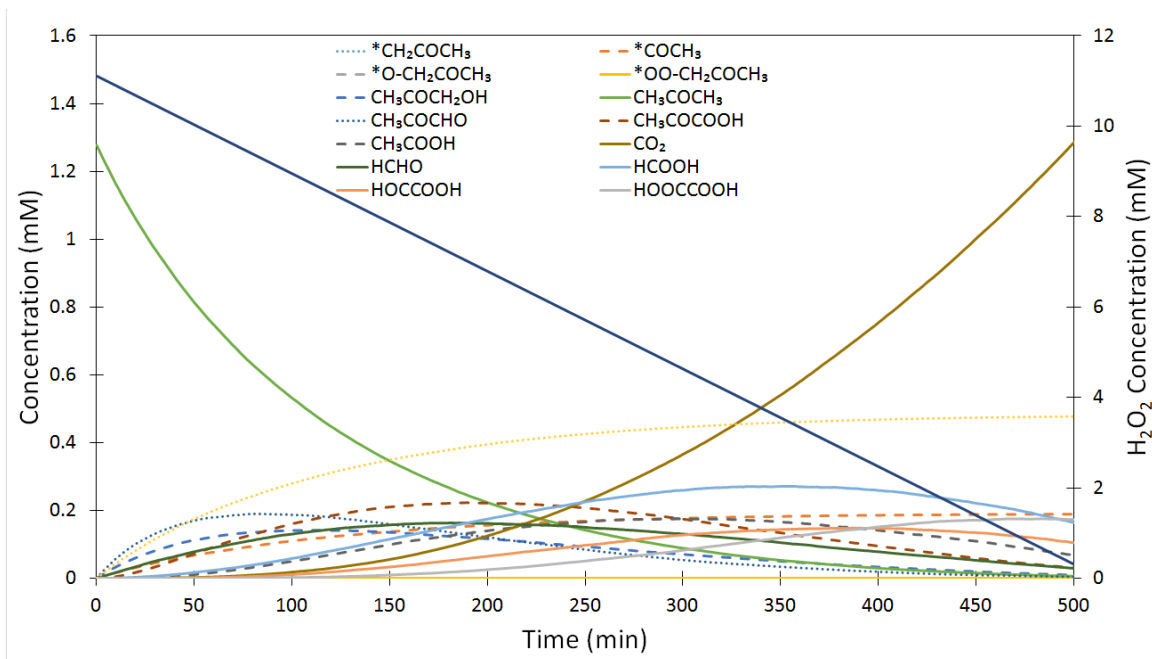


Figure 4.1 Time-dependent concentration profiles of acetone, hydrogen peroxide, and other byproducts formed in UV/H₂O₂ process

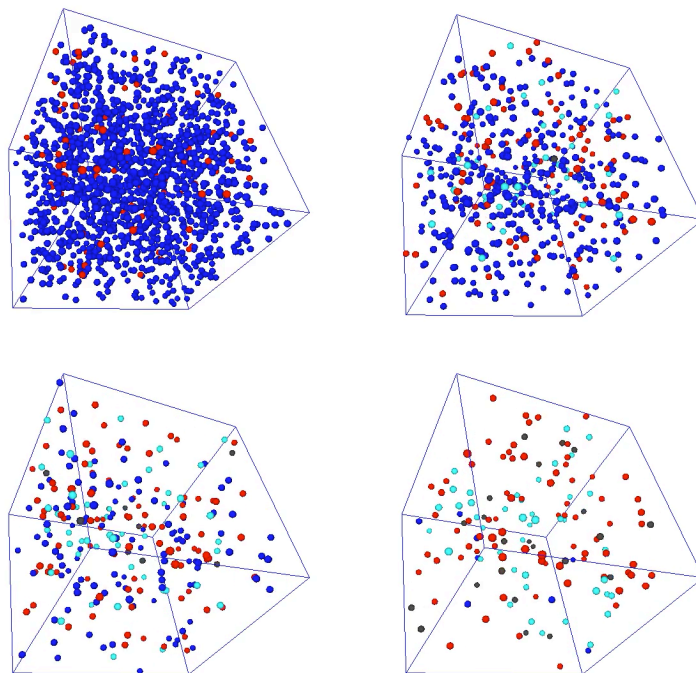


Figure 4.2 Snapshots of our agent based model that represent the agents of species at different time points. Blue represents hydrogen peroxide, teal represents acetone, red represents hydroxyl radicals, and dark gray represents byproducts

Table 4.1 Simplified reaction pathways and the reaction rate constants used in the test run

Reaction	Reaction Rate (Ratios)	Source
$\text{H}_2\text{O}_2 + h\nu \rightarrow \text{HO}^\bullet$	$2.1 \times 10^{-2} \text{ M s}$	[96]
$\text{CH}_3\text{COCH}_3 + \text{HO}^\bullet \rightarrow \cdot\text{CH}_2\text{COCH}_3$	$1.0 \times 10^8 \text{ M}^{-1}\text{s}^{-1}$	[69]
$\cdot\text{CH}_2\text{COCH}_3 + \text{O}_2 \rightarrow \cdot\text{OOCH}_2\text{COCH}_3$	$5.0 \times 10^9 \text{ M}^{-1}\text{s}^{-1}$	[79]
$\cdot\text{OOCH}_2\text{COCH}_3 + \cdot\text{OOCH}_2\text{COCH}_3 \rightarrow 2 \cdot\text{OCH}_3\text{COCH}_3 + \text{O}_2$	$1.0 \times 10^9 \text{ M}^{-1}\text{s}^{-1}$	(15%) [79]
$\cdot\text{OOCH}_2\text{COCH}_3 + \cdot\text{OOCH}_2\text{COCH}_3 \rightarrow \text{H}_2\text{O}_2 + 2 \text{CH}_3\text{COCHO}$		(25%) [79]
$\cdot\text{OOCH}_2\text{COCH}_3 + \cdot\text{OOCH}_2\text{COCH}_3 \rightarrow \text{CH}_3\text{COCHO} + \text{CH}_3\text{COCH}_2\text{OH} + \text{O}_2$		(60%) [79]
$\cdot\text{OCH}_2\text{COCH}_3 \rightarrow \cdot\text{COCH}_3 + \text{HCHO}$	$1.4 \times 10^6 \text{ s}^{-1}$	[79]
$\text{CH}_3\text{COCHO} + \text{HO}^\bullet \rightarrow \text{CH}_3\text{COCO}^\bullet\text{OH}$	$5.0 \times 10^8 \text{ M}^{-1}\text{s}^{-1}$	[110]
$\text{CH}_3\text{COCO}^\bullet\text{OH} + \text{HO}^\bullet \rightarrow \text{CH}_3\text{COOH}$	$1.0 \times 10^7 \text{ M}^{-1}\text{s}^{-1}$	[79]
$\text{CH}_3\text{COCH}_2\text{OH} + \text{HO}^\bullet \rightarrow \text{HCHO}$	$1.0 \times 10^8 \text{ M}^{-1}\text{s}^{-1}$	[79]
$\text{HCHO} + \text{HO}^\bullet \rightarrow \text{HCOOH}$	$1.0 \times 10^8 \text{ M}^{-1}\text{s}^{-1}$	[79]
$\text{CH}_3\text{COOH} + \text{HO}^\bullet \rightarrow \text{HOCCOO}^\bullet\text{H} + \text{HCOOH}$	$1.6 \times 10^7 \text{ M}^{-1}\text{s}^{-1}$	[111]
$\text{HOCCOO}^\bullet\text{H} + \text{HO}^\bullet \rightarrow \text{HOCCOOH}$	$1.9 \times 10^8 \text{ M}^{-1}\text{s}^{-1}$	[112]
$\text{HOCCOOH} + \text{HO}^\bullet \rightarrow \text{CO}_2$	$1.4 \times 10^6 \text{ M}^{-1}\text{s}^{-1}$	[113]
$\text{HCOOH} + \text{HO}^\bullet \rightarrow \text{CO}_2$	$4.5 \times 10^7 \text{ M}^{-1}\text{s}^{-1}$	[111]

Taking a closer look at the individual molecule concentration profiles produced in our simulated reactor, we can further see the value behind the ABM approach to modeling AOP treatment. We begin with an exposition of the underlying dynamics driving our simulated results to gain a better sense of how our reactions were catalyzed to generate our byproduct concentration profiles of interest. As in a real AOP reactor, the decay of our hydrogen peroxide agents is the driving force behind the reactions produced in our simulated reactor because it is this photolytic decay that leads to the formation of hydroxyl radical agents that then react with acetone agents to further catalyze the entire chain of byproduct agent reactions generated in each simulation run. As discussed above, we modelled photolysis using a linear decay rate fit to our experimental data to avoid the unnecessary complications of having to model the movement and reactions of individual photons. Therefore, we essentially fixed the rate of decay of our hydrogen

peroxide agents to ensure that a consistent proportion of such agents would be randomly selected for replacement with a hydroxyl radical agent as a way to replicate the photolysis process in each round of the simulation. Figure 4.6 shows the resulting linear decay of our hydrogen peroxide agents using this scheme to replicate photolysis reactions during the course of our experimental runs. Here we can see that hydrogen peroxide is behaving as expected to catalyze further byproduct reactions in our simulation in that the decay of hydrogen peroxide agents over time is both linear and is a reasonable fit to the experimental data. The one exception to note is that our simulated hydrogen peroxide is exhausted slightly earlier in our computational experiment as compared to our laboratory experiment but this is likely attributable to measurement error due to the sensitivity of sampling low concentration profile values toward the end of our laboratory experiment.

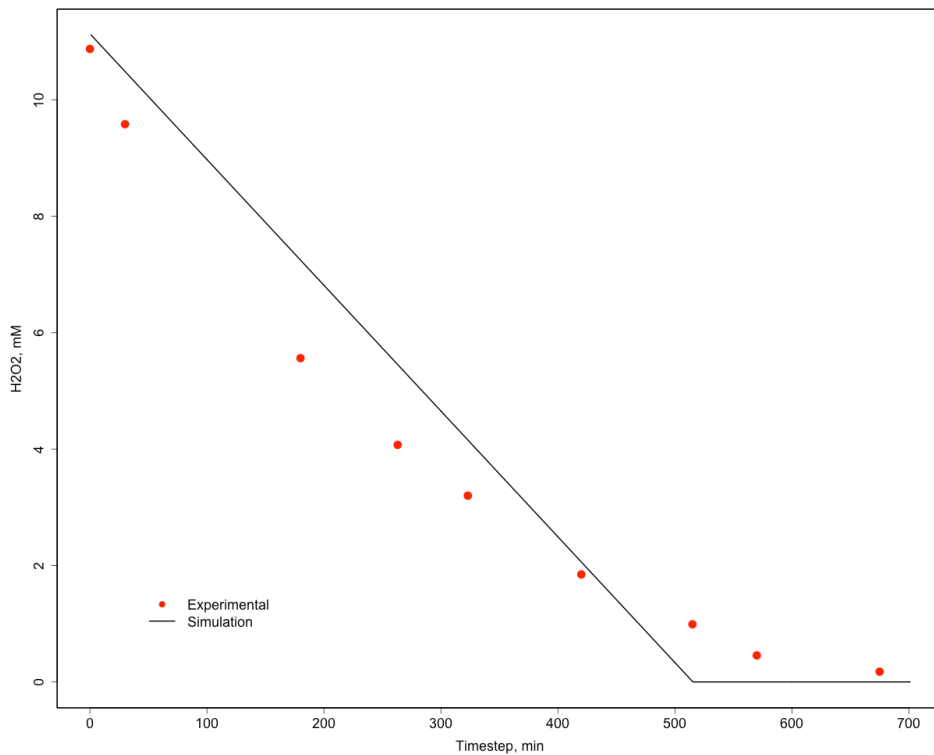


Figure 4.3 Time-dependent concentration profile of hydrogen peroxide

Having verified the expected linear decay of hydrogen peroxide agents in our simulated reactor experiments against our laboratory observations, we then moved on to explore the next reaction phase of our simulated AOP reactor. In this phase, our simulated

acetone agents are designed to react with any newly created hydroxyl radical agent that occupies the same reactor grid space either because it just emerged from our photolysis reactions occurring at random locations within the simulated reactor grid or because it came into contact with the acetone agent through the random-walk dispersion process driving all agent movement within our simulated reactor. Figure 4.7 shows that we were able to replicate the second-order acetone decay from our laboratory experiments in our simulated AOP reactor. We can see that the initial concentration of acetone agents matches the initial concentration of acetone in our laboratory experiments while decaying in an exponential manner to its final exhaustion point just slightly beyond the observed experimental findings. We should note that the simulated decay of acetone was also slightly more rapid than our experimental observations between time steps 100 and 300. This was likely due to some measurement error in our laboratory samples as well as the somewhat oversimplified modeling of hydroxyl radical elimination in our model. More specifically on the latter point, we did not include all possible elementary reaction pathways responsible for the production of byproducts that competitively react with hydroxyl radical agents and, therefore, our model overproduced hydroxyl radical agents over time that would have been eliminated in an actual AOP reactor through downstream reactions with further byproducts that were not modeled in our simplified simulated reactor.

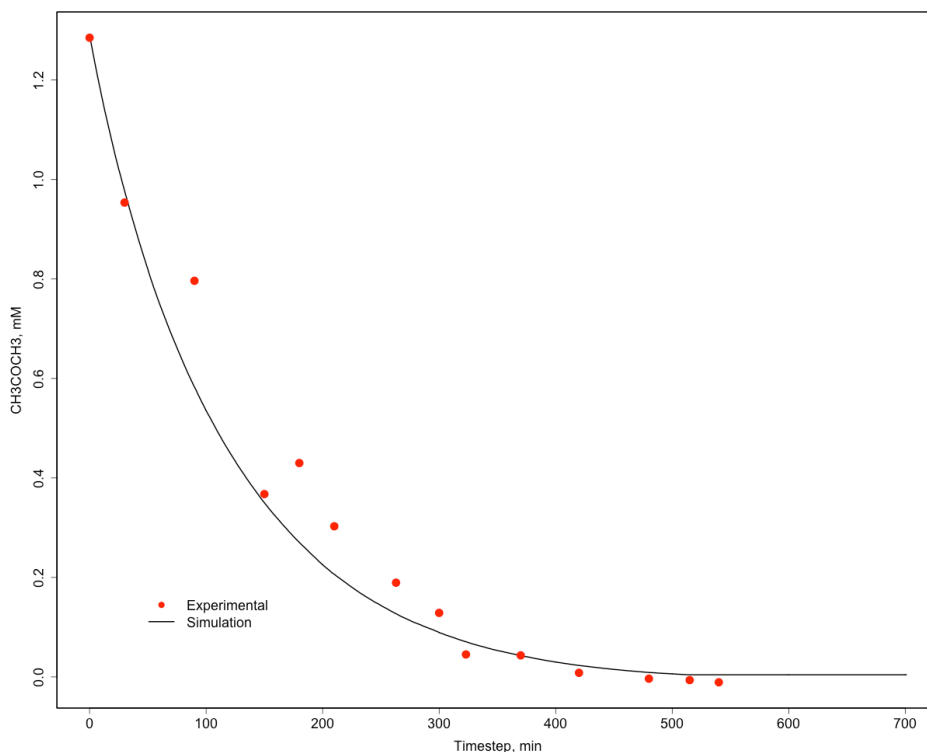


Figure 4.4 Time-dependent concentration profile of acetone

In addition to replicating the second-order decay of acetone in our simulated AOP reactor, we also generated and tracked the formation and concentration profile changes of three additional simulated byproducts over time: acetic acid, formic acid, and oxalic acid. Figures 4.8, 4.9, and 4.10 compare the simulated production of these three byproducts to their accompanying observed laboratory results to demonstrate how well our simulated concentration profile changes matched our observed laboratory results. Overall, these three figures show that we were able to successfully replicate the shape of our observed concentration profile changes over time for two of our simulated byproducts (acetic acid and oxalic acid) but were not necessarily able to match expected concentration levels for these byproducts at key time points of interest, such as the specific timing in which the byproduct reached its concentration peak before continuing its eventual decay over time.

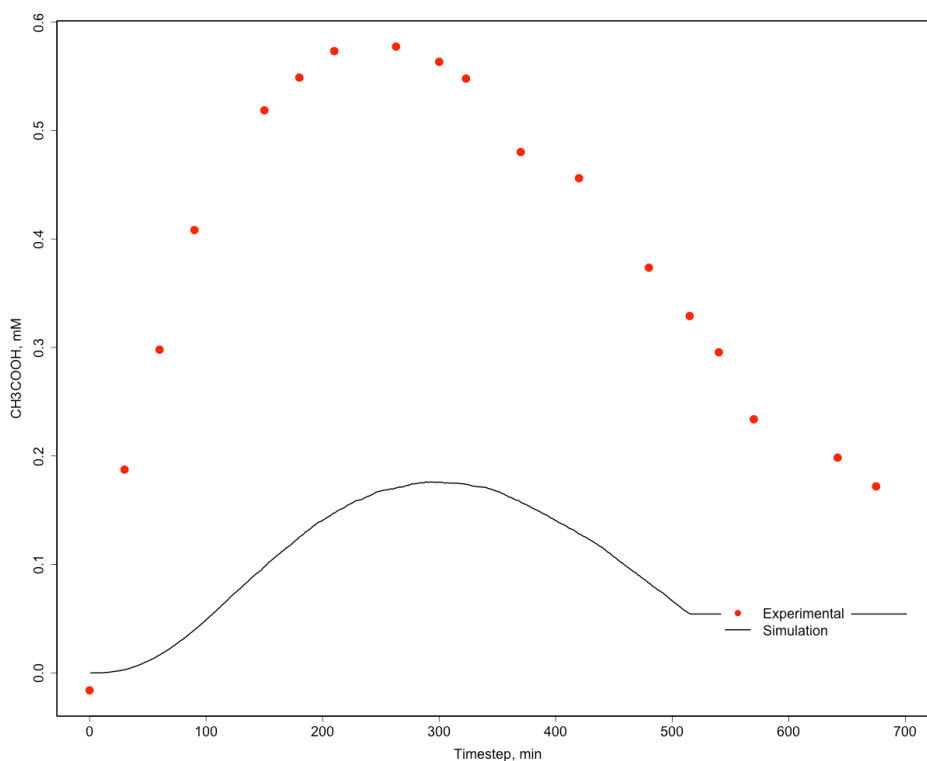


Figure 4.5 Time-dependent concentration profile of acetic acid

For example, we can see in Figure 4.8 that the shape of the simulated concentration profile for acetic acid follows the same somewhat Gaussian shape of our observed laboratory results for acetic acid but the peak concentration observed in the lab of nearly 0.6 mM at roughly 225 minutes was about 0.4 mM higher than the peak concentration achieved in our simulated reactor roughly 45 minutes later. In other words, the production of our simulated acetic acid was much less robust than the production of acetic acid in actual laboratory conditions, indicating that the elementary reaction pathways included in our proof-of-concept demonstration were possibly lacking critical downstream byproducts responsible for the production of acetic acid early in the AOP setting we attempted to simulate. Nevertheless, we were still able to reproduce the general trend of acetic acid concentration changes over time as observed in our laboratory experiments.

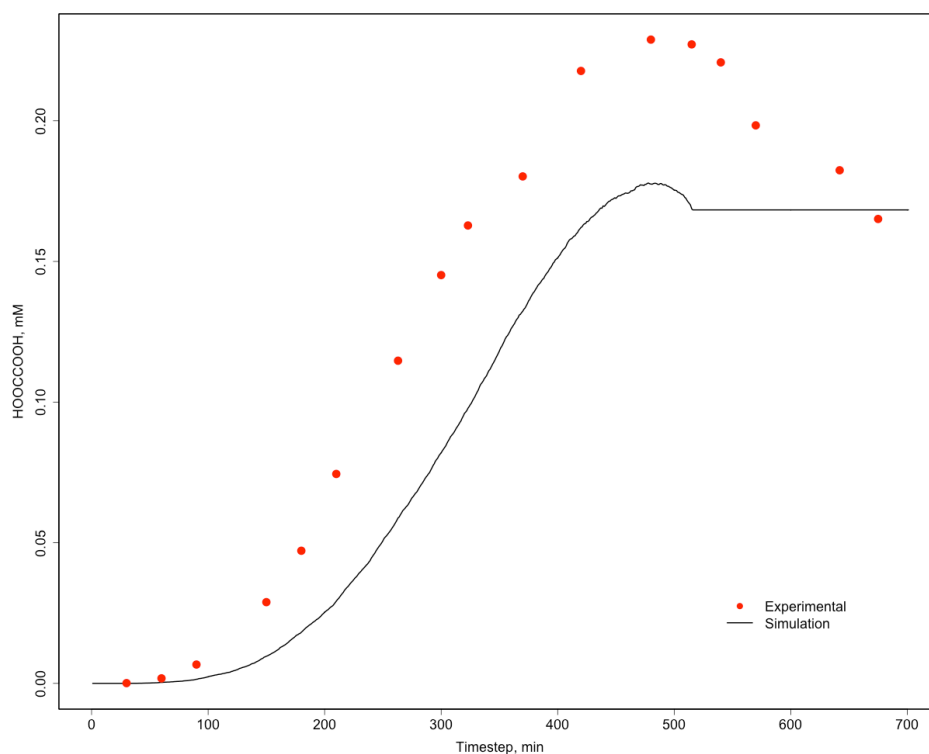


Figure 4.6 Time-dependent concentration profile of oxalic acid

A similar outcome to that of Figure 4.8 occurs in Figure 4.9 in which the simulated concentration profile of oxalic acid even more closely follows the trend in our observed laboratory results for oxalic acid, peaking at about 500 minutes for both results. However, the simulated concentration level of oxalic acid still fell about 0.1 mM short of the peak concentration level observed in the laboratory of roughly 0.25 mM at this same point in time. This tells us that the elementary reaction pathways used to generate this result were reasonably better at addressing all possible production sources for oxalic acid than was true for acetic acid, enabling our model to simulate the general trend in oxalic acid concentration profile changes over time relatively well.

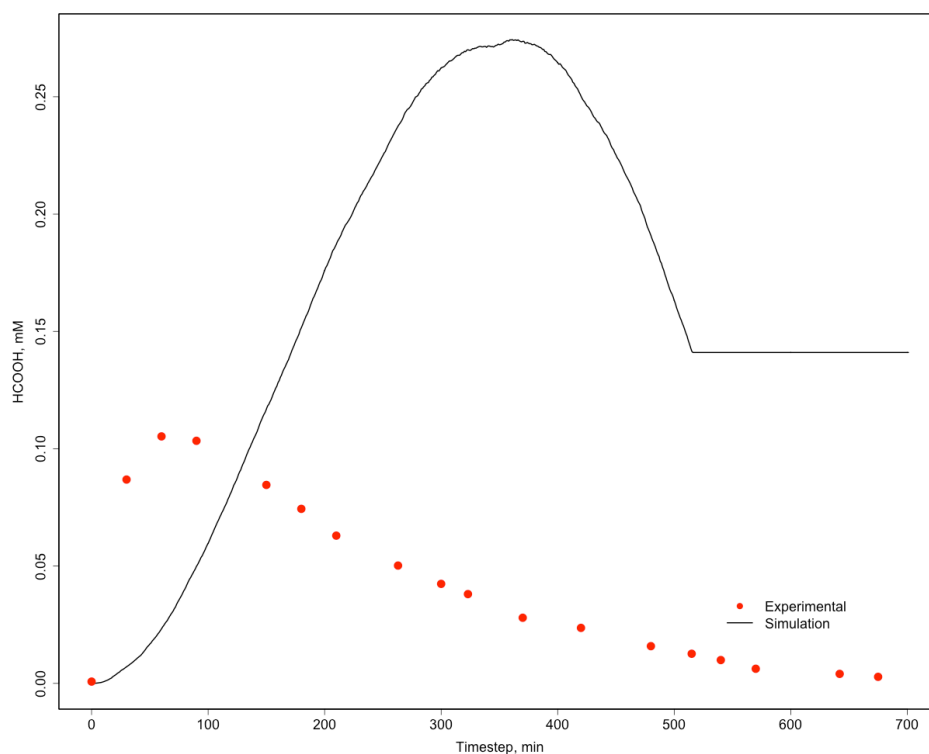


Figure 4.7 Time-dependent concentration profile of formic acid

Finally, we can see in Figure 4.10 that the simulated concentration profile for formic acid took a lot longer to reach the much higher concentration level peak of roughly 0.27 mM when compared to the concentration profile peak observed in our laboratory results of roughly 0.10 mM that occurred almost 300 minutes sooner in the laboratory. Here we can see that our model greatly overproduced formic acid which should have been eliminated much earlier due to the presence of other reactants that were not in our simplified elementary reaction pathways. This last result demonstrates most dramatically how sensitive our model results can be to the inclusion or exclusion of downstream reactants. In other words, given the bottom-up way in which ABMs generate their simulated system-level dynamics, it is critical that the model includes all possible reaction pathways responsible for the production of downstream reactants that can contribute to the production of simulated byproducts that fail to reach their observed concentration level peaks or for the production of competing reactions that can eliminate the overproduction of simulated byproducts beyond expected peak concentration levels observed in the laboratory. Nonetheless, our results show that it is possible to replicate

complex emergent trends in an ABM using a somewhat oversimplified reaction pathway that can always be refined to include further downstream reactant details.

4.5 Applicability and Future Work

Overall, these results show promise for developing a better understanding of the complex elementary reaction pathways and the fate of organic compounds. Now that ChemSim operational, and the program side of the project is complete, the next big step is to work on the chemistry side of the model and determine what reactions are missing and need to be included and if there are reactions that are negligible when looking at the full list. For instance, we know that hydroxyl radicals are not being removed from the system at the same rate in our trail runs as in real world reactors and know that addition of radical scavenging reactions for hydroxyl radicals need to be included. In the future, ideally ChemSim will be able to differentiate between dissociated and non-dissociated compounds and allow for consideration of pKa based off of system pH. Additionally, we would like to validate the model further by measuring byproduct concentrations of more species to see how well the model is able to predict those, since currently we are only have experimentally determined concentration profiles for five species.

5 Conclusions and Future Work

5.1 Chapter 2

- Use of QM calculations to determine elementary reactions from overall experimentally obtained reactions can be very beneficial, particularly when concentrations are below detection limits for nitrosamines.
- The resulting elementary reactions can be paired with reaction rate constants to predict time dependent concentration profiles of target compounds.

5.2 Chapter 3

- Elementary-reaction-based kinetic model can be used a way to screen for contaminants of concern and estimate the degradation byproducts of nitrosamines.
- Continued work is needed to improve model at pH 7 to ensure its applicability in other scenarios.

5.3 Chapter 4

- Agent-based modeling is a promising approach for determining concentration profiles in AOPs, particularly of compounds that are unable to be experimentally measured.
- Next steps are to run full reaction list and determine any missing elementary reactions along with improving the model to account for variation in pH.

6 Bibliography

- [1] D. W. Kolpin *et al.*, "Pharmaceuticals, hormones, and other organic wastewater contaminants in US streams, 1999-2000: A national reconnaissance," (in English), *Environmental Science & Technology*, vol. 36, no. 6, pp. 1202-1211, Mar 15 2002.
- [2] S. D. Richardson and S. Y. Kimura, "Water Analysis: Emerging Contaminants and Current Issues," (in English), *Analytical Chemistry*, vol. 88, no. 1, pp. 546-582, Jan 5 2016.
- [3] P. J. Phillips *et al.*, "Pharmaceutical Formulation Facilities as Sources of Opioids and Other Pharmaceuticals to Wastewater Treatment Plant Effluents," (in English), *Environmental Science & Technology*, vol. 44, no. 13, pp. 4910-4916, Jul 1 2010.
- [4] A. B. A. Boxall, C. J. Sinclair, K. Fenner, D. Kolpin, and S. J. Maud, "When synthetic chemicals degrade in the environment," (in English), *Environmental Science & Technology*, vol. 38, no. 19, pp. 368a-375a, Oct 1 2004.
- [5] J. Rice and P. Westerhoff, "Spatial and Temporal Variation in De Facto Wastewater Reuse in Drinking Water Systems across the U.S.A.," *Environmental Science & Technology*, vol. 49, no. 2, pp. 982-989, 2015/01/20 2015.
- [6] D. Minakata, K. Li, P. Westerhoff, and J. Crittenden, "Development of a Group Contribution Method To Predict Aqueous Phase Hydroxyl Radical (HO•) Reaction Rate Constants," *Environmental Science & Technology*, vol. 43, no. 16, pp. 6220-6227, 2009/08/15 2009.
- [7] G. V. Buxton, C. L. Greenstock, W. Phillips Helman, and A. B. Ross, *Critical Review of Rate Constants for Reactions of Hydrated Electrons, Hydrogen Atoms and Hydroxyl Radicals (•OH/•O-) in Aqueous Solution*. 1988.
- [8] D. Minakata and E. Coscarelli, "Mechanistic Insight into the Degradation of Nitrosamines via Aqueous-Phase UV Photolysis or a UV-Based Advanced Oxidation Process: Quantum Mechanical Calculations," *Molecules*, vol. 23, no. 3, p. 539, 2018.
- [9] (2017). *Technical Fact Sheet – N-Nitroso-dimethylamine (NDMA)*.
- [10] D. H. Fine *et al.*, "Determination of Dimethylnitrosamine in Air, Water, and Soil by Thermal-Energy Analysis - Measurements in Baltimore, Md.," (in English), *Environmental Science & Technology*, vol. 11, no. 6, pp. 581-584, 1977.
- [11] C. E. P. A. S. W. R. C. Board. (2018). *NDMA and Other Nitrosamines - Drinking Water Issues*. Available: https://www.waterboards.ca.gov/drinking_water/certlic/drinkingwater/NDMA.html

- [12] W. H. Glaze, J. W. Kang, and D. H. Chapin, "The Chemistry of Water-Treatment Processes Involving Ozone, Hydrogen-Peroxide and Ultraviolet-Radiation," (in English), *Ozone-Science & Engineering*, vol. 9, no. 4, pp. 335-352, 1987.
- [13] W. H. Glaze and J. W. Kang, "Advanced Oxidation Processes - Test of a Kinetic-Model for the Oxidation of Organic-Compounds with Ozone and Hydrogen-Peroxide in a Semibatch Reactor," (in English), *Industrial & Engineering Chemistry Research*, vol. 28, no. 11, pp. 1580-1587, Nov 1989.
- [14] G. Tchobanoglous, "Framework for Direct Potable Reuse," Alexandria, VA2015.
- [15] W. A. Mitch, J. O. Sharp, R. R. Trussell, R. L. Valentine, L. Alvarez-Cohen, and D. L. Sedlak, "N-nitrosodimethylamine (NDMA) as a drinking water contaminant: A review," (in English), *Environmental Engineering Science*, vol. 20, no. 5, pp. 389-404, Sep-Oct 2003.
- [16] N. A. Landsman, K. L. Swancutt, C. N. Bradford, C. R. Cox, J. J. Kiddle, and S. P. Mezyk, "Free radical chemistry of advanced oxidation process removal of nitrosamines in water," (in English), *Environmental Science & Technology*, vol. 41, no. 16, pp. 5818-5823, Aug 15 2007.
- [17] S. P. Mezyk, W. J. Cooper, K. P. Madden, and D. M. Bartels, "Free radical destruction of N-nitrosodimethylamine in water," (in English), *Environmental Science & Technology*, vol. 38, no. 11, pp. 3161-3167, Jun 1 2004.
- [18] Y. L. Chow, M. P. Lau, R. A. Perry, and J. N. S. Tam, "Photoreactions of Nitroso Compounds in Solution. XX. Photoreduction, Photoelimination, and Photoaddition of Nitrosamines," *Canadian Journal of Chemistry*, vol. 50, no. 7, pp. 1044-1050, 1972/04/01 1972.
- [19] Y. L. Chow, "Nitrosamine photochemistry. Reactions of aminium radicals," *Accounts of Chemical Research*, vol. 6, no. 10, pp. 354-360, 1973/10/01 1973.
- [20] D. Daiber and R. Preussmann, "Quantitative colorimetrische Bestimmung organischer N-Nitroso-Verbindungen durch photochemische Spaltung der Nitrosaminbindung," *Fresenius' Zeitschrift für analytische Chemie*, vol. 206, no. 5, pp. 344-352, 1964/09/01 1964.
- [21] S. Grilli, M. R. Tosi, and G. Prodi, "Degradation of dimethylnitrosoamine catalysed by physical and chemical agents," *Gan*, vol. 66, no. 5, pp. 481-8, Oct 1975.
- [22] M. I. Stefan and J. R. Bolton, "UV direct photolysis of N-nitrosodimethylamine (NDMA): Kinetic and product study," (in English), *Helvetica Chimica Acta*, vol. 85, no. 5, pp. 1416-1426, 2002.
- [23] C. Lee, W. Choi, and J. Yoon, "UV photolytic mechanism of N-nitrosodimethylamine in water: Roles of dissolved oxygen and solution pH," (in

- English), *Environmental Science & Technology*, vol. 39, no. 24, pp. 9702-9709, Dec 15 2005.
- [24] C. Lee, W. Choi, Y. G. Kim, and J. Yoon, "UV photolytic mechanism of N-nitrosodimethylamine in water: Dual pathways to methylamine versus dimethylamine," (in English), *Environmental Science & Technology*, vol. 39, no. 7, pp. 2101-2106, Apr 1 2005.
- [25] B. G. Kwon, J. O. Kim, and K. C. Namkung, "The formation of reactive species having hydroxyl radical-like reactivity from UV photolysis of N-nitrosodimethylamine (NDMA): Kinetics and mechanism," (in English), *Science of the Total Environment*, vol. 437, pp. 237-244, Oct 15 2012.
- [26] B. G. Kwon, J.-O. Kim, and J.-K. Kwon, "Formation of Reactive Species Enhanced by H₂O₂ Addition in the Photodecomposition of N-Nitrosodimethylamine (NDMA)," *Environmental Engineering Research*, vol. 18, no. 1, pp. 29-35, 3 2013.
- [27] C. Lee, J. Yoon, and U. Von Gunten, "Oxidative degradation of N-nitrosodimethylamine by conventional ozonation and the advanced oxidation process ozone/hydrogen peroxide," (in English), *Water Research*, vol. 41, no. 3, pp. 581-590, Feb 2007.
- [28] J. Lv, Y. M. Li, and Y. Song, "Reinvestigation on the ozonation of N-nitrosodimethylamine: Influencing factors and degradation mechanism," (in English), *Water Research*, vol. 47, no. 14, pp. 4993-5002, Sep 15 2013.
- [29] R. Y. Xiao, M. Noerpel, H. L. Luk, Z. S. Wei, and R. Spinney, "Thermodynamic and Kinetic Study of Ibuprofen with Hydroxyl Radical: A Density Functional Theory Approach," (in English), *International Journal of Quantum Chemistry*, vol. 114, no. 1, pp. 74-83, Jan 5 2014.
- [30] T. C. An, Y. P. Gao, G. Y. Li, P. V. Kamat, J. Peller, and M. V. Joyce, "Kinetics and Mechanism of (OH)-O-center dot Mediated Degradation of Dimethyl Phthalate in Aqueous Solution: Experimental and Theoretical Studies," (in English), *Environmental Science & Technology*, vol. 48, no. 1, pp. 641-648, Jan 7 2014.
- [31] S. Q. Liu *et al.*, "Theoretical and experimental insights into the center dot OH-mediated mineralization mechanism of flutriafol," (in English), *Electrochimica Acta*, vol. 235, pp. 223-232, May 1 2017.
- [32] D. Trogolo, B. K. Mishra, M. B. Heeb, U. von Gunten, and J. S. Arey, "Molecular Mechanism of NDMA Formation from N,N-Dimethylsulfamide During Ozonation: Quantum Chemical Insights into a Bromide-Catalyzed Pathway," (in English), *Environmental Science & Technology*, vol. 49, no. 7, pp. 4163-4175, Apr 7 2015.
- [33] D. Minakata, W. H. Song, S. P. Mezyk, and W. J. Cooper, "Experimental and theoretical studies on aqueous-phase reactivity of hydroxyl radicals with multiple

- carboxylated and hydroxylated benzene compounds," (in English), *Physical Chemistry Chemical Physics*, vol. 17, no. 17, pp. 11796-11812, 2015.
- [34] D. Minakata, W. H. Song, and J. Crittenden, "Reactivity of Aqueous Phase Hydroxyl Radical with Halogenated Carboxylate Anions: Experimental and Theoretical Studies," (in English), *Environmental Science & Technology*, vol. 45, no. 14, pp. 6057-6065, Jul 15 2011.
- [35] D. Minakata and J. Crittenden, "Linear Free Energy Relationships between Aqueous phase Hydroxyl Radical Reaction Rate Constants and Free Energy of Activation," (in English), *Environmental Science & Technology*, vol. 45, no. 8, pp. 3479-3486, Apr 15 2011.
- [36] M. J. T. Frisch, G.W.; Schlegel, H.B.; Scuseria, G.E.; Robb, M.A.; Cheeseman, J.R.; Scalmani, G.; Barone, V.; and B. P. Mennucci, G.A.; et al., "Gaussian 09, Revision D.02," ed. Wallingford, CT, USA: Gaussian Inc., 2009.
- [37] Y. Zhao and D. G. Truhlar, "The M06 suite of density functionals for main group thermochemistry, thermochemical kinetics, noncovalent interactions, excited states, and transition elements: two new functionals and systematic testing of four M06-class functionals and 12 other functionals," (in English), *Theoretical Chemistry Accounts*, vol. 120, no. 1-3, pp. 215-241, May 2008.
- [38] L. A. Curtiss, P. C. Redfern, and K. Raghavachari, "Gaussian-4 theory," (in English), *Journal of Chemical Physics*, vol. 126, no. 8, Feb 28 2007.
- [39] A. V. Marenich, C. J. Cramer, and D. G. Truhlar, "Universal Solvation Model Based on Solute Electron Density and on a Continuum Model of the Solvent Defined by the Bulk Dielectric Constant and Atomic Surface Tensions," (in English), *Journal of Physical Chemistry B*, vol. 113, no. 18, pp. 6378-6396, May 7 2009.
- [40] D. Minakata, S. P. Mezyk, J. W. Jones, B. R. Daws, and J. C. Crittenden, "Development of Linear Free Energy Relationships for Aqueous Phase Radical-Involved Chemical Reactions," (in English), *Environmental Science & Technology*, vol. 48, no. 23, pp. 13925-13932, Dec 2 2014.
- [41] C. Adamo and D. Jacquemin, "The calculations of excited-state properties with Time-Dependent Density Functional Theory," (in English), *Chemical Society Reviews*, vol. 42, no. 3, pp. 845-856, 2013.
- [42] A. D. Laurent, C. Adamo, and D. Jacquemin, "Dye chemistry with time-dependent density functional theory," (in English), *Physical Chemistry Chemical Physics*, vol. 16, no. 28, pp. 14334-14356, 2014.
- [43] G. V. Buxton and C. R. Stuart, "Radiation chemistry of aqueous solutions of hydrazine at elevated temperatures .2. Solutions containing oxygen," (in English), *Journal of the Chemical Society-Faraday Transactions*, vol. 93, no. 8, pp. 1535-1538, Apr 21 1997.

- [44] J. McMurry, "Nucleophilic addition of H₂O: Hydration," in *Organic Chemistry* Boston, MA: Cengage Learning, 2015.
- [45] E. Bothe and D. Schultefrohlinde, "Reaction of Dihydroxymethyl Radical with Molecular-Oxygen in Aqueous-Solution," (in English), *Zeitschrift Fur Naturforschung Section B-a Journal of Chemical Sciences*, vol. 35, no. 8, pp. 1035-1039, 1980.
- [46] C. Vonsonntag and H. P. Schuchmann, "The Elucidation of Peroxyl Radical Reactions in Aqueous-Solution with the Help of Radiation-Chemical Methods," (in English), *Angewandte Chemie-International Edition in English*, vol. 30, no. 10, pp. 1229-1253, Oct 1991.
- [47] S. Padmaja and R. E. Huie, "The Reaction of Nitric-Oxide with Organic Peroxyl Radicals," (in English), *Biochemical and Biophysical Research Communications*, vol. 195, no. 2, pp. 539-544, Sep 15 1993.
- [48] S. Goldstein and G. Czapski, "The Reaction of No-Center-Dot with O-2(Center-Dot-) and Ho2-Center-Dot - a Pulse-Radiolysis Study," (in English), *Free Radical Biology and Medicine*, vol. 19, no. 4, pp. 505-510, Oct 1995.
- [49] M. Anbar and H. Taube, "Interaction of Nitrous Acid with Hydrogen Peroxide and with Water," *Journal of the American Chemical Society*, vol. 76, no. 24, pp. 6243-6247, 1954/12/01 1954.
- [50] C. M. Sharpless and K. G. Linden, "Experimental and model comparisons of low- and medium-pressure Hg lamps for the direct and H₂O₂ assisted UV photodegradation of N-nitrosodimethylamine in simulated drinking water," (in English), *Environmental Science & Technology*, vol. 37, no. 9, pp. 1933-1940, May 1 2003.
- [51] Y.-L. Chow, "Photolysis of N-nitrosoamines," *Tetrahedron Letters*, vol. 5, no. 34, pp. 2333-2338, 1964/01/01/ 1964.
- [52] E. M. Burgess and J. M. Lavanish, "Photochemical decomposition of N-nitrosamines," *Tetrahedron Letters*, vol. 5, no. 20, pp. 1221-1226, 1964/01/01/ 1964.
- [53] T. A. Grover, J. A. Ramseyer, and L. H. Piette, "Photolysis of Nitrosamines and Nitrosamides at Neutral Ph - a Spin-Trap Study," (in English), *Free Radical Biology and Medicine*, vol. 3, no. 1, pp. 27-32, 1987.
- [54] I. Wagner, H. Strehlow, and G. Busse, "Flash-Photolysis of Nitrate Ions in Aqueous-Solution," (in English), *Zeitschrift Fur Physikalische Chemie-Wiesbaden*, vol. 123, no. 1, pp. 1-33, 1980.
- [55] M. C. Gonzalez, A. M. Braun, A. B. Prevot, and E. Pelizzetti, "Vacuum-Ultraviolet (Vuv) Photolysis of Water - Mineralization of Atrazine," (in English), *Chemosphere*, vol. 28, no. 12, pp. 2121-2127, Jun 1994.

- [56] J. Mack and J. R. Bolton, "Photochemistry of nitrite and nitrate in aqueous solution: a review," (in English), *Journal of Photochemistry and Photobiology a-Chemistry*, vol. 128, no. 1-3, pp. 1-13, Nov 1999.
- [57] H. O. Tugaoen, S. Garcia-Segura, K. Hristovski, and P. Westerhoff, "Challenges in photocatalytic reduction of nitrate as a water treatment technology," (in English), *Science of the Total Environment*, vol. 599, pp. 1524-1551, Dec 1 2017.
- [58] A. C. Hindmarsh, *GEAR: Ordinary Differential Equation System Solver*. Lawrence Livermore Laboratory, 1974.
- [59] A. Hindmarsh, "Large ordinary differential equation systems and software," *IEEE Control Systems Magazine*, vol. 2, no. 4, pp. 24-30, 1982.
- [60] K. Li, D. R. Hokanson, J. C. Crittenden, R. R. Trussell, and D. Minakata, "Evaluating UV/H₂O₂ processes for methyl tert-butyl ether and tertiary butyl alcohol removal: Effect of pretreatment options and light sources," (in English), *Water Research*, vol. 42, no. 20, pp. 5045-5053, Dec 2008.
- [61] X. Guo, D. Minakata, J. F. Niu, and J. Crittenden, "Computer-Based First-Principles Kinetic Modeling of Degradation Pathways and Byproduct Fates in Aqueous-Phase Advanced Oxidation Processes," (in English), *Environmental Science & Technology*, vol. 48, no. 10, pp. 5718-5725, May 20 2014.
- [62] J. C. Crittenden, S. M. Hu, D. W. Hand, and S. A. Green, "A kinetic model for H₂O₂/UV process in a completely mixed batch reactor," (in English), *Water Research*, vol. 33, no. 10, pp. 2315-2328, Jul 1999.
- [63] O. Svoboda and P. Slaviček, "Is Nitrate Anion Photodissociation Mediated by Singlet-Triplet Absorption?," *The Journal of Physical Chemistry Letters*, vol. 5, no. 11, pp. 1958-1962, 2014/06/05 2014.
- [64] O. Svoboda, L. Kubelová, and P. Slaviček, "Enabling Forbidden Processes: Quantum and Solvation Enhancement of Nitrate Anion UV Absorption," *The Journal of Physical Chemistry A*, vol. 117, no. 48, pp. 12868-12877, 2013/12/05 2013.
- [65] M. Fischer and P. Warneck, "Photodecomposition of Nitrite and Undissociated Nitrous Acid in Aqueous Solution," *The Journal of Physical Chemistry*, vol. 100, no. 48, pp. 18749-18756, 1996/01/01 1996.
- [66] L. Chu and C. Anastasio, "Quantum Yields of Hydroxyl Radical and Nitrogen Dioxide from the Photolysis of Nitrate on Ice," *The Journal of Physical Chemistry A*, vol. 107, no. 45, pp. 9594-9602, 2003/11/01 2003.
- [67] J. Thogersen *et al.*, "Primary photochemistry of peroxyxynitrite in aqueous solution," (in English), *Chemical Physics Letters*, vol. 641, pp. 187-192, Nov 16 2015.

- [68] K. Li, M. I. Stefan, and J. C. Crittenden, "UV photolysis of trichloroethylene: Product study and kinetic modeling," (in English), *Environmental Science & Technology*, vol. 38, no. 24, pp. 6685-6693, Dec 15 2004.
- [69] G. V. Buxton, C. L. Greenstock, W. P. Helman, and A. B. Ross, "Critical-Review of Rate Constants for Reactions of Hydrated Electrons, Hydrogen-Atoms and Hydroxyl Radicals (.Oh/.O-) in Aqueous-Solution," (in English), *Journal of Physical and Chemical Reference Data*, vol. 17, no. 2, pp. 513-886, 1988.
- [70] H. Christensen, K. Sehested, and H. Corfitzen, "Reactions of hydroxyl radicals with hydrogen peroxide at ambient and elevated temperatures," *The Journal of Physical Chemistry*, vol. 86, no. 9, pp. 1588-1590, 1982/04/01 1982.
- [71] A. Farhataziz and A. B. Ross, "Selected Specific Rates of Reactions of Transients from Water in Aqueous Solution," U. N. B. o. Standards, Ed., ed, 1977.
- [72] B. H. J. Bielski, D. E. Cabelli, R. L. Arudi, and A. B. Ross, "Reactivity of HO₂/O₂- Radicals in Aqueous Solution," *Journal of Physical and Chemical Reference Data*, vol. 14, no. 4, pp. 1041-1100, 1985/10/01 1985.
- [73] P. Neta, R. E. Huie, and A. B. Ross, "Rate Constants for Reactions of Inorganic Radicals in Aqueous Solution," *Journal of Physical and Chemical Reference Data*, vol. 17, no. 3, pp. 1027-1284, 1988/07/01 1988.
- [74] M. Nakashima and E. Hayon, "Rates of reaction of inorganic phosphate radicals in solution," *The Journal of Physical Chemistry*, vol. 74, no. 17, pp. 3290-3291, 1970/08/01 1970.
- [75] J. Weinstein and B. H. J. Bielski, *Kinetics of the Interaction of HO₂ and O₂- Radicals with Hydrogen Peroxide, The Haber-Weiss Reaction*. 1979, pp. 58-62.
- [76] S.-n. Chen and M. Z. Hoffman, "Rate Constants for the Reaction of the Carbonate Radical with Compounds of Biochemical Interest in Neutral Aqueous Solution," *Radiation Research*, vol. 56, no. 1, pp. 40-47, 1973.
- [77] T. E. Eriksen, J. Lind, and G. Merényi, "On the acid-base equilibrium of the carbonate radical," *Radiation Physics and Chemistry (1977)*, vol. 26, no. 2, pp. 197-199, 1985/01/01/ 1985.
- [78] S. Goldstein and J. Rabani, "Mechanism of nitrite formation by nitrate photolysis in aqueous solutions: The role of peroxyxynitrite, nitrogen dioxide, and hydroxyl radical," (in English), *Journal of the American Chemical Society*, vol. 129, no. 34, pp. 10597-10601, Aug 29 2007.
- [79] D. Kamath, S. P. Mezyk, and D. Minakata, "Elucidating the Elementary Reaction Pathways and Kinetics of Hydroxyl Radical-Induced Acetone Degradation in Aqueous Phase Advanced Oxidation Processes," (in English), *Environmental Science & Technology*, vol. 52, no. 14, pp. 7763-7774, Jul 17 2018.

- [80] M. C. Gonzalez and A. M. Braun, "VUV photolysis of aqueous solutions of nitrate and nitrite," *Research on Chemical Intermediates*, journal article vol. 21, no. 8, pp. 837-859, August 01 1995.
- [81] M. N. Hughes, "Relationships between nitric oxide, nitroxyl ion, nitrosonium cation and peroxyxynitrite," (in English), *Biochimica Et Biophysica Acta-Bioenergetics*, vol. 1411, no. 2-3, pp. 263-272, May 5 1999.
- [82] T. Logager and K. Sehested, "Formation and Decay of Peroxynitrous Acid - a Pulse-Radiolysis Study," (in English), *Journal of Physical Chemistry*, vol. 97, no. 25, pp. 6664-6669, Jun 24 1993.
- [83] E. De Laurentiis, M. Minella, S. Berto, V. Maurino, C. Minero, and D. Vione, "The fate of nitrogen upon nitrite irradiation: Formation of dissolved vs. gas-phase species," *Journal of Photochemistry and Photobiology A: Chemistry*, vol. 307-308, pp. 30-34, 2015/07/01/ 2015.
- [84] F. T. Bonner and N. Y. Wang, "Reduction of Nitric-Oxide by Hydroxylamine .1. Kinetics and Mechanism," (in English), *Inorganic Chemistry*, vol. 25, no. 11, pp. 1858-1862, May 21 1986.
- [85] A. R. Cook, N. Dimitrijevic, B. W. Dreyfus, D. Meisel, L. A. Curtiss, and D. M. Camaioni, "Reducing Radicals in Nitrate Solutions. The NO₃²⁻ System Revisited," *The Journal of Physical Chemistry A*, vol. 105, no. 14, pp. 3658-3666, 2001/04/01 2001.
- [86] P. Westerhoff, Y. Yoon, S. Snyder, and E. Wert, "Fate of endocrine-disruptor, pharmaceutical, and personal care product chemicals during simulated drinking water treatment processes," (in English), *Environmental Science & Technology*, vol. 39, no. 17, pp. 6649-6663, Sep 1 2005.
- [87] S. A. Snyder, E. C. Wert, L. Hongxia, P. Westerhoff, and Y. Yoon, "Removal of EDCs and Pharmaceuticals in Drinking and Reuse Treatment Processes," in "AWWARF Project," 2007.
- [88] W. H. Glaze, Y. Lay, and J. W. Kang, "Advanced Oxidation Processes - a Kinetic-Model for the Oxidation of 1,2-Dibromo-3-Chloropropane in Water by the Combination of Hydrogen-Peroxide and Uv-Radiation," (in English), *Industrial & Engineering Chemistry Research*, vol. 34, no. 7, pp. 2314-2323, Jul 1995.
- [89] B. A. Wols and C. H. M. Hofman-Caris, "Review of photochemical reaction constants of organic micropollutants required for UV advanced oxidation processes in water," (in English), *Water Research*, vol. 46, no. 9, pp. 2815-2827, Jun 1 2012.
- [90] H. S. Fogler, *Elements of chemical reaction engineering*, 3 ed. Upper Saddle River, New Jersey: Prentice-Hall, 1999.

- [91] G. R. Peyton, "Guidelines for the selection of a chemical model for advanced oxidation processes," in *Symposium on Advanced Oxidation Processes for the Treatment of Contaminated Water and Air*, Wastewater Technology Centre of Environment Canada, 1990.
- [92] W. Braun, J. T. Herron, and D. K. Kahaner, "AcuChem - a Computer-Program for Modeling Complex Chemical-Reaction Systems," (in English), *International Journal of Chemical Kinetics*, vol. 20, no. 1, pp. 51-62, Jan 1988.
- [93] Y. C. D., H. W. R., and M. T., "Kinetic features of advanced oxidation processes for treating aqueous chemical mixtures," in *Chemical Oxidation, Technologies for the Nineties*, Nashville, Tennessee, USA, 1992.
- [94] C. W. Gear, "The automatic integration of ordinary differential equations," *Commun. ACM*, vol. 14, no. 3, pp. 176-179, 1971.
- [95] L. Y. S., "Oxidation of 1,2-Dibromo-3-Chloropropane in Ground Water using Advanced Oxidation Processes," PhD, University of California at Los Angeles, California, USA, 1989.
- [96] *Manual Advanced Oxidation Process Simulation Software (AdOxTM) version 1.0*, 1998.
- [97] J. C. Crittenden and MWH, *MWH's water treatment : principles and design*. Hoboken, N.J: Wiley, 2012.
- [98] B. A. Wols, D. J. H. Harmsen, J. Wanders-Dijk, E. F. Beerendonk, and C. H. M. Hofman-Caris, "Degradation of pharmaceuticals in UV (LP)/H₂O₂ reactors simulated by means of kinetic modeling and computational fluid dynamics (CFD)," (in English), *Water Research*, vol. 75, pp. 11-24, May 15 2015.
- [99] B. A. Wols, D. J. H. Harmsen, E. F. Beerendonk, and C. H. M. Hofman-Caris, "Predicting pharmaceutical degradation by UV (LP)/H₂O₂ processes: A kinetic model," (in English), *Chemical Engineering Journal*, vol. 255, pp. 334-343, Nov 1 2014.
- [100] H. V. Parunak, R. Savit, and R. L. Riolo, "Agent-based modeling vs. equation-based modeling: A case study and users ' guide," (in English), *Multi-Agent Systems and Agent-Based Simulation*, vol. 1534, pp. 10-25, 1998.
- [101] S. F. Railsback and V. Grimm, *Agent-Based and Individual-Based Modeling: A Practical Introduction*. Princeton, New Jersey: Princeton University Press, 2012.
- [102] M. M. Waldrop, "FREE AGENTS Monumentally complex models are gaming out disaster scenarios with millions of simulated people," (in English), *Science*, vol. 360, no. 6385, pp. 144-147, Apr 13 2018.
- [103] M. T. Klann, A. Lapin, and M. Reuss, "Agent-based simulation of reactions in the crowded and structured intracellular environment: Influence of mobility and

- location of the reactants," (in English), *Bmc Systems Biology*, vol. 5, May 14 2011.
- [104] J. A. Bachman and P. Sorger, "New approaches to modeling complex biochemistry," (in English), *Nature Methods*, vol. 8, no. 2, pp. 130-131, Feb 2011.
- [105] M. Pogson, R. Smallwood, E. Qwarnstrom, and M. Holcombe, "Formal agent-based modelling of intracellular chemical interactions," (in English), *Biosystems*, vol. 85, no. 1, pp. 37-45, Jul 2006.
- [106] S. Luke, C. Cioffi, L. Panait, K. Sullivan, and G. Balan, *MASON: A Multiagent Simulation Environment*. 2005, pp. 517-527.
- [107] V. Grimm, U. Berger, D. L. DeAngelis, J. G. Polhill, J. Giske, and S. F. Railsback, "The ODD protocol A review and first update," (in English), *Ecological Modelling*, vol. 221, no. 23, pp. 2760-2768, Nov 24 2010.
- [108] V. Grimm *et al.*, *A Standard Protocol for Describing Individual-Based and Agent Based Models*. 2006, pp. 115-126.
- [109] M. Teschner, B. Heidelberger, M. Müller, D. Pomeranets, and M. Gross, *Optimized Spatial Hashing for Collision Detection of Deformable Objects*. 2003.
- [110] A. Monod, L. Poulain, S. Grubert, D. Voisin, and H. Wortham, *Kinetics of OH-initiated oxidation of oxygenated organic compounds in the aqueous phase: New rate constants, structure-activity relationships and atmospheric implications*. 2005, pp. 7667-7688.
- [111] M. Chin and P. H. Wine, "A Temperature-Dependent Competitive Kinetics Study of the Aqueous-Phase Reactions of OH Radicals with Formate, Formic Acid, Acetate, Acetic Acid, and Hydrated Formaldehyde," in *Aquatic and Surface Photochemistry* Boca Raton: CRC Press, 1994.
- [112] B. Ervens, S. Gligorovski, and H. Herrmann, "Temperature-dependent rate constants for hydroxyl radical reactions with organic compounds in aqueous solutions," *Physical Chemistry Chemical Physics*, 10.1039/B300072A vol. 5, no. 9, pp. 1811-1824, 2003.
- [113] K. Sehested, N. Getoff, F. Schwoerer, V. M. Markovic, and S. O. Nielsen, "Pulse radiolysis of oxalic acid and oxalates," *The Journal of Physical Chemistry*, vol. 75, no. 6, pp. 749-755, 1971/03/01 1971.

A Supporting Information for Chapter 4

A.1 Hydrogen Peroxide Decay Slope Calculations

Table A.6.1 Experimentally obtained concentrations of hydrogen peroxide over time in benchtop photolysis experiment

Time (min)	H ₂ O ₂ Conc. (mM)
0	10.87
30	9.58
180	5.56
263	4.07
323	3.20
420	1.85
515	0.99
570	0.46
675	0.18

Table A.6.2 Slope and y intercept for linear fit of hydrogen peroxide decay based on variation in included experimental points

Range	Slope	y - intercept
0 - 323 min	-2.38×10^{-2}	10.44
0 - 420 min	-2.16×10^{-2}	10.23
0 - 570 min	-1.79×10^{-2}	9.73
0 - 675 min	-1.59×10^{-2}	9.36

A.2 Console Output

ChemSim, version 0.5.181

WARNING: Molecule count limited by configuration

Max Memory: 4294967296b

Molecule Size: 384b

Staring Molecule Limit: 1E6 (384000000b)

Time Step (sec): 1.0

Hydroxyl Retention: 0.25

Reactor Dimensions (nm): 4208, 4208, 4208

Reactions: experiment/pathway5.csv [2018-08-04 - 00:54:25]

H2O2 + UV -> HO• + HO•, r = 0 (photolysis)

CH3COCH3 + HO• -> •CH2COCH3, r = 339 (bimolecular)

•CH2COCH3 + O2 -> •OO-CH2COCH3, r = 1108 (bimolecular)

$\bullet\text{OO-CH}_2\text{COCH}_3 + \bullet\text{OO-CH}_2\text{COCH}_3 \rightarrow \bullet\text{O-CH}_2\text{COCH}_3 + \bullet\text{O-CH}_2\text{COCH}_3 + \text{O}_2$, r = 713
 (bimolecular, 0.15)
 $\bullet\text{OO-CH}_2\text{COCH}_3 + \bullet\text{OO-CH}_2\text{COCH}_3 \rightarrow \text{H}_2\text{O}_2 + \text{CH}_3\text{COCHO} + \text{CH}_3\text{COCHO}$, r = 713
 (bimolecular, 0.25)
 $\bullet\text{OO-CH}_2\text{COCH}_3 + \bullet\text{OO-CH}_2\text{COCH}_3 \rightarrow \text{CH}_3\text{COCHO} + \text{CH}_3\text{COCH}_2\text{OH} + \text{O}_2$, r = 713
 (bimolecular, 0.6)
 $\bullet\text{O-CH}_2\text{COCH}_3 \rightarrow \bullet\text{COCH}_3 + \text{HCHO}$, r = 82 (unimolecular)
 $\text{CH}_3\text{COCHO} + \text{HO}\bullet \rightarrow \text{CH}_3\text{COCO}\bullet\text{OH}$, r = 574 (bimolecular)
 $\text{CH}_3\text{COCO}\bullet\text{OH} + \text{HO}\bullet \rightarrow \text{CH}_3\text{COOH}$, r = 158 (bimolecular)
 $\text{CH}_3\text{COCH}_2\text{OH} + \text{HO}\bullet \rightarrow \text{HCHO}$, r = 339 (bimolecular)
 $\text{HCHO} + \text{HO}\bullet \rightarrow \text{HCOOH}$, r = 339 (bimolecular)
 $\text{CH}_3\text{COOH} + \text{HO}\bullet \rightarrow \text{HOCCOOH} + \text{HCOOH}$, r = 185 (bimolecular)
 $\text{HOCCOOH} + \text{HO}\bullet \rightarrow \text{HOCCOO}\bullet\text{H}$, r = 419 (bimolecular)
 $\text{HOCCOO}\bullet\text{H} + \text{HO}\bullet \rightarrow \text{CO}_2$, r = 82 (bimolecular)
 $\text{HCOOH} + \text{HO}\bullet \rightarrow \text{CO}_2$, r = 260 (bimolecular)
 $\text{HO}\bullet \rightarrow \text{H}\bullet$, r = 0 (unimolecular, 0.0)

Molecule to mol scalar: 4.48E7

Generating 896000 molecules of H2O2
 Generating 103040 molecules of CH3COCH3
 Adding molecules to the schedule...
 H2O2 photolysis decay rate: -31.99 molecules/timestep
 Estimated running time of 38401 time steps, padded to 42001

2018-08-04T00:54:52.957: Starting simulation...
 2018-08-04T00:54:52.957: 0 of 42001
 2018-08-04T00:55:18.765: 60 of 42001
 2018-08-04T00:55:48.621: 120 of 42001
 2018-08-04T00:56:15.114: 180 of 42001
 2018-08-04T00:56:42.905: 240 of 42001
 2018-08-04T00:57:08.207: 300 of 42001
 2018-08-04T00:57:33.849: 360 of 42001
 2018-08-04T00:58:00.734: 420 of 42001
 2018-08-04T00:58:24.769: 480 of 42001
 2018-08-04T00:58:48.059: 540 of 42001
 2018-08-04T00:59:11.341: 600 of 42001
 ...
 ...
 ...
 2018-08-04T02:38:46.061: 41760 of 42001
 2018-08-04T02:38:46.966: 41820 of 42001
 2018-08-04T02:38:47.866: 41880 of 42001
 2018-08-04T02:38:48.758: 41940 of 42001
 2018-08-04T02:38:49.657: 42000 of 42001

Molecule counts written to: data/results-1.csv
 Molar counts written to: data/molar-1.csv

2018-08-04T02:38:49.722

B Copyright documentation

For all images in Chapter 2, Mechanistic Insight into the Degradation of Nitrosamines via Aqueous-Phase UV Photolysis or a UV-Based Advanced Oxidation Process: Quantum Mechanical Calculations, published in *Molecules*, the copyright is retained by the authors Dr. Daisuke Minakata and Erica Coscarelli.

Here is the reference link, <https://www.mdpi.com/authors/rights>, with the relevant section copied below.

Copyright and Licensing

For all articles published in MDPI journals, copyright is retained by the authors. Articles are licensed under an open access Creative Commons CC BY 4.0 license, meaning that anyone may download and read the paper for free. In addition, the article may be reused and quoted provided that the original published version is cited. These conditions allow for maximum use and exposure of the work, while ensuring that the authors receive proper credit.

All images other images in the document were created by the author(s).